Towards Practical Hybrid Laminar Flow Control

Boundary Layer Stability with Suction and Scalability of Pressure Losses across Perforated Sheets

J.P.P. Hemmen

Technische Universiteit Delft

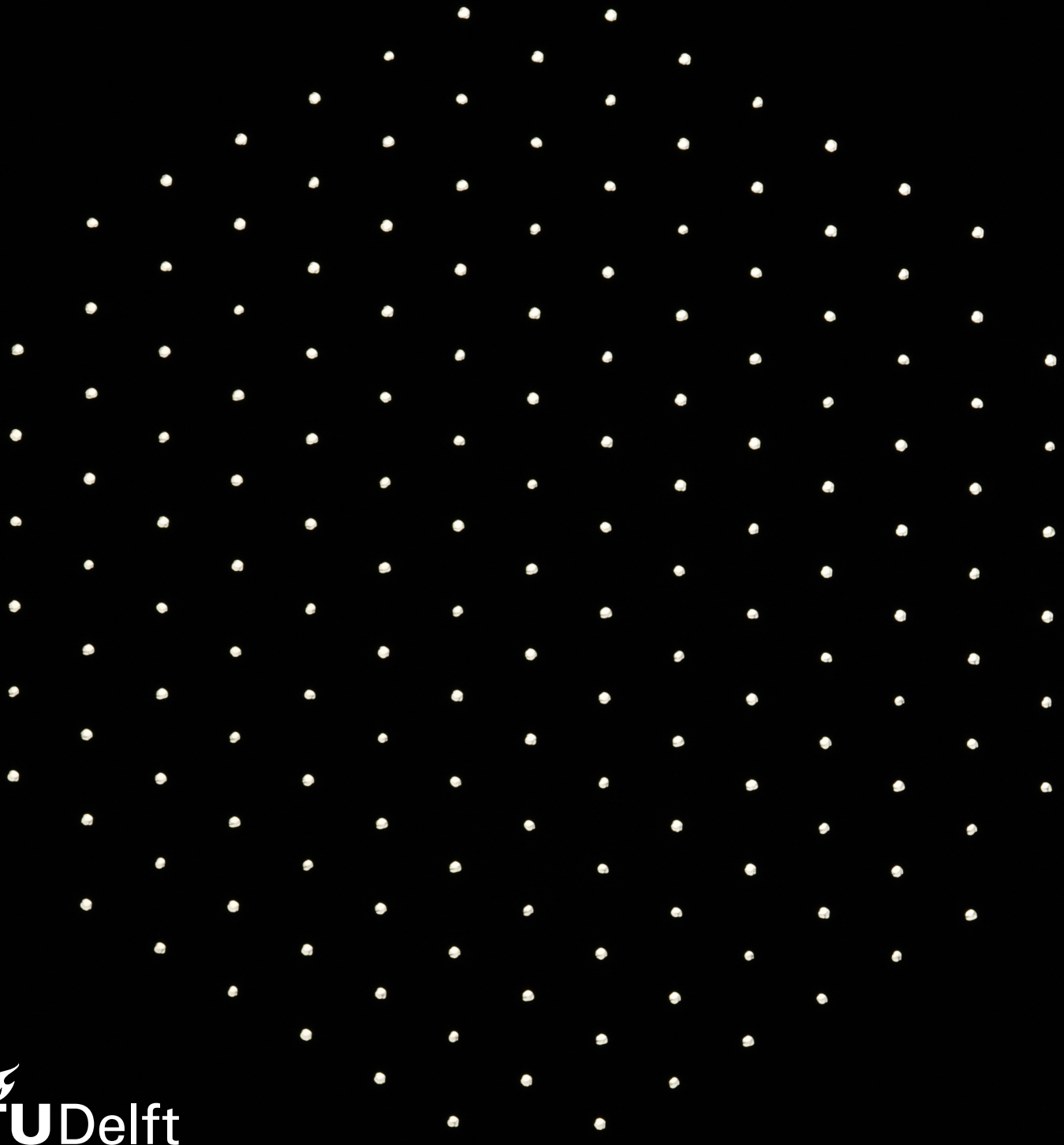

TU Delft

Towards Practical Hybrid Laminar Flow Control

Boundary Layer Stability with Suction and Scalability of Pressure Losses across Perforated Sheets

by

J.P.P. Hemmen

to obtain the degree of Master of Science
at the Delft University of Technology,
to be defended publicly on Thursday, March 29, 2018 at 9:00 AM.

Student number:	4195612	
Project duration:	May 1, 2017–March 29, 2018	
Thesis committee:	Dr. M. Kotsonis	TU Delft, supervisor
	ir. A. F. Rius Vidales	TU Delft, supervisor
	Dr. B. W. van Oudheusden	TU Delft
	Dr. D. Ragni	TU Delft
	R. Cosin	Embraer

An electronic version of this thesis is available at `http://repository.tudelft.nl/`.

TU Delft

Preface

This report was written to fulfill the requirements for obtaining the degree of Master of Science in Aerospace Engineering at Delft University of Technology. This thesis project culminates my studies in Delft, which I started in 2012. I was excited to start this project and it has continually captivated me. Therefore, this project has been extremely valuable and rewarding, but it would not have been possible without others' support.

First of all, I would like to thank my supervisors Marios Kotsonis for his decisiveness and guidance and Alberto Rius Vidales for his inexhaustible enthusiasm. I have greatly enjoyed working with you over the course of this project.

In addition, I would like to thank Embraer for their funding, involvement, and assistance with this project. Furthermore, I would like to thank Leo Molenwijk, Stefan Bernardy, Peter Duyndam, Ed Roessen, Roger Groves, Andrei Anisimov, and Loek Boermans for their technical support for this project.

Finally, I especially thank my parents and my brother, who have always supported me. I dedicate this work to my father.

J.P.P. Hemmen
Delft, March 2018

Abstract

The quest for decreasing fuel consumption of transport aircraft has led to research into skin friction drag reduction, since it is the largest contributor to cruise drag. Skin friction drag can be reduced by applying hybrid laminar flow control (HLFC) to delay boundary layer transition. HLFC combines an active flow control solution with passive airfoil shaping to limit the region where active control is required, thereby reducing complexity and power requirements compared to a fully active system. Boundary layer suction through perforated sheets combined with pressure gradient tailoring was identified as the most technologically mature HLFC solution to suppress the two prime boundary layer instability mechanisms on a swept wing. The feasibility of HLFC was demonstrated in full-scale flight tests, but details of a successful commercial implementation are not publicly available.

This highlights the gap in knowledge regarding the design of an effective HLFC system, which was addressed by the research objective of the present work: to expand the capability to perform the aerodynamic design of a suction-type HLFC component. In order to meet this objective, developments in two main areas were required, namely a transition prediction tool that accounts for suction and a good estimate of the pressure losses across perforated suction surfaces.

The first development was practically translated into the incorporation of boundary layer transpiration into an existing transition prediction tool. Fundamentally, the existing tool was suitable for the adaptation required to design HLFC components, because it is based on linear stability theory combined with the e^N-method, which is the industry standard for transition predictors. However, modifications to its constituting elements, a boundary layer solver and a stability solver, were required before HLFC could be modeled.

The no-penetration boundary condition in the boundary layer solver was adapted to allow transpiration. Additional inputs were created to specify the suction distribution with its own discretization, which is later interpolated and automatically accounts for the position of the stagnation point. A desired option was to have an indirect input of the suction distribution, where the suction rate is determined internally based on a specification of the layout of the suction system. However, this was left as a suggestion for future work, as it requires a good model linking the suction rate to the pressure drop across the surface. The experimental data collected as part of the present research is a starting point.

The stability solver itself did not need modifications, as its boundary conditions remain valid with transpiration. However, suction was found to be incompatible with the preprocessing algorithm of the stability solver. Suction had such a stabilizing effect that the predicted grid of unstable frequencies became too limited: not all unstable frequencies were covered and the grid did not allow N-curves to be integrated along the entire airfoil surface. The preprocessor was modified by negating the influence of suction such that the boundary layer appeared less stable.

The modifications to the boundary layer and stability solvers were verified and validated for the relevant characteristics of HLFC on a transonic transport aircraft. The tested combinations of pressure gradient, wing sweep, and suction showed good agreement with experimental references. The modified preprocessor produced appropriate grids that captured all unstable behavior and enabled integration of N-curves over the entire domain. In conclusion, the modified tools can be used to predict transition for HLFC components, although experimental data will be required to estimate the critical N-factor with suction. The extension to compressible flow and more advanced stability solvers was left as a recommendation for future work.

The second development, estimating the pressure losses across arbitrary HLFC surfaces, was addressed by means of an experimental investigation into the scalability of these losses. While the loss characteristics of specific perforated sheets were traditionally determined experimentally, the present research aimed to assess whether they can be predicted based on a scaled model. To that end, an experiment was designed to measure the pressure drop across a diverse matrix of perforated sheets in a perpendicular flow. As such, the

experimental setup consisted of a pipe, within which a perforated article was placed. Neglecting tangential flow simplified the problem to the following nondimensional governing parameters: the pressure drop coefficient, the open area ratio, the hole aspect ratio, and a hole Reynolds number. The experimental matrix was designed to represent typical HLFC applications according to these similarity parameters.

A set of 18 large-scale perforated articles was manufactured from laser-drilled acrylic sheets. Their geometric properties were measured with an optical setup, consisting of a camera and a light table. The setup captured the entire perforated article in a single image, after which a boundary recognition algorithm was used to determine individual hole properties. The optical setup was calibrated with separate measurements performed with a microscope. A set of three titanium reference articles was made, at the actual scale of typical HLFC components.

The experimental results showed the expected behavior with respect to the similarity parameters. It was found that pressure losses were higher through a converging hole than a diverging hole, reproducing other experimental observations. However, the pressure losses were found to strongly depend on the scale of the perforated article, which was represented by means of the number of holes per unit of open area ratio. A division was made between the frictional pressure losses inside holes and the inertial losses due to flow expansion and contraction across holes. Both pressure losses were greater for the large-scale perforated articles than for the reference articles. However, the inertial losses reached a steady value above a certain number of holes. This limit denotes when the sheet has sufficiently many holes to represent an infinite perforated sheet. In contrast, the frictional losses did not feature such a limit, but instead decreased continually with an increasing number of holes.

Because the inertial and frictional pressure losses are both relevant in the typical operating conditions of HLFC, the scalability of the experimental results is limited. While the inertial losses can be captured with large-scale models, so long as the number of holes is sufficient, an accurate estimate of the frictional losses should be obtained close to the actual size of the intended application. In conclusion, pressure losses across HLFC components will likely still need to be determined experimentally, but it is recommended that more small-scale experiments be conducted, such that the pressure losses across arbitrary HLFC components may be estimated and modeled in the future.

Contents

List of Figures

List of Tables

Nomenclature

Abbreviations

ALT	Attachment line transition
CF	Cross flow
CFD	Computational fluid dynamics
DLR	German Aerospace Center
DNS	Direct numerical simulation
HLFC	Hybrid laminar flow control
LES	Large eddy simulation
LFC	Laminar flow control
NLF	Natural laminar flow
PSE	Parabolized stability equation
TS	Tollmien-Schlichting

Latin Symbols

a	Speed of sound	[m/s]
A	Disturbance amplitude	[m/s]
A	Viscous term in pressure drop model	[-]
B	Nondimensional spanwise wave number	[-]
B	Inertial term in pressure drop model	[-]
C_f	Skin friction coefficient	[-]
C_p	Pressure coefficient	[-]
$C_{\Delta p}$	Pressure drop coefficient	[-]
d	Diameter of suction hole	[m]
D	Pipe diameter	[m]
$\mathbf{f}$	Body forces	[N/m^3]
F	Nondimensional frequency	[-]
G_k	Streamtube parameter used to describe flow into a suction hole	[-]
H	Shape factor	[-]
i	Imaginary number, $i = \sqrt{-1}$	[-]
k	Wave number	[1/m]
l	Blasius length scale	[m]
L	Reference length	[m]
$\dot{m}$	Mass flow	[kg/s]
M	Mach number	[-]
N	Amplification factor	[-]
N	Number of holes	[-]
p	Pressure	[Pa]
Q	Freestream velocity	[m/s]
Q_h	Suction volume flow rate into perforation	[m^3/s]
R	Specific gas constant	[J/(kg·K)]
Re	Reynolds number (Subscripts indicate variable used as reference length)	[-]
s	Coordinate along surface	[m]
S	Sutherland constant	[K]
t	Thickness of sheet	[m]
t	Time	[s]
T	Temperature	[K]
u, U	Velocity component parallel to wall (x-direction)	[m/s]

$\mathbf{u}$	Velocity vector	[m/s]
v	Velocity component normal to wall (y-direction)	[m/s]
$\bar{v}_w$	Suction-blowing parameter	[-]
w, W	Velocity component in spanwise direction (z-direction)	[m/s]
x	Cartesian coordinate parallel to wall and normal to leading edge	[m]
y	Cartesian coordinate normal to wall	[m]
z	Cartesian coordinate in spanwise direction and parallel to leading edge	[m]

Greek Symbols

α	Streamwise wave number	[1/m]
β	Spanwise wave number	[1/m]
β	Open area ratio: ratio of area of perforations to total area of perforated surface	[-]
δ	Boundary layer thickness	[m]
δ^*	Displacement thickness	[m]
θ	Momentum thickness	[m]
Θ	Phase function	[-]
Λ	Sweep angle	[rad]
μ	Dynamic viscosity	[kg/(m·s)]
ν	Kinematic viscosity	[m^2/s]
ρ	Density	[kg/m^3]
σ	Standard deviation	[-]
τ	Shear stress	[N/m^2]
$\boldsymbol{\tau}$	Viscous stress tensor	[N/m^2]
ϕ	Disturbance amplitude, $\hat{v}^*$	[-]
ω	Angular frequency	[rad/s]

Subscripts

e	Quantity evaluated at the edge of the boundary layer
h	Quantity evaluated in a suction hole
i	Imaginary component
r	Real component
s	Reference frame aligned with inviscid streamline
w	Quantity evaluated at the wall
∞	Quantity evaluated in the freestream
0	Reference condition
99	Quantity evaluated at the point where boundary layer velocity has reached 99% of outer flow velocity

Superscripts

$\bullet^*$	Nondimensional quantity

Accents

$\bullet'$	Disturbance quantity (unsteady)
$\bar{\bullet}$	Mean quantity (steady)
$\bar{\bullet}$	Boundary layer transformation
$\hat{\bullet}$	Disturbance mode amplitude
$\tilde{\bullet}$	Dummy variable

1 Introduction

Aircraft manufacturers are under increasing pressure to reduce fuel consumption and emissions. Drag reduction techniques are applied to lower the fuel burn. Given that skin friction drag can make up as much as half of the total aircraft drag [53], its reduction has large potential gains in aerodynamic efficiency. Therefore, the present research focuses on skin friction drag reduction.

Skin friction originates from the boundary layer flow over external surfaces of an aircraft. A turbulent boundary layer features much higher skin friction than a laminar boundary layer. Therefore, a designer can attempt to modify a turbulent boundary layer to reduce its skin friction, for example using riblets [48], which can provide a "modest" reduction [22, p. 98]. Yet, if a turbulent boundary layer is avoided altogether, the expected benefit is even greater. In fact, laminarization has the largest potential benefit to aerodynamic efficiency in cruise for conventional transport aircraft [13]. Therefore, this research considers only this strategy.

One way to reduce skin friction is laminar flow control (LFC). LFC is a broad term encompassing any means to prolong the extent of laminar flow beyond its natural occurrence. A subset of LFC is natural laminar flow (NLF), which is a passive solution to delay boundary layer transition. NLF works by shaping the airfoil to create a favorable pressure gradient that stabilizes the boundary layer and delays transition. However, NLF is not suitable for wings with significant sweep. An active LFC solution is usually required to suppress the instabilities occurring on a swept wing. Such an active system is complex. Therefore, its extent is usually limited but it is then combined with the philosophy of NLF: passive, favorable airfoil shaping is used wherever possible, but it is coupled with an active system where needed to obtain the desired extent of laminar flow. This combination of active and passive solutions is called hybrid laminar flow control (HLFC).

HLFC has received significant attention over the years, culminating in flight tests on full-scale transport aircraft that demonstrated the feasibility of the technology. However, these flight tests only proved the capability of HLFC, but the systems were generally too heavy and complex to yield a net benefit in performance. The bridge to commercial operation was still left to be made, until recently, when Boeing introduced[1] HLFC on its 787-9 model. This is a major milestone for HLFC, being the first time that the practical challenges of HLFC have been overcome to enable the allegedly successful operation on a commercial aircraft.

However, little public information is available about the HLFC system on the Boeing 787, so the design choices and its performance benefits remain unknown. This highlights the apparent gap in public knowledge regarding the design of successful HLFC systems. In particular, it is desired to identify the necessary steps to go from the current knowledge to the capability to design an HLFC component for future aircraft. Among others, two steps are essential to reaching this goal, as illustrated in Fig. 1.1. The first key step is to predict the degree of flow control needed to obtain the desired transition delay, which requires a model accounting for the effect of HLFC on transition. The second key step is to predict the operational power penalty associated to an HLFC system. As HLFC is generally realized using boundary layer suction through a perforated skin, it

[1] `https://www.flightglobal.com/news/articles/farnborough-aero-secrets-of-boeings-new-dreamliner-401784/` Accessed July 27, 2017.

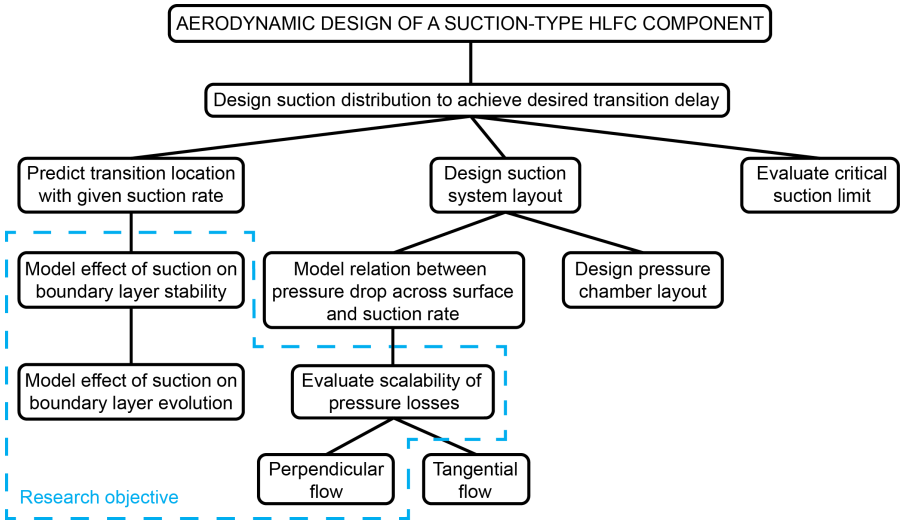

Figure 1.1: Road map for achieving the capability to perform the aerodynamic design of a suction-type HLFC component with constituting goals. The research objective of the present work is highlighted

is desired to estimate the required pressure difference across the surface to achieve the intended suction rate.

Widespread research has focused on the pressure losses across perforated sheets, for applications such as screens and filters, for example in [39]. However, perforated sheets for HLFC are different from the usual applications, in that they feature holes with a very high aspect ratio and that they are less open, in the order of 1%. Research specific to these types of sheets is limited. In fact, the general trend of the pressure losses across HLFC surfaces is known, but the characteristics of specific configurations have historically been determined experimentally. The present research therefore investigates whether these characteristics can be predicted.

1.1. Motivation for Research at TU Delft and Embraer

The motivation for the present research is emphasized by the involvement of Embraer. In fact, Embraer is conducting a joint research project with TU Delft to determine the required steps in order to design laminar flow wings for future aircraft. The research focuses on developing the capability to predict the transition location on laminar flow wings, while taking into account the effect of surface imperfections and the presence of HLFC technology. Regarding HLFC technology, the goals are to determine what technologies need development to achieve HLFC on a future aircraft, to develop a transition prediction tool that accounts for suction, and to assess the feasibility of a suction-type HLFC component by quantifying its associated pressure losses. These goals are addressed in part by the research objective of the present work.

1.2. Research Objective

The preceding discussion highlighted the gap in knowledge of designing viable HLFC components. Besides the challenges regarding implementing and operating HLFC, research is required into predicting the transition location in combination with HLFC and into estimating the operational power penalty of an HLFC component, particularly the pressure losses across suction surfaces. Thus, the research objective is to expand the capability to perform the aerodynamic design of a suction-type hybrid laminar flow control component, by:

1. reviewing the existing literature regarding HLFC;
2. developing a tool capable of assessing how a suction-type HLFC component affects boundary layer stability;
3. performing an experimental study investigating the scalability of the pressure losses across a suction-type HLFC component.

Figure 1.1 illustrates how this research objective fits in the larger context of the goal to develop the capability to perform the aerodynamic design of suction-type HLFC components. For instance, in order to

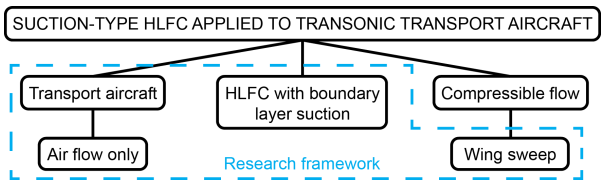

Figure 1.2: Research framework for suction-type HLFC being applied to transonic transport aircraft

predict boundary layer transition with suction, the influence of suction on stability must first be modeled, as in part 2 of the objective. Similarly, before developing a model relating the suction rate to the pressure drop for arbitrary suction surfaces, it must first be established whether the pressure losses across these surfaces are scalable. This is covered by part 3 of the objective. The road map also highlights some aspects of the aerodynamic design of HLFC components that are not addressed in the present research. In fact, the scope of the research is delimited by the framework described in the following section.

1.3. Research Framework

This research is limited to the application of suction-type HLFC technology to a transonic transport aircraft. As illustrated by Fig. 1.2, this implies the following framework. Only transport aircraft are considered, because essentially all commercial air travel falls into this category, so the greatest economic and environmental benefit may be obtained by applying HLFC to this category of aircraft. Furthermore, since aircraft are considered, applications of HLFC suitable to water are outside the scope of this research.

The second restriction is that only HLFC concepts involving boundary layer suction through perforated sheets are considered. This restriction is explained in Sec. 2.6, but the main reason is that those concepts are most technologically mature. From the numerical point of view, boundary layer suction or injection is only a change in sign in the boundary conditions, so this research uses the broader term ‘transpiration’ throughout.

Given that transonic aircraft are considered, compressibility effects are a key element. However, including compressible flow was outside the scope of the present research, but is recommended for future work. Still, transonic aircraft feature a sweep angle, which introduces an additional boundary layer instability mechanism, which hinders the sustainment of laminar flow. Thus, wing sweep is included in the present work.

Further restrictions are underscored by Fig. 1.1. For example, only the pressure losses across perforated sheets in perpendicular flow are investigated. Section 5.2 explains the reason more clearly, but the primary argument is that eliminating tangential flow allows a significant simplification of the experimental setup, matrix, and analysis. Furthermore, the present research is limited to the perforated suction surface of an HLFC component, since it has common features in most applications of HLFC. On the contrary, the other elements of a suction system, such as the pressure chamber layout and suction pumps, are specific to its application and are hence outside the scope of this research. Finally, evaluating the critical suction limit is essential for the design of an HLFC component, but is also outside the scope of the present work.

1.4. Research Questions

From the research objective set in Sec. 1.2 and the framework delimited in Sec. 1.3, it is possible to deduce the following set of research questions. Similar to the research objective, there are three key questions, each having their own set of subquestions.

1. What is the principle behind achieving hybrid laminar flow control and modeling its influence on boundary layer transition?

   (a) How can HLFC be used to affect boundary layer transition on a transport aircraft in the transonic flight regime?

   (b) What is the most feasible way to implement HLFC technology on a transonic transport aircraft and what are its limitations?

   (c) How can the effects of boundary layer transpiration on transition be modeled effectively?

2. Upon implementing a transpiration model into the existing transition prediction tool, will the tool be sufficient in order to perform the aerodynamic design of an HLFC component?
   (a) How does the existing transition prediction tool work?
   (b) What modifications to the existing tool are required in order to predict boundary layer transition with boundary layer transpiration?
   (c) How accurately does the tool predict the boundary layer properties and stability for suitable validation cases?
   (d) What further steps are required in order to perform the aerodynamic design of an HLFC component using this tool?
3. Are pressure losses across perforated surfaces of suction-type HLFC components scalable?
   (a) What factors affect the pressure loss across perforated sheets?
   (b) What nondimensional parameters characterize the flow through a suction surface?
   (c) How do typical HLFC components look in terms of the parameters resulting from 3b?
   (d) How has the pressure loss across perforated surfaces been modeled effectively in literature?

For some of the research questions, some 'vague' terms have been purposefully introduced. They attempt to steer the answer to the question in a direction such that a useful solution will be obtained. For starters, research question 1b refers to the 'near' future. While the meaning of 'near' is unclear, this term is intended to identify the HLFC concept that is most technologically mature to be implemented in practice.

A second example is found in research question 1c, which refers to an 'effective' way of predicting transition. This term was introduced to direct the research towards those methods that predict transition accurately for a wide range of applications, while being manageable in terms of computational effort, such that they can be used during the initial design stage, for example with optimization procedures. This also affects the selection of the model in Fig. 1.1 which will be used to assess the effect of suction on boundary layer stability.

Furthermore, research question 2 asks whether the tool will be 'sufficient' for design purposes. Not only does this term imply an assessment of the accuracy of the tool, like in question 2c, but also suggests a reflection on the limitations of the tool (question 2d).

Finally, question 2c refers to 'suitable' validation cases. These cases should be representative of a transonic transport aircraft. According to Fig. 1.2, this implies that the validation cases should involve boundary layer suction and the multiple transition mechanisms that can occur on this type of aircraft.

1.5. Structure

This report is structured to follow roughly the three elements of the research objective (Sec. 1.2). First, the fundamentals of HLFC are introduced in Chap. 2, along with a review of the practical concerns of its implementation. Then, the remainder of the report is divided into the two primary areas of research: the numerical incorporation of boundary layer transpiration into an existing transition prediction tool and an experimental investigation into the scalability of pressure losses across perforated sheets.

The numerical study starts in Chap. 3, which reviews transition prediction methods and subsequently describes the methodology used to adapt the existing transition prediction tool to incorporate boundary layer transpiration. These modifications were verified and validated in Chap. 4.

The experimental research starts in Chap. 5, which explores the governing parameters and boundary conditions for suction flow through perforated sheets. Moreover, it summarizes the typical features of HLFC suction surfaces, which was used to design the experiment. Chapter 6 describes the experimental setup, consisting of the rig to measure the pressure drop across perforated sheets and the optical setup to evaluate their geometric properties. Subsequently, Chap. 7 presents and analyzes the experimental results.

Finally, Chap. 8 concludes the report. Furthermore, it provides recommendations for future work.

2

Fundamentals of Hybrid Laminar Flow Control

Hybrid laminar flow control (HLFC) was briefly introduced in Chap. 1. This chapter explores it in more detail, starting in Sec. 2.1. To describe how HLFC affects a boundary layer, the fundamentals of boundary layer flow are covered first in Sec. 2.2. Then, Sec. 2.3 describes the types of flow instabilities that influence laminar-to-turbulent boundary layer transition. Afterwards, Sec. 2.4 explains how HLFC can be used to control these flow instabilities. Next, Sec. 2.5 discusses how the drag of an aircraft component is affected by HLFC. Subsequently, Sec. 2.6 reviews various concepts for implementing HLFC. Then, Sec. 2.7 discusses the aircraft components on which implementing HLFC is suitable. Practical examples of HLFC are summarized in Sec. 2.8. Furthermore, Sec. 2.9 extracts the relevant elements for HLFC from the research on boundary layer suction performed at TU Delft. Finally, the challenges of HLFC technology are examined in Sec. 2.10.

2.1. Hybrid Laminar Flow Control

The aim of laminar flow control (LFC) is to prolong the extent of laminar flow beyond what is possible naturally [31]. Natural laminar flow (NLF) is a passive way of maintaining laminar flow, by means of shaping the airfoil such that a prolonged area of favorable pressure gradient is created. This suppresses the growth of Tollmien-Schlichting instabilities (Sec. 2.3.1), in turn delaying boundary layer transition, leading to a decrease in skin friction. The NLF technique is ineffective on swept wings, because transition on a swept wing is dominated by the cross flow instability, which is not stabilized by a favorable pressure gradient (Sec. 2.3).

Thus, for swept wings, an active system is required: laminar flow control [13]. The common solution is to apply boundary layer suction over the entire airfoil, but other means are also possible (Sec. 2.6). Laminar flow control is complex, as it requires an active system (suction) which covers the entire airfoil surface.

Hybrid laminar flow control (HLFC) attempts to reduce the complexity of LFC while maintaining most of its benefits. To that end, active flow control is applied to a smaller region than for LFC, usually upstream of the front spar [31]. Behind the controlled area, the airfoil shape is tailored to create a favorable pressure gradient to passively promote natural laminar flow. This hybrid solution exploits the benefits of NLF to limit the area where active flow control is required, thereby drastically reducing complexity compared to full LFC.

The differences between NLF, LFC, and HLFC are visualized in Fig. 2.1. Note the favorable pressure gradient for over half the chord length on the NLF section. For LFC, suction is applied over the entire surface, while for HLFC, the area of suction is limited to a small region around the leading edge, maintaining the favorable pressure gradient over a large part of the surface, as with the NLF section.

Increasing the extent of laminar flow using HLFC reduces the skin friction, resulting in an overall drag reduction for the aircraft. The benefit of laminar flow may be understood through boundary layer theory.

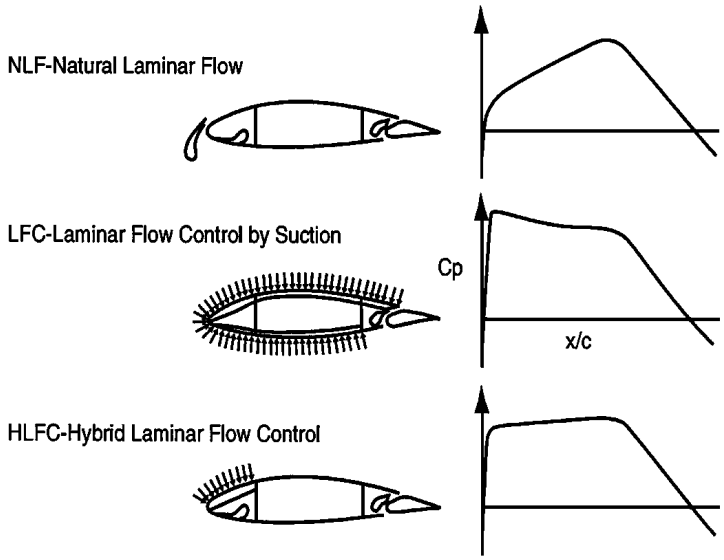

Figure 2.1: Schematics of natural laminar flow, laminar flow control, and hybrid laminar flow control concepts with corresponding suction areas and pressure distributions [31]

2.2. Fundamentals of Boundary Layer Theory

In absence of viscosity, there is a potential flow around an object. Potential flows feature a finite velocity at the interface of the fluid and the surface. In other words, the fluid slips along the wall, which implies a discontinuous velocity profile. In real, viscous flows, no such discontinuity can exist because the fluid is regarded as a continuum [17]. In fact, it is observed that the fluid sticks to the wall [50]. This is the no-slip condition.

Due to the no-slip condition, there must be a transition from zero velocity at the wall to a finite velocity in the outer flow. Viscosity takes care of this transition. Viscosity causes the transport of momentum perpendicular to the primary flow direction [50]. The region of transition between the no-slip condition and the outer velocity divides the flow into two parts. In the outer part of the flow, the effect of viscosity is negligible, and the flow behaves as if it is inviscid. The second region is a thin region close to the wall where the effects of viscosity are significant [50]. In fact, the effects of viscosity are of the same order as the inertial effects in this region. Thus, this region is called the 'frictional layer' or 'boundary layer' [50].

Since the division between the outer flow and the boundary layer is governed by the viscous and inertial forces, the Reynolds number is an important parameter. It represents the ratio of the inertial forces to the viscous forces [17], as shown in Eq. (2.1). At very high Reynolds numbers, the effect of viscosity cannot be neglected, because there is always a region where viscous effects are relevant [17]. Even though viscosity can be neglected in most of the flow field, the effect of viscosity is concentrated in the thin boundary layer. Thus, high-Reynolds number flows are a small perturbation away from the inviscid limiting case ($Re \rightarrow \infty$) [50].

$$Re = \frac{U_\infty L}{\nu} \tag{2.1}$$

Defining the boundary layer thickness is not straightforward because there is no sudden division between the boundary layer and the outer flow [50]. Therefore, an arbitrary definition exists, which states that the boundary layer ends at 99% of the outer flow velocity (U_e) [50], indicated by δ_{99}. A more tangible definition of the boundary layer thickness is the displacement thickness, δ^*, given by Eq. (2.2).

$$\delta^* = \int_0^\infty \left(1 - \frac{\rho u}{\rho_e U_e}\right) dy \tag{2.2}$$

As its name suggests, the boundary layer displacement thickness describes the displacement effect of the boundary layer on the outer flow. The magnitude of δ^* describes how far away from the wall the inviscid streamlines should be placed in order to obtain the same mass flow in the boundary layer [17]. A second important boundary layer parameter is the momentum thickness, θ, given by Eq. (2.3). It is a measure of the momentum deficit existing in the boundary layer compared to the inviscid outer flow.

$$\theta = \int_0^\infty \frac{\rho u}{\rho_e U_e}\left(1 - \frac{u}{U_e}\right) dy \tag{2.3}$$

The ratio of the displacement thickness to the momentum thickness is a measure of the 'fullness' of the boundary layer profile. It is called the shape factor, H, given by Eq. (2.4). Since δ^* is always larger than θ, H is always greater than unity. The lower the shape factor, the fuller the boundary layer profile.

$$H = \frac{\delta^*}{\theta} \tag{2.4}$$

Due to the effect of viscosity and the no-slip condition, there will be a shear force at the wall. This shear force is proportional to the gradient of the velocity profile at the wall. It is given by Eq. (2.5).

$$\tau_w = \mu \left.\frac{\partial u}{\partial y}\right|_{y=0} \tag{2.5}$$

The wall shear stress can be made nondimensional by dividing it by the dynamic pressure of the outer flow. This results in the skin friction coefficient given by Eq. (2.6).

$$C_f = \frac{\tau_w}{\frac{1}{2}\rho_e U_e^2} \tag{2.6}$$

The skin friction drag follows by integrating the wall shear stress along the entire surface. The next section presents the effect of the state of the boundary layer—laminar or turbulent—on the skin friction. It will become apparent why a laminar boundary layer exhibits lower skin friction than a turbulent boundary layer.

2.2.1. Laminar Boundary Layer

The laminar flow state may be described as a "layered flow, where layers of fluid move with different velocities without great exchange of fluid particles perpendicular to the flow direction" [50, p. 13]. In other words, laminar flow is very orderly, implying limited mixing between streamlines inside a laminar boundary layer. Therefore, the flow properties change gradually from stationary at the wall to the outer flow. Consequently, the region of retarded flow is relatively large for a laminar boundary layer, as illustrated in Fig. 2.2.

2.2.2. Turbulent Boundary Layer

In contrast to a laminar boundary layer, a turbulent boundary layer exhibits random fluctuations, enhancing momentum transfer between streamlines. As a result, mixing is increased in a turbulent flow [17]. Consequently, regions in the boundary layer with different flow properties are condensed, compared to laminar flow [17]. Therefore, the region of retarded flow remains much closer to the wall than for laminar flow, to which the effects of viscosity are confined. This is called the 'viscous sublayer' [50].

Outside of the viscous sublayer, the remaining part of the turbulent boundary layer is more uniform than a laminar boundary layer, at a velocity close to the outer velocity, as indicated by Fig. 2.2. Therefore, the turbulent velocity profile in Fig. 2.2 is fuller than the laminar one. Note that, near the wall, the velocity in the turbulent boundary layer approaches the outer velocity more rapidly than for the laminar boundary layer.

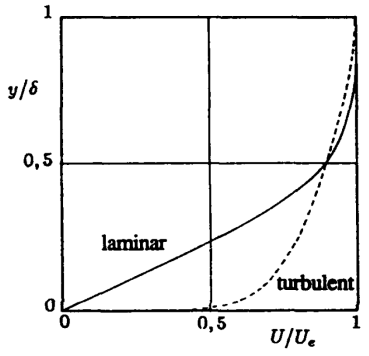

Figure 2.2: Velocity profiles in a laminar and turbulent boundary layer [17]

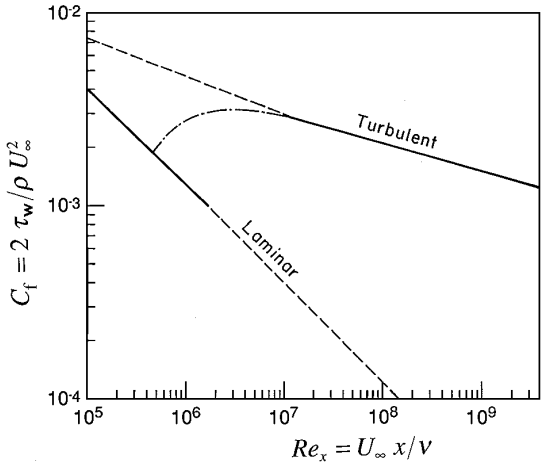

Figure 2.3: Skin friction coefficient as function of Reynolds number on a flat plate for the laminar and turbulent boundary layer [22]

As a consequence, the velocity gradient of the turbulent velocity profile at the wall is much greater than that of the laminar profile. Thus, recalling Eq. (2.5), the wall shear stress, and thus skin friction, is much higher for the turbulent boundary layer. This point is illustrated in Fig. 2.3. The curve connecting the laminar to the turbulent curve denotes the transition process. Thus, if transition could be delayed, this would yield the benefit of a lower skin friction. In fact, this is the goal of hybrid laminar flow control. The next section explores why boundary layer transition occurs and how the transition process may be controlled and delayed.

2.3. Boundary Layer Transition

Boundary layer transition is the process by which a boundary layer changes its state from laminar to turbulent. Transition occurs because laminar flow is unstable above a certain Reynolds number [78]. This is the 'critical Reynolds number.' The critical Reynolds number is such that transition occurs on all full-size aircraft, because of the large length scale and therefore Reynolds number associated to such aircraft.

The transition process is not instantaneous. Rather, it encompasses a region of the flow, in space and time, where disturbances are amplified. Disturbances enter the boundary layer due to disturbances in the freestream [49]. These will form perturbations to the mean flow of the boundary layer which start to grow when the boundary layer becomes unstable [49]. This process is called 'receptivity.' Once these disturbances have amplified sufficiently, turbulent spots form, after which these turn into turbulent wedges. The final step is the complete breakdown into spanwise turbulent flow. Then, the transition process is considered complete.

Transition by means of amplification of boundary layer oscillations consists of a linear stage and a nonlinear stage. The linear amplification of disturbances is weak [49] and is thus the slowest step of transition [22]. At a certain disturbance amplitude, nonlinear effects take over. These are secondary instabilities [49]. When they occur, the transition process is quickly completed [22]. If the initial disturbances are sufficiently strong, the linear amplification of disturbances can be bypassed [49]. This is appropriately called 'bypass' transition. Bypass transition is much faster since the slow, linear stage is completely circumvented.

Thus, if bypass transition can be avoided, the linear instability modes should be studied [13]. For a transonic, swept wing, the flow instabilities described below are relevant in the boundary layer transition process.

2.3.1. Tollmien-Schlichting Instability

Tollmien-Schlichting (TS) waves are two-dimensional waves traveling in the streamwise direction [22]. During the linear amplification stage, TS waves grow in amplitude. At a certain amplitude, they will develop three-dimensional spanwise variations due to a secondary instability [22]. Eventually, they break down into turbulence. Since TS waves are a streamwise instability, any wing can generally exhibit TS instabilities. However, TS waves tend to dominate transition only between wing sweep angles of 0 and 25 degrees [31].

For incompressible flow, two-dimensional waves are the most unstable. This was proven by Squire, who

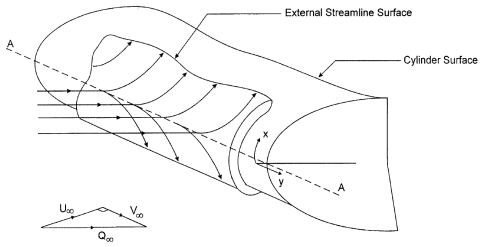

Figure 2.4: Flow around leading edge of swept wing [62]. Attachment line indicated by section A–A

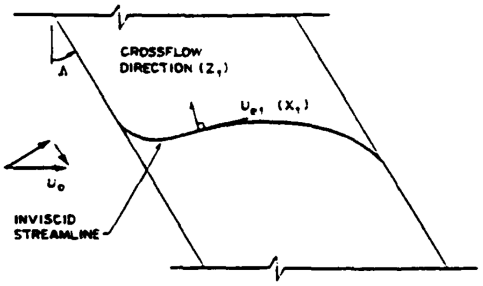

Figure 2.5: Inviscid streamline over infinite swept wing [49]

showed that any three-dimensional instability would already have occurred as a two-dimensional instability at a lower Reynolds number [66]. When compressibility is taken into account, the transition criteria do not differ much from the incompressible results [42, 49]. In fact, up to a Mach number of 0.9, the dominant direction of wave amplification remains the two-dimensional direction [42]. However, for transonic flight conditions, in the area of the airfoil where $M > 0.9$, the most unstable direction for amplification of disturbances moves away from the streamwise direction.

A favorable pressure gradient stabilizes TS instabilities [13]. In fact, this is the concept behind NLF wings (Sec. 2.1), where a large section of the airfoil exhibits a favorable pressure gradient in order to suppress the growth of TS waves and consequently to delay laminar-to-turbulent boundary layer transition.

2.3.2. Cross Flow Instability

Swept wings exhibit another type of instability: the cross flow (CF) instability. It originates from the spanwise pressure gradient that exists on a swept wing, in turn induced by the streamwise pressure gradient.

The origin of the spanwise pressure gradient may be reasoned from the effect a sweep angle has on the flow around an infinite wing, having the same streamwise pressure distribution at every spanwise location. For a straight wing, there is no pressure difference between neighboring airfoil sections. The behavior changes with a sweep angle. In this case, despite having a constant pressure distribution along the span, the displacement in the streamwise direction creates a spanwise pressure gradient between neighboring sections.

On a swept wing, there is no stagnation point, as shown in Fig. 2.4. Instead, the flow over the upper and lower surfaces is delimited by a line of spanwise flow: the attachment line [62]. On the attachment line, the flow velocity normal to the leading edge is brought to zero, but the spanwise component of the freestream velocity remains, as a consequence of the sweep angle. Because the pressure decreases around the nose of the airfoil, the attachment line flow will leave its spanwise direction and turn into the chordwise direction [52], resulting in highly three-dimensional flow around the leading edge.

Behind the attachment line, there is a region of decreasing pressure. On a back-swept wing, when traveling in the streamwise direction in this region of negative pressure gradient, the pressure is lower on the inboard side than on the outboard side, creating a spanwise pressure gradient that causes the inviscid streamline leaving the attachment line to turn inboard. This is visualized in the initial part of Fig. 2.5. The opposite occurs near the trailing edge of the airfoil.

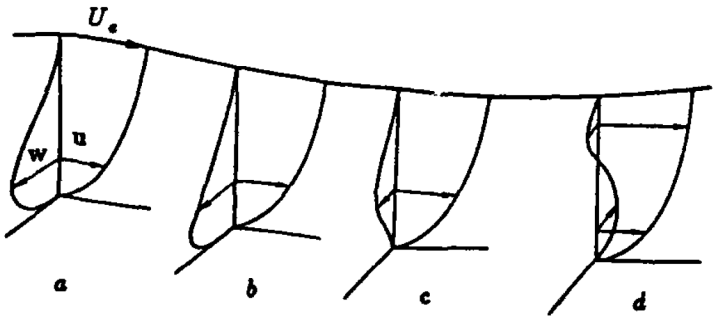

Figure 2.6: Cross flow velocity profiles developing over swept wing following the inviscid streamline [17]. w pointing in inboard direction

The boundary layer cross flow component is defined as the velocity normal to the local inviscid streamline direction [49]. Momentum in the boundary layer is lower than in the outer flow, causing a stronger response to pressure gradients. Thus, when the inviscid streamline is turned inboard, the boundary layer turns even more inboard. This leads to a boundary layer cross flow component in the inboard direction, as shown in Fig. 2.6 by profile 'a.' The cross flow velocity in profiles 'a' and 'b' is largest near the wall, being most affected by the spanwise pressure gradient, because the momentum in the boundary layer is lowest here.

By definition, the cross flow velocity must be zero at the inviscid streamline and at the wall. Given that the cross flow component has a nonzero magnitude inside the boundary layer, there must be at least one inflection point in the cross flow velocity profile [62]. An inflection point in the boundary layer profile is unstable [78], which leads to the cross flow instability. The result is the formation of cross flow vortices in the streamwise direction which all rotate in the same direction [49].

While TS instabilities are stabilized by a favorable pressure gradient, CF instabilities are destabilized by it [22]. So, a 'favorable' pressure gradient is actually not favorable for cross flow. Actually, any pressure gradient is destabilizing for cross flow [59]. So, for cross flow, it would be best to have no pressure gradient on the wing at all. However, this is not possible, because the wing is intended to create lift. Still, it is possible to tailor the airfoil, so that the growth of CF instabilities is suppressed [59], as discussed in Sec. 5.6.

Cross flow instabilities are likely to influence transition above a sweep angle of 25 degrees. Up to a sweep angle of 30 to 35 degrees, both TS instabilities and CF instabilities influence boundary layer transition [31]. Beyond that, CF disturbances dominate transition [31]. Given that transonic transport aircraft typically have sweep angles in the order of 30 degrees [69], considering cross flow instabilities is crucial.

2.3.3. Attachment Line Transition

Attachment line transition (ALT) is also referred to in literature as 'leading edge contamination' or any variation of these terms. They all refer to the same phenomenon, namely the 'contamination' of the attachment line on swept wings by the turbulent boundary layer from the fuselage. Turbulence coming from the boundary layer on the fuselage can be convected along the attachment line of the wing [53]. This can cause the entire wing to become turbulent [17]. Leading edge contamination causes transition without a initial stage of linear amplification of the disturbances [14]. ALT is thus a kind of bypass transition.

Because ALT can cause turbulent flow all over the wing, it has a strong detrimental effect on the drag. Therefore, it is important that ALT be avoided on swept wings. A trivial solution would be to reduce the sweep angle, but the sweep angle is needed to limit wave drag. Another option would be to relaminarize the flow on the attachment line by means of suction [31]. However, since the suction requirements for relaminarization are much higher than for suppressing disturbances in laminar flow, this is not a viable solution.

A better solution to avoid ALT is to make the leading edge radius sharp, such that strong acceleration around the nose draws the disturbances away from the leading edge [52]. Then, the turbulence is not allowed to convect along the attachment line anymore, preventing the wing from becoming fully turbulent.

Another solution is to install a Gaster bump on the wing leading edge, near the root, but outside the

fuselage boundary layer. It aims to create a stagnation point on the bump, which allows the turbulence to be diverted and allows a new, laminar boundary layer to develop behind the bump [51]. For a transonic transport aircraft, it will be necessary to use a device like a Gaster bump to avoid ALT [31, 51].

2.3.4. Görtler Vortices

Görtler vortices are a kind of instability that can occur on concave surfaces. Like for CF vortices, Görtler vortices are oriented in the streamwise direction [49]. However, unlike CF vortices, Görtler vortices are counter-rotating [49]. Görtler vortices are insensitive to pressure gradients [22].

In practice, supercritical airfoils on transonic transport aircraft typically have a concave surface in the rear of the lower surface to create aft loading. However, this region is far back on the airfoil, so the potential gains from laminarization are small. For a vertical stabilizer, the airfoil would be symmetric, which is unlikely to have concave surfaces. Thus, Görtler vortices have limited practical importance on transport aircraft.

2.4. Effect of HLFC on Transition Mechanisms

HLFC aims to control the instability mechanisms described in Sec. 2.3 to delay boundary layer transition. These mechanisms are related to the velocity profile, which in turn is controlled with HLFC. A necessary condition for inviscid instability is that the inviscid velocity profile have an inflection point [78]. Thus, an inviscid velocity profile is stable if it does not have an inflection point. However, a viscous velocity profile can be unstable even without an inflection point [78]. Still, an inflection point remains a strong indication of instability. Because the curvature of a boundary layer velocity profile governs the existence of an inflection point, boundary layer instability can be characterized by it. In fact, the curvature of the velocity profile is a major term in the Orr-Sommerfeld equation (Sec. 3.3.2), which is used to describe boundary layer stability.

The influence of the curvature on boundary layer stability is best illustrated by means of the streamwise instability that occurs when a boundary layer loses momentum. Following Fig. 2.7, a full boundary layer profile (profile a) features a large velocity gradient at the wall which decreases further away from the wall. Therefore, the curvature of the velocity profile is negative near the wall. Its magnitude decreases when the boundary layer profile is less full (profile b). At some point when the boundary layer is even less full (profiles c–e), the gradient of the velocity profile near the wall is so low such that a positive curvature is required to reach the edge velocity. This leads to an inflection point, and therefore an unstable state. In order to counter instability, the velocity profile should be made more full. In other words, the curvature of the velocity profile at the wall should be reduced increase the stability of the boundary layer.

The parameters that affect the curvature of the velocity profile at the wall can be identified from the two-dimensional, streamwise boundary layer momentum equation. Shown in Eq. (2.7), the terms on the left-hand side influence the curvature, and are therefore considered 'stability modifiers' following Gad-el-Hak [22] or 'transition modifiers' [3]. Three stability modifiers can be identified, namely the normal velocity at the wall (v_w), the pressure gradient in streamwise direction ($\frac{\partial p}{\partial x}$), and the viscosity gradient in the wall-normal direction ($\frac{\partial \mu}{\partial y}$). A normal velocity at the wall can be obtained by means of transpiration: injection or suction of fluid through the wall. A viscosity gradient can be obtained by means of a temperature gradient, because the viscosity of a fluid is related to its temperature ($\frac{\partial \mu}{\partial y} = \frac{\partial \mu}{\partial T}\frac{\partial T}{\partial y}$). For gases, the viscosity increases with temperature [22]. Given that $\frac{\partial^2 u}{\partial y^2}$ should be negative or decreased for stability against TS waves, favorable are therefore: suction ($v_w < 0$), favorable pressure gradient ($\frac{\partial p}{\partial x} < 0$), and wall cooling ($\frac{\partial \mu}{\partial T}, \frac{\partial T}{\partial y} > 0$) for gases.

$$\rho_w v_w \left.\frac{\partial u}{\partial y}\right|_{y=0} + \left.\frac{\partial p}{\partial x}\right|_{y=0} - \left.\frac{\partial \mu}{\partial y}\right|_{y=0}\left.\frac{\partial u}{\partial y}\right|_{y=0} = \mu \left.\frac{\partial^2 u}{\partial y^2}\right|_{y=0} \tag{2.7}$$

The aforementioned stability modifiers affect the other instability mechanisms differently than for the TS instability. In fact, CF instabilities are excited by any pressure gradient, as stated in Sec. 2.3.2, so a favorable pressure gradient for TS waves is not favorable for CF. Furthermore, CF instabilities are insensitive to wall temperature, but are stabilized by suction [13]. For Görtler instabilities, the shape of the surface (concave) is more important that the pressure gradient, since the concavity of the surfaces causes the instability. Görtler

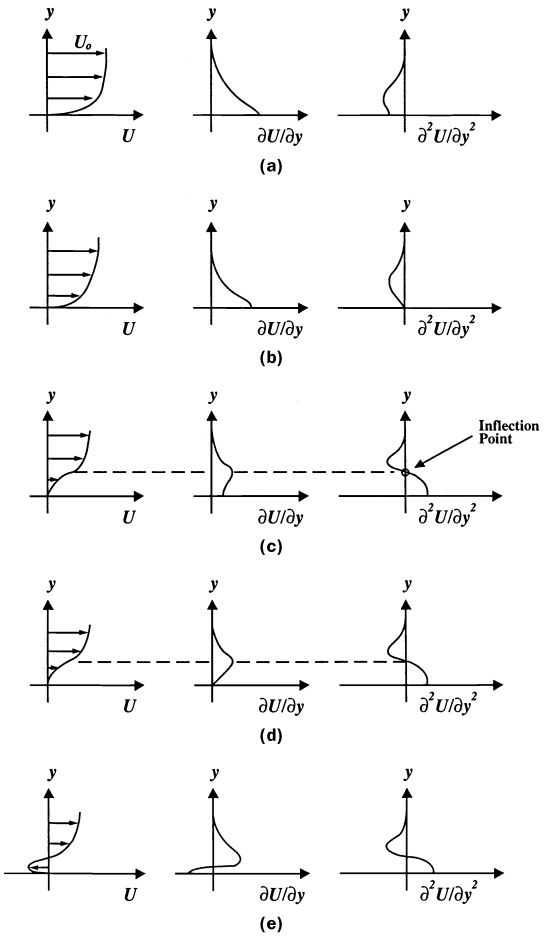

Figure 2.7: Boundary layer velocity profiles (left) along with the gradient of the profile (center) and the curvature of the profile (right) [22]. The velocity profiles are progressively less full from (a) to (e). Profile (a) is full, (b) is a Blasius profile on a flat plate, (c) has an inflection point, (d) is on the verge of separation, and (e) is separated with backflow

instabilities are insensitive to wall temperature and stabilized by suction [13]. ALT is a kind of bypass transition, so there are no stability modifiers to be considered. In conclusion, suction is stabilizing for all transition mechanisms, wall temperature has a varying effectiveness on the transition mechanisms, while a favorable pressure gradient has conflicting effects, being stabilizing for TS waves and destabilizing for CF.

2.5. Effect of HLFC on Drag

Considering only the prolonged extent of laminar flow realized by HLFC does not paint the complete picture. In fact, by making the boundary layer profile fuller to make it more stable, the local skin friction increases, which seems counterintuitive to the objective of HLFC. But, the increased boundary layer stability allows the region of laminar flow to be extended, thereby reducing the region of high-skin-friction turbulent flow. So, while a fuller boundary layer increases the local skin friction, the delayed transition to turbulent flow avoids its much higher skin friction, resulting in a net reduction in skin friction drag.

Taking into account the turbulent skin friction diminishes the benefit of prolonging the extent of laminar flow [65]. In the first place, skin friction is highest at the start of turbulent flow, as illustrated in Fig. 2.3, because the turbulent velocity profile is fullest there. This initial part with comparatively high skin friction is always maintained, so that the relative importance of the turbulent skin friction increases. Furthermore, when the region of laminar flow is extended, the turbulent boundary layer starts off with a smaller thickness. Therefore, the velocity gradient and turbulent skin friction are locally higher than without flow control. Thus, at the same chordwise location in the turbulent part of the boundary layer, the skin friction is higher for a longer extent of laminar flow before the turbulent part [65].

Fortunately, the increased turbulent skin friction is outweighed by a reduction in pressure drag [65]. Because HLFC extends laminar flow, the boundary layer thickness is reduced, resulting in a smaller displacement effect and thus lower pressure drag. An additional contributing factor to the drag of HLFC components is the drag associated to its operation. For example, HLFC using suction requires a pump, which introduces losses, but even passive suction systems create a form of drag. This is discussed in more detail in Sec. 5.6.

2.6. Laminar Flow Control Concepts

In general, concepts for LFC can be classified as passive or active. Passive solutions do not require any source of power, while active solutions do. Active solutions can be split up into systems with a response constant in time or systems with a time-varying response. The former category can be called 'semi-active' [15] or 'predetermined' [22], where the output does not depend on any sensory inputs. The latter category can also be called 'reactive' [22], in that there is some form of control: the output is adjusted based on a measurement.

2.6.1. Passive Laminar Flow Control Concepts

This section examines pressure gradient tailoring and compliant coatings as solutions for passive LFC.

Pressure Gradient

Inherent to the 'hybrid' part of HLFC is passive airfoil shaping to create a favorable pressure gradient. This solution is most effective at suppressing TS waves, because CF instabilities are induced by any pressure gradient. For laminar flow control on a swept wing, therefore, an additional type of flow control is needed. Still, because airfoil shaping is a passive solution, it remains an essential part of any HLFC component.

Compliant Coatings

Compliant walls are a passive LFC solution, intended to create a favorable interaction with the boundary layer flow [22]. One way to realize a compliant wall is to apply a compliant coating. This is a simple solution, because it can be applied relatively easily to existing vehicles and does not require any internal systems. Compliant coatings have been demonstrated to delay transition in water flows, but they are unfortunately less effective in gas flows [22]. Therefore, compliant coatings are not suitable for HLFC on an aircraft.

2.6.2. Active Laminar Flow Control Concepts

This section investigates solutions for active laminar flow control, namely wall heating and cooling, plasma actuators, and boundary layer transpiration.

Wall Heating and Cooling

A temperature variation at the wall induces a corresponding gradient in viscosity and also in density for compressible flows. This variation in viscosity can be used to damp TS waves. In fact, wall cooling is stabilizing for TS waves in air. Unfortunately, wall cooling is less effective for controlling CF instabilities [22], because a cross flow velocity profile is always inflectional, making it inherently unstable (Sec. 2.3.2). Furthermore, wall cooling in air is hindered by poor thermal coupling due to the low Prandtl number [22]. Water—having a higher Prandtl number—requires a much lower temperature variation for the same viscosity gradient. A practical issue with wall cooling is the need for a heat sink to cool the wall below the ambient temperature. This requires a cryogenic fuel, such as hydrogen [3, 22], which is not currently implemented on commercial aircraft. More advanced techniques using local wall heating and cooling are described in [15], but these are not technologically mature. Because of the aforementioned limitations, wall cooling is not a feasible solution for HLFC on a transonic aircraft in the near future.

Plasma Actuators

The stability of the laminar boundary layer is affected largely by the curvature of the velocity profile near the wall. Because the momentum is low near the wall, only a small change in the boundary layer velocity profile can affect the stability significantly. Plasma actuators are able to provide this small change in the boundary layer momentum near the wall, as illustrated by Fig. 2.8, and are thus a candidate for laminar flow control. Concepts to damp TS and CF instabilities are described in [15]. Their use has also been investigated at TU Delft, both numerically and experimentally. However, this technology is not yet ready to be implemented on industrial applications, as also reported in [15].

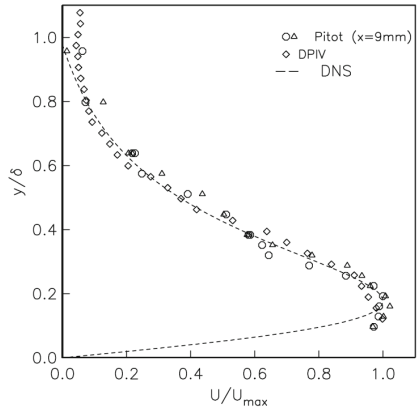

Figure 2.8: Example of mean velocity profile induced by a plasma actuator [16]

Boundary Layer Transpiration

Boundary layer transpiration as a way of LFC has been around for a long time. Typically boundary layer suction is used to prolong the extent of laminar flow. A distinction can be made between discrete and continuous suction: the former applies suction only at distinct locations, while the latter applies suction over an entire area. For discrete suction, there are again two options: slit suction and slot suction. They differ in the way fluid is extracted from the boundary layer. Slit and slot suction extract fluid in the directions tangential and perpendicular to the wall, respectively.

Continuous suction aims to create flow normal to the surface. Ideally, this motion would be unobstructed, but there must be some kind of supporting structure. Since the normal velocity must be zero on the solid structure between pores, the ideal suction surface does not exist [26]. Two options exist for enabling normal motion through a surface: a porous surface or a perforated sheet. The former is a material with "labyrinth-like passageways" [19, p. 8], while the latter is a material containing holes passing straight through it.

Slit Suction

Slit suction works by removing a part or all of the boundary layer in the tangential direction, as illustrated in Fig. 2.9a. By removing the fluid with the lowest momentum, a new or fuller laminar boundary layer will form downstream of the slit, which can withstand a larger adverse pressure gradient than without suction, prolonging the extent of laminar flow. However, the boundary layer that forms downstream of the slit is very thin. Hence, it becomes susceptible to surface roughness when an excessive portion of the boundary layer is removed [26]. This could cause premature transition, which is counterproductive.

(a) Tangential suction (b) Tangential blowing

Figure 2.9: Schematic of suction and blowing through slits [50]

Another option for slits is tangential blowing, as illustrated in Fig. 2.9b, where fluid is injected into the region of lowest momentum in the boundary layer. By 'filling' the profile like this, the boundary layer becomes less prone to separation. However, tangential blowing is not useful for laminar flow control, because the flow created by the blown air is very likely to cause transition [29].

Slot Suction

Slot suction works by removing a part of the boundary layer through discretely spaced slots normal to the airfoil surface, illustrated by Fig. 2.10. By sucking away part of the boundary layer, the boundary layer thickness behind the slot is reduced, which allows it to withstand a higher adverse pressure gradient [50]. In front of the slot, the flow is accelerated into it, which creates a more favorable pressure gradient. These two effects

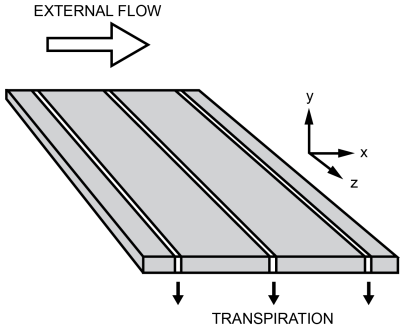

Figure 2.10: Schematic of slot suction indicating tangential flow over suction surface along with transpiration through slots in the surface

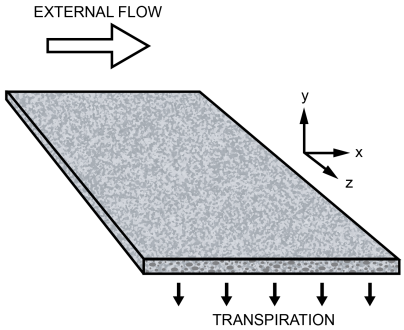

(a) Continuous suction through porous surface

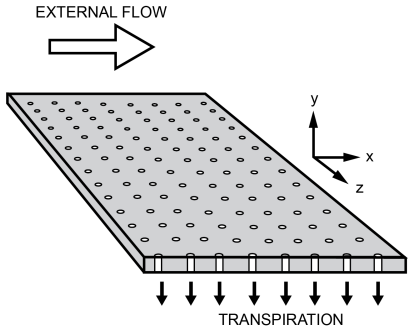

(b) Continuous suction through perforated sheet

Figure 2.11: Schematic of continuous suction through porous and perforated surfaces. External flow is tangential to the surface

increase the extent of laminar flow. However, the flow decelerates behind the slot. For this reason, the boundary layer behind the slot quickly becomes less stable, as if there were no positive influence of suction [45].

Because of this, the goal has been to “approach area suction more closely” [45, p. 3-4]. Perforated LFC surfaces did not seem feasible at the time (1950s), which is why researchers opted for closely spaced, narrow slots [45]. This shows that continuous suction through perforated sheets was desired, but manufacturing limitations prevented the development of these solutions. Currently, manufacturing of LFC surfaces is no longer a concern (Sec. 2.10.1). In addition, this illustrates that compensating for the drawbacks of discrete slots leads to more closely spaced slots with increasingly small suction velocity. In the limit, it can be expected that this tendency go towards continuous suction, which could be seen as the idealized case of discrete suction.

Suction through slots or slits is less effective on a swept wing, especially near the leading edge [26]. Here, the streamlines are highly curved, making it difficult to align the slots such that they are always perpendicular to the streamline direction. A further limitation is that high suction velocities through slots cannot be handled by the classical stability theory [14], because the assumption of small normal velocity in the derivation of the boundary layer equations is violated for slot suction. Continuous suction avoids these limitations.

Continuous Suction through Porous Surface

Porous surfaces for continuous suction, illustrated in Fig. 2.11a, can be made of a woven material, a fibrous material, or sintered metal [26]. The open passages through the material do not pass straight through. This makes porous materials susceptible to clogging and reverse blowing does not always clean them [26]. The biggest limitation of porous surfaces is their structural strength, which is typically low [14]. Furthermore, sintered materials can be heavy [14]. A further limitation of porous materials is less control over the porosity. With perforated sheets, the porosity can be directly controlled by the distribution and size of the holes. On the other hand, the porosity of a porous material is not necessarily uniform and may change if the surface is smoothed [14]. Surface smoothing may be required to prevent transition due to roughness [26].

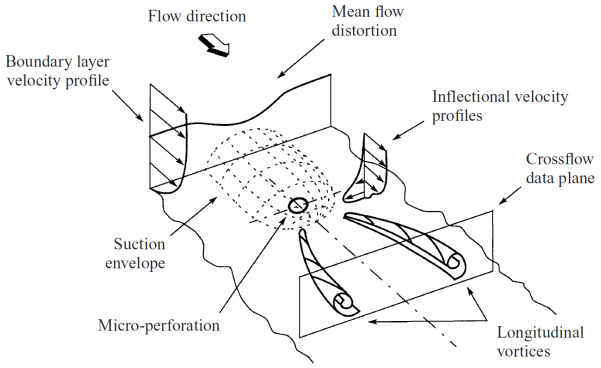

Figure 2.12: Flow field induced by a single suction hole [37]

Continuous Suction through Perforated Sheet

Perforated suction sheets clog less easily than porous surfaces, because their holes are larger and pass straight through the material, as indicated in Fig. 2.11b. Yet, clogging remains an issue for perforated sheets. Another issue for continuous suction surfaces, both porous and perforated, is the interface with the other, nonporous, surfaces of the wing. These joints can cause premature transition [14]. Contrary to porous materials, perforated sheets can be used as a structural element [49]. This is also an advantage over discrete suction, where the suction sheet is broken up into smaller segments that have lower rigidity than a single sheet. Finally, perforated sheets are advantageous over porous materials in off-design conditions [19].

The most important drawback of perforated surfaces is the flow induced by a suction hole. While suction through holes is typically modeled as continuous suction, the flow behavior is "profoundly different" from the idealized situation [37, p. 47]. In fact, the flow field around a suction hole is highly three-dimensional [37], featuring vortices behind the hole, as illustrated in Fig. 2.12. These vortices are always generated when suction is applied [36], but their structure and stability depends on the hole spacing and suction rate.

When the holes are far apart, combined with a low suction rate, streamwise vortices are formed behind the suction holes [45], which are contra-rotating [36]. At a combination of dense hole spacing and a larger suction rate, streamwise vortices from adjacent holes link up to form horseshoe vortices [49], which shed periodically. For even higher suction rates and denser hole spacing, the vortices between holes connect to form standing vortex bridges [45]. While suction through holes always creates downstream vortices, they are only detrimental if they grow and cause transition. This corresponds to the 'critical' suction rate [45], while even stronger suction rates correspond to 'oversuction' [49]. Premature transition due to oversuction can be avoided with a very large number of closely spaced, small holes [45]. Still, these holes will create vortices. Because they are contra-rotating, there is always a vortex that rotates in the same direction as the co-rotating CF vortices. As such, it may be expected that for some favorable combination of CF and hole spacing, these vortices can superimpose and cause transition earlier than without this interaction [26, 36]. This is why the critical suction limit is important for swept wings.

2.6.3. Hybrid Laminar Flow Control Concepts

For practical implementation of HLFC solutions, considering the complexity of the solution gives preference to passive systems, since they have no power consumption and would require less maintenance than active systems. However, active flow control is required to deal with cross flow instabilities on a swept wing. In this case, a 'semi-active' system would be preferred over a fully active system, to avoid the complexity of a time-varying response. Furthermore, for implementation of HLFC in the near future, concepts that have been flight-tested are better candidates than those tested only at a numerical or laboratory level.

From the point of view of complexity and technology readiness, plasma actuators and local wall heating can be excluded. In addition, compliant coatings may be excluded because of their limited applicability to air flows, while wall cooling may be excluded because of its limited benefits in air and the lack of a heat sink on typical transport aircraft. This leaves boundary layer transpiration, specifically, suction, as the most feasible solution for implementing HLFC on a transonic transport aircraft in the near future. Its effectiveness

has been proven in numerous experiments and flight tests. Boundary layer suction should be combined with tailoring of the airfoil pressure distribution to limit the suction requirements.

Finally, this leaves the selection between discrete and continuous suction. Addressing the limitations of discrete suction tends to continuous suction in the limit. Thus, it may be more useful to start with continuous suction from the outset. Continuous suction through perforated sheets appears to be the desired solution, because porous materials are more sensitive to clogging and have worse structural strength. Clogging remains an important issue for perforated materials, though. Other limitations include the critical suction limit and the possible interaction of hole vortices and CF vortices. Careful design can limit the negative effects of suction through perforated sheets, which makes it the most feasible way to implement boundary layer suction.

2.7. Suitable Aircraft Components for the Application of HLFC

According to Joslin, potential candidates for HLFC are the main wing, the horizontal and vertical tail surfaces, the nacelles of the engines, and the nose of the fuselage [31]. Common for these components is a comparable order of magnitude of the length scale, and thus the Reynolds number. Laminarization on the fuselage is prohibited by its large Reynolds number and the presence of surface irregularities, such as doors and windows.

The main wing is the prime candidate for friction drag reduction, because it has the largest surface area. The potential for drag reduction due to laminarization on the upper wing surface is approximately twice that of the lower surface [59]. This is because the upper surface experiences the highest flow velocities, which causes stronger velocity gradients in the boundary layer, and thus a larger wall shear stress, or skin friction [13]. Using this knowledge, applying HLFC only on the upper surface has the benefit that the allowable surface roughness on the lower surface may be relaxed [13]. This allows the placement of components, such as high lift devices, maintenance access panels, and engine pylons.

The potential for drag reduction on the tail surfaces is lower than on the main wing, due to their smaller surface area. However, installation of HLFC is simplified, because the tail surfaces do not have high lift systems and sometimes do not have an anti-icing system [51]. Because the tail surfaces are smaller than the main wing, a further benefit of HLFC on the tail surfaces is that large-scale models can be tested in wind tunnels [48]. This allows flight Reynolds number to be more easily obtained in wind tunnel experiments than for the main wing. However, a challenge with the tail surfaces is that they are prone to the CF instability. This is due to sweep angles commonly comparable or slightly greater than the sweep angle of the main wing [43].

Of the proposed aircraft components for HLFC, the nacelles usually have the smallest surface area. This implies that the nacelles have the smallest potential drag benefits from laminarization with HLFC. However, there is an important advantage for HLFC on nacelles: the engine can be used to generate the required suction power. Some bleed air can be extracted from the engine and be used to drive the suction system [41].

2.8. Practical Applications of Suction-Type HLFC

Boundary layer suction was identified in Sec. 2.6 as the most viable solution for implementing HLFC in the near future. The most suitable aircraft components to apply HLFC to were discussed in Sec. 2.7. Successful practical examples of boundary layer suction as a form of HLFC are presented in this section.

2.8.1. Leading Edge Flight Test Program

The Leading Edge Flight Test (LEFT) program was performed to test the practical integration and operation of an HLFC system. The program is described in [11]. Two different HLFC gloves were designed for the main wing of a JetStar aircraft. They incorporated all required subsystems, such as the suction system, an anti-icing system, an insect protection system, and a high lift system. One wing glove was designed with suction slots, while the other featured suction through a perforated sheet. The former consisted of a titanium surface with suction applied to both the upper and lower surfaces, as illustrated in Fig. 2.13a. A fluid that lowers the freezing point was injected through the slots as a combined solution for anti-icing and preventing insect contamination. In contrast, the latter applied suction only to the upper surface of the glove, as shown in Fig. 2.13b. A leading edge device of the Krueger type was installed, which acted as a high lift device and an insect shield. The titanium suction surface was perforated through electron-beam technology.

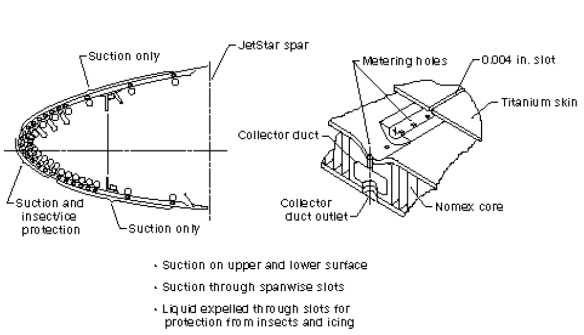

(a) HLFC using slot suction on upper and lower surfaces

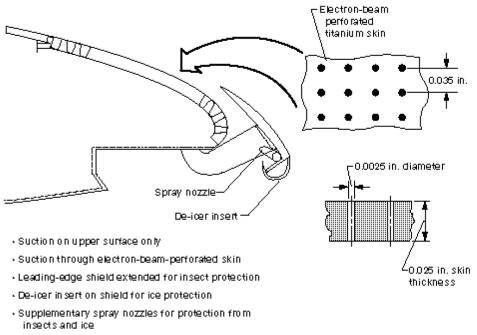

(b) HLFC using suction on upper surface through perforated sheet

Figure 2.13: Schematics of two HLFC solutions from LEFT program [11]

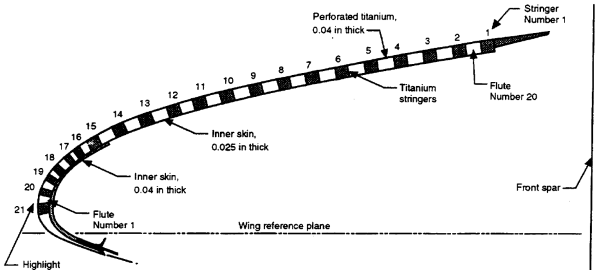

Figure 2.14: Schematic of suction panel used on Boeing 757 [7]

Both wing gloves were tested for four years in various weather conditions. No degradation of the titanium surfaces was observed. Slot suction performed worse than suction through the perforated surface. These tests demonstrated the successful operation of HLFC along with the integration of all its necessary components.

2.8.2. Boeing 757 HLFC

Boeing tested HLFC on one of its 757 aircraft. The test program is described in [11]. The HLFC solution was similar to the LEFT program: it also used a perforated titanium surface and a Krueger flap for high lift and insect protection. However, the anti-icing system was different, in that the Boeing 757 used a thermal anti-icing system, which injects hot air through the suction holes. The titanium skin was laser-drilled [6].

More information about the design of the HLFC system on the Boeing 757 is provided in [6]. An important point was that the suction sheet may be blocked at certain locations due to stringers or ribs. The suction rate thus has to be slightly higher in the remaining open areas to compensate for the area blocked by structural elements. Furthermore, a method of adjustment may be required to account for the movement of the attachment line with changing flight conditions [6]. The suction distribution contained high suction near the leading edge to suppress CF instabilities, but required much lower suction downstream where the dominant TS waves were partly suppressed by the favorable airfoil shape. The suction distribution was created by supplying varying pressures to small compartments under the skin, called flutes, as shown in Fig. 2.14. These flutes were short in the chordwise direction, but long in the spanwise direction. A constant spanwise suction distribution was obtained by aligning the flutes with isobars or by varying the skin porosity.

The flight tests demonstrated the applicability of HLFC in transonic flight conditions at higher Reynolds numbers than the LEFT program. Less suction power was needed than expected, partly due to neglecting streamline curvature terms in the stability theory [6]. These are typically stabilizing and would have reduced the suction requirements. Another important result was that the Krueger flap worked well as an insect shield.

2.8.3. Airbus A320 Hybrid Laminar Fin

One of the key European research activities regarding laminar flow is the application of HLFC to the vertical stabilizer of an Airbus A320 [28]. Flight tests proved the feasibility of HLFC for transport aircraft [28]. HLFC

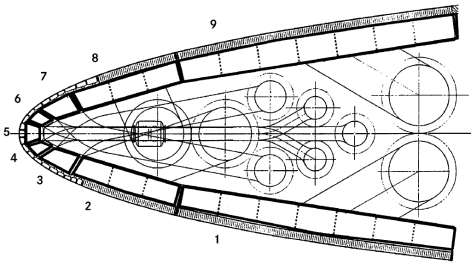

Figure 2.15: Suction system layout on the vertical tail of an Airbus A320, consisting of nine suction chambers [52]

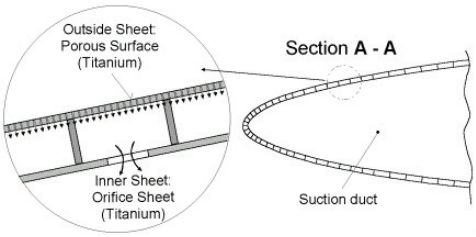

Figure 2.16: Simplified HLFC system with a single suction chamber [53]. Orifices in the inner panel control the suction distribution

was applied on the vertical tail for the reasons outlined in Sec. 2.7: there were no anti-icing and high lift systems [51], and flight Reynolds numbers could be reached on a scale-model in the wind tunnel [48].

Suction through a laser-drilled titanium sheet was applied to both sides of the symmetrical vertical stabilizer, as illustrated by Fig. 2.15 [53]. Nine internal suction chambers were placed symmetrically around the leading edge [52]. The suction panel extended to approximately 20% of the chord [52]. A Gaster bump was installed to prevent ALT [51]. Without suction, the CF instability would cause transition within the first 2% of the chord, but transition could be delayed to 20%–50% of the chord with suction, depending on the sideslip angle and Mach number [51, 52]. This illustrates that the CF instabilities were sufficiently suppressed on the suction panel. TS waves dominated behind the suction panel and caused downstream transition [52].

While the flight tests proved the feasibility of HLFC on a transonic transport aircraft, the HLFC setup was not economically viable. Intended to test the capabilities of HLFC, the suction system on the A320 was complex and ultimately too heavy to benefit from the drag reduction due to extended laminar flow [53]. In addition, practical concerns such as anti-icing and insect contamination were not addressed [53].

Therefore, follow-up research focused on making the suction system simpler and lighter. A proposed solution was to use the entire leading edge region as a single suction chamber [53], a significant simplification over the original configuration. Suction must now be generated with a single internal pressure level, so the skin was split into two parts to still enable control over the suction distribution, as indicated in Fig. 2.16. The outer skin remains a perforated sheet, but an additional inner orifice panel attached to the stringers divides the leading edge region into small compartments. The orifices are sized such that the pressure level in each compartment creates the intended suction distribution. The downside of this system is that the fixed orifice size must account for all flight conditions. However, significant weight savings can be obtained from such a system. The simplified system was successfully applied to an A320's vertical and horizontal tail surfaces [53].

Further simplification and weight reduction of an HLFC system can be obtained with a passive suction system, removing the need for a pump [54]. With a convenient location for the suction system outlet, the pressure difference between the inlet and outlet could generate a natural suction flow. A numerical investigation by Krause et al. showed that placing the air outlet on the lower part of the vertical tail appears the most promising for generating the required suction mass flow while limiting the associated aerodynamic drag [32].

2.8.4. Boeing 787 Passive HLFC

In 2011, it was reported that HLFC was going to be used on the Boeing 787-9 [65]. It would be used on both the horizontal and vertical tail surfaces. An intriguing feature is that the system would be passive [65]. Unfortunately, not much public information about Boeing's HLFC efforts on the 787 is available, but an online article[1] states that the 787-9 aircraft are currently flying using HLFC technology. According to Fig. 2.17, small doors are used to drive the suction. Interestingly, these doors are placed near the root of both the vertical and horizontal tail surfaces, at a similar location as Krause et al. suggested in [32], supporting their observations.

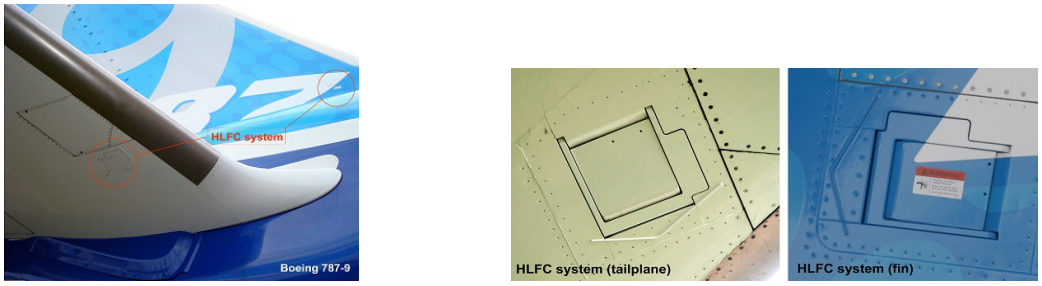

(a) Location of HLFC systems on the tail surfaces

(b) Doors that are part of the HLFC system

Figure 2.17: Images[1] of the HLFC systems on the tail surfaces of the Boeing 787-9

Furthermore, the article suggests that the doors open both ways. One direction would be used to allow the air to be naturally sucked through the suction panels and exhausted via the doors. The other direction may be used to capture air into the system and blow it out through the suction sheet. It is suspected that this blowing may be used at low altitudes to prevent dust from entering the suction system. In addition, if this flow can be heated, it may also be a solution for anti-icing through transpiration heating. Because thermal anti-icing was also used on the Boeing 757 (Sec. 2.8.2), it is possible that it is used again on the 787.

While not much is known about the HLFC setup on the Boeing 787, it represents an important milestone of HLFC: its first implementation on a commercially operated aircraft. This is a big step forward from the Boeing 757 and Airbus A320 flight tests. Those tests were primarily used to demonstrate the practical operation of HLFC, but the systems were too complex and heavy to yield a net performance benefit. From the available information, it appears the performance gain is reached with the passive HLFC system on the Boeing 787-9.

2.9. Research on Boundary Layer Suction at TU Delft

Besides the practical examples of HLFC, as presented in Sec. 2.8, research on boundary layer suction has been performed at TU Delft. The relevant results for HLFC are discussed in this section.

Extensive research on sailplane aerodynamics has been conducted by Boermans, as documented in [8]. Boundary layer suction was investigated in an effort to improve the performance of sailplanes. Like for the Airbus A320, Boermans designed a simplified suction system. Illustrated in Fig. 2.18, it consists of an outer perforated sheet and an internal space filled by a foldcore structure [8]. The goal of the foldcore structure is to create the desired suction distribution through the outer skin. Because the external pressure varies over the wing, the internal pressure below the suction sheet should also vary. This is controlled by appropriately sized holes in the foldcore structure, acting as throttling holes. These holes are much larger than the holes in the outer skin. The source of the suction air is a single row of large holes in the very front of the foldcore structure. A comparison with the simplified HLFC system on the A320 (Fig. 2.16) shows that both solutions are a way of creating a variable suction distribution while having only one internal pressure level. While it does make suction systems simpler, a single pressure level means that the suction distribution can only be optimized for one condition [8], as was also mentioned for the A320.

Steffens investigated the pressure loss across perforated sheets and their critical suction limit in [67]. An experimental study was performed to characterize the pressure drop across two different suction sheet ge-

[1] `https://www.flightglobal.com/news/articles/farnborough-aero-secrets-of-boeings-new-dreamliner-401784/` Accessed July 27, 2017.

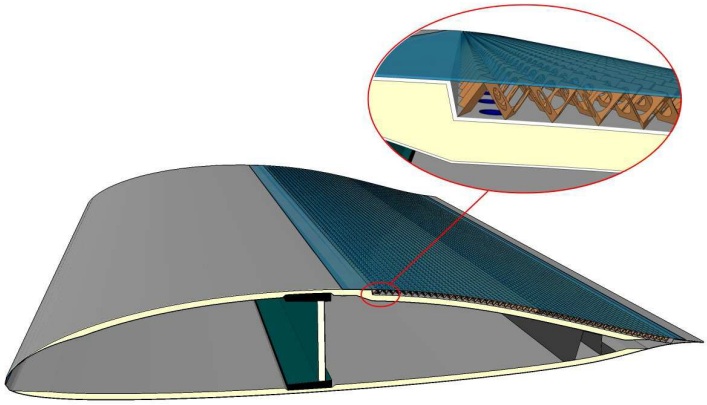

Figure 2.18: Suction system containing a perforated outer skin and an internal foldcore structure containing orifices to generate the desired suction distribution from a single source [8]

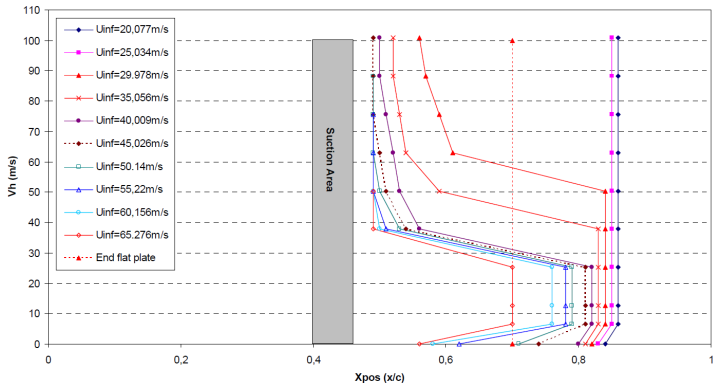

Figure 2.19: Experimental data for quantifying the critical suction limit with multiple rows of holes [67]. Chordwise transition location is shown against hole suction velocity for a range of freestream velocities

ometries. Extrapolation of these results to arbitrary geometries is limited by the number of samples tested in this study. An important point from this study is that the pressure drop across a suction sheet can be split up into two parts [67]. The first part of the pressure loss is due to the perpendicular suction flow through small perforations, while the second part originates from the tangential boundary layer flow over a suction sheet.

The latter pressure losses were experimentally investigated in [67]. The results were compared to a model, but an imperfect agreement was found, likely due to applying a model intended for turbulent boundary layer shock wave interaction to an LFC situation. Therefore, Steffens concluded that more measurements would be required in order to predict this pressure loss for arbitrary geometries. The results from [67] highlight a gap in knowledge regarding the prediction of the pressure loss across suction surfaces. This suggests additional experiments on pressure losses of perforated sheets over a wide range of geometric and flow parameters. In fact, Chap. 5 deals with this goal in more detail.

The experimental study performed in [67] showed that the critical suction limit for a suction sheet with multiple holes is much lower than suggested by criteria for single (rows of) suction holes [67]. Pfenninger also indicated this point but did not quantify it [45]. Hence, the work from [67] is relevant for obtaining quantified data about this topic. The results are shown in Fig. 2.19, indicating how the transition location first moves aft with an increasing suction rate up to a certain point, as expected, but the transition location suddenly moves forward with even higher suction rates, indicating that the critical suction limit has been exceeded.

Experimental research on slot suction of a turbulent boundary layer was performed in [73]. The results on a turbulent boundary layer do not directly apply to laminar flow control, but some observations are still relevant. For instance, the flow field induced by the suction slot showed a region of strong deceleration be-

hind the slot [73]. As discussed in Sec. 2.6.2, this could lead to premature transition in case of a laminar boundary layer. Furthermore, a comparison of slot suction to continuous suction showed that the effectiveness of suction does not depend on the suction surface [73]. However, this only holds as long as the strong local effects of slot suction do not induce premature transition. An additional advantage for continuous suction is that it provides easier control over the three-dimensional suction distribution than for slot suction [73].

Boundary layer suction was implemented into XFOIL and MSES modeled through integral formulations in [72]. However, the present research must use a different implementation, because the boundary layer equations in Sec. 3.4.1 are discretized with a finite difference scheme. Still, one of the validation cases can also be used to validate the numerical implementation of boundary layer transpiration in the present work.

Boundary layer suction near the trailing edge to control separation or wake bursting on a multi-element airfoil was studied in [71], which focused on minimizing the suction pump requirements by applying the suction at a convenient location, which is relevant for HLFC. Instead of focusing only on aerodynamic benefits, it should be balanced with the required suction power [71]. The suction power may be reduced by selecting appropriate locations for the inlet and outlet of the suction system. In order to avoid a pump altogether and create a passive system, the total pressure at the outlet should be lower than at its inlet, with a margin to account for the pressure losses over the suction sheet and all internal ducting. This reasoning was used in [71] to apply suction near the trailing edge. Here the static pressure is relatively high, which means that the pump requires less power to pump the air back to freestream pressure at the outlet. Applying this reasoning to HLFC implies that suction be avoided at the suction peak on the upper surface. However, this is typically the region near the leading edge where suction is required to suppress CF instabilities.

Still, passive HLFC was presumably obtained on the Boeing 787-9 (Sec. 2.8.4) on a surface highly affected by cross flow. Suction to control CF instabilities is most needed in the region of strongest pressure gradient (Sec. 2.3.2). If the pressure distribution contains an initially strong pressure gradient followed by a much more gradual decrease in pressure (Fig. 5.3), the point of lowest pressure is further downstream of where suction is most needed. Therefore, if the outlet of the suction system is placed at that location and if the extent of suction remains limited to the leading edge region, it may be possible to obtain naturally driven suction. A solution like this may be used on the Boeing 787-9, because the outlet panel appears to be located downstream of the suction surface.

Extensive research on predicting boundary layer transition with and without suction has been performed by van Ingen. In fact, the e^N-method was originally proposed by van Ingen in [74], while at the same time Smith and Gamberoni independently presented the same method in [63]. Since its development, van Ingen demonstrated that the e^N-method could also be used with boundary layer suction [75].

Further research from van Ingen has focused on using database methods for transition prediction with the e^N-method [76]. This is because solving the Orr-Sommerfeld equation (Sec. 3.3.2) over the entire chord of an airfoil is expensive. Rather, the database method uses a set of predetermined stability results of Falkner-Skan flows to predict the critical Reynolds number and thereby the transition location [76]. The shape factor of the boundary layer velocity profile is used to correlate the critical Reynolds number. The correlation works with pressure gradient and suction [76], which can be considered to be interchangeable effects [75]. This was first argued in [75], where van Ingen found that the resulting stability behavior was similar if an amount of suction was applied to a flat plate boundary layer such that its critical Reynolds number was the same as another boundary layer flow without suction. In later research, this claim was supported by the observation that, given the same shape factor, boundary layer profiles created with suction produce nearly the same velocity profile and curvature as a corresponding Falkner-Skan profile [76].

2.10. Challenges for HLFC Technology

Sections 2.8 and 2.9 highlighted some difficulties inherent to HLFC design. This section summarizes the main challenges that have to be overcome before HLFC technology can be implemented in practice.

2.10.1. Manufacturing

Historically, surface roughness and waviness have hindered the development and implementation of hybrid laminar flow control [14, 31]. However, as of the 1990s, manufacturing capabilities have advanced such that the required smoothness can be satisfied [31]. Still, care must be taken with respect to surface irregularities, such as high lift devices, maintenance access panels, and other attachments. Because the lower surface of the main wing usually contains these, HLFC is typically reserved for the upper surface, as indicated in Sec. 2.7.

Traditional manufacturing techniques for creating perforated metal sheets include punching, drilling, etching, and rolling wire mesh cloths [19]. Their minimum obtainable hole diameter is limited or these methods are time-consuming. Modern methods are electron-beam drilling and laser drilling [31]. In fact, the suction sheet of the LEFT program was created by electron-beam drilling (Sec. 2.8.1). The Boeing 757 (Sec. 2.8.2) and Airbus A320 (Sec. 2.8.3) HLFC programs, which came after the LEFT program, used suction sheets made by laser drilling. These drilling techniques have been proven successful in flight tests.

All HLFC programs reported in Sec. 2.8 had suction sheets made from titanium, which is no coincidence. A study of the durability of perforated panels, made from titanium, aluminum, and a carbon fiber composite, during 20 months of flight, showed that titanium panels had no degradation [80]. In contrast, aluminum panels were significantly less durable, displaying micro-cracks [80]. The carbon fiber composite degraded very quickly, showing surface erosion after only two months of testing [80]. With the LEFT program, the titanium suction sheet also showed no degradation (Sec. 2.8.1). Titanium is therefore considered as the benchmark material for HLFC applications [80].

2.10.2. Insect Contamination

Maintaining a smooth surface requires the prevention of accumulating foreign objects, such as insects, onto the surface. Insect density is highest near the ground, so that a solution for preventing insect contamination must be used at low altitudes [31]. During cruise at high altitude, such a system is not necessary. Several solutions have been proposed, such as mechanical scrapers, deflectors, paper covers that are removed once cruise altitude is reached, and continuous liquid discharge [31]. A mechanical scraper does not seem practical because of system complexity and maintenance requirements. Paper covers may be used during take-off, but they cannot be put back in place for landing. This implies that the surface must be cleaned after each flight, which is not desirable from an operational point of view. Another idea was to use superslick or hydrophobic surfaces intended to prevent insects from sticking to the surface. However, experiments showed that these materials did not prevent insect contamination to such a degree that premature transition could be avoided [11]. Thus, it became clear that an active system would be required.

Liquid discharge is an active solution for preventing contamination. Insect accumulation can be prevented by keeping the leading edge wet. Such a system was successfully used during the LEFT program, serving the combined purpose of anti-icing (Sec. 2.8.1). However, the liquid cannot wash insects away that had already stuck to the surface when it was dry [11]. In addition, a system that uses liquids will be heavy, so Schrauf calls for the development of a self-cleaning coating [53]. Ideally, this coating would prevent insect contamination and provide anti-icing capabilities. However, it is unclear whether such a material has since been developed. A deflector acting as a shield to prevent insect accumulation on the main wing has been used effectively in the form of a Krueger flap during the LEFT program (Sec. 2.8.1) and the Boeing 757 HLFC program (Sec. 2.8.2). The downside of a Krueger flap is that it creates surface discontinuities when retracted into the lower surface, which can prevent laminar flow. Because of this, a Krueger flap is not a good solution when laminar flow control is desired on both sides of the wing, for example for the vertical stabilizer.

2.10.3. Weather Effects

Not only insects but also atmospheric conditions, such as rain, ice, and gusts, can affect laminar flow. During flight tests of laminar flow control on an F-94A aircraft, loss of laminar flow was observed during strong gusts [47]. However, as soon as the gust passed, laminar flow was obtained again without any hysteresis [47]. For the same flight tests, rain caused transition, but laminar flow was regained soon after clearing the rain. In a study of atmospheric effects, it was found that cloud encounters are not frequent enough to cause a significant loss of performance from loss of laminar flow, even when it was assumed that all cloud encounters cause a complete loss of laminar flow and that clouds would not be actively avoided during flight [11]. This implies that the benefits of HLFC remain when real-world weather effects are taken into account.

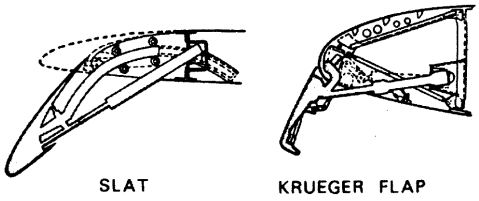

Figure 2.20: Comparison between slat and Krueger flap as leading edge high lift devices [69]

Another atmospheric effect is ice formation. An anti-icing and de-icing system will be required to avoid losing laminar flow due to accumulating ice. Several solutions were identified in Sec. 2.8. For the LEFT program, a fluid was injected that lowers the freezing point. The Boeing 757 used thermal anti-icing. These solutions worked in practice and demonstrate that "[the] icing issue for NLF and LFC is more of a system design problem than a technical obstacle" [31, p. 14]. The Airbus A320 did not have an anti-icing system, but the importance of anti-icing for industrial application was stressed before and after the flight tests [28, 48, 53].

Thus, finding an efficient anti-icing system that is not too heavy is a remaining challenge. While a liquid system may be heavy [53], its weight penalty could become acceptable if it can also prevent insect contamination, as demonstrated in the LEFT program. On the other hand, Boeing has had success with thermal anti-icing on the Boeing 757. The program showed that thermal anti-icing through transpiration heating may be more efficient than a conventional anti-icing system, because the hot air injected through the suction holes comes into direct contact with the ice, such that almost all heat can be used to melt it [6]. The weight penalty of a thermal anti-icing system is limited, because the required ducting is already part of the suction system. A heat source will be required, though, for which the Boeing 757 used bleed air from the engine [6].

2.10.4. Leading Edge High Lift Device

The main wing of a transport aircraft needs a leading edge high lift device in order to increase the stall angle of attack, thereby increasing the maximum lift coefficient, which is required for take-off and landing. The leading edge device must be compatible with the HLFC system. Aircraft without HLFC usually have a slat as a leading edge device [65]. For aircraft with HLFC, a slat is not an option because the slat is stored in front of the main wing, as illustrated in Fig. 2.20, creating a surface discontinuity near the leading edge, where the thin boundary layer is susceptible to roughness. Furthermore, the slat is always the most upstream component on the wing, which means it will be most affected by insect contamination. Preventing this would require a system that is small enough to be installed in the slat, which seems impractical at the moment.

Surface discontinuities created by a slat can be avoided by means of a morphing leading edge. Its principal advantage is the seamless integration with the main wing [64]. However, its biggest disadvantage is that the flexible surface must be combined with perforations for HLFC, leading to a variable suction distribution if holes and distances between holes can be stretched. In addition, the morphing mechanisms must be combined with all other subsystems required for HLFC, and insect contamination must be addressed.

Given the disadvantages of slats and morphing leading edges, the preferred solution for HLFC is a Krueger flap [65]. While its high lift performance is worse than a slat [48], a Krueger flap has an important benefit: the flap can be used as a deflector-type insect shield. Because it deploys in front of the main wing, as shown in Fig. 2.13b, it collects all insect contamination, but keeps the leading edge of the main wing clean. During cruise, the flap is stored, leaving a perfectly clean surface on the main wing without surface discontinuities.

3

Numerical Modeling of Boundary Layer Transpiration and Its Effect on Transition

The concept and benefits of HLFC were introduced in Chap. 2, with boundary layer suction emerging as the most feasible solution for HLFC on a transonic transport aircraft. Following the research objective, developing the capability to design a suction-type HLFC component requires a tool that quantifies the effect of suction on boundary layer development—and ultimately, transition. To that end, this chapter explores the necessary steps to design such a tool. First, methods to model boundary layer stability are presented in Sec. 3.1, which are required for some of the transition prediction methods identified in Sec. 3.2. Subsequently, Sec. 3.3 describes the theoretical background for predicting transition for a boundary layer affected by suction, which includes the boundary layer equations and the stability of such a boundary layer.

Afterwards, these steps are implemented in a transition prediction tool. This tool is already available at TU Delft, as described in Sec. 3.4. However, some modifications are required before it can be used to design an HLFC component, as outlined in Sec. 3.5.

3.1. Methods for Modeling Boundary Layer Stability

Prior to predicting boundary layer transition, the stability of a boundary layer should be evaluated, which can be done with several methods. Some of them are discussed in the present section.

3.1.1. Linear Stability Theory

Linear stability theory determines the growth rate of wave-like disturbances. In linear stability theory, a sinusoidal disturbance of a certain frequency is superimposed onto the steady base flow. Subsequently, the theory determines its amplitude growth as the wave propagates in the boundary layer [35]. Using the amplitude growth from linear stability theory as input, the transition location may be estimated with the e^N-method, which is discussed in Sec. 3.2.2.

Within linear stability theory, a selection between a temporal or a spatial formulation must be made. The former describes the development of a disturbance wave in time and the latter in space. The temporal theory is generally simpler than the spatial theory. For a steady base flow, the disturbance amplitude does not change in time, but only in space [35]. Therefore, the spatial theory describes the amplitude growth more directly. In fact, Saric claimed already in 1992 that there is no reason to use the temporal theory "[with] today's advanced computers" [49, p. 4-7]. Thus, the spatial theory is preferred over the temporal theory.

A convenient feature of linear stability theory is observed in combination with suction. It is generally accepted that the effects of the stability modifiers, such as pressure gradient, suction, and heat transfer, affect boundary layer transition in the same way as linear stability theory predicts [35]. Thus, if linear stability theory predicts suction to stabilize the flow, it should also be stabilized in the real flow. Hence, linear stability theory can be used to design HLFC systems to a first degree.

3.1.2. Parabolized Stability Equation Theory

One of the shortcomings of linear stability theory is that it cannot account for nonlinear effects. This issue can be addressed with the parabolized stability equation (PSE) theory. Within this framework, it is possible to include some nonlinear effects, in addition to the influence of surface curvature and boundary layer history [31]. Hence, a more complete description of the disturbances is used to compute the amplitude growth of unstable waves. This information is subsequently used with the e^N-method, presented in Sec. 3.2.2, to predict the location of boundary layer transition.

A necessary input for the PSE method is a good estimate of the initial disturbance environment [31]. However, this is not straightforward, because receptivity is not yet fully understood. Alternatively, linear stability theory may be used to obtain first order information on the initial disturbances [31].

3.2. Methods for Predicting Boundary Layer Transition

Several methods exist for predicting boundary layer transition. Each method has its own strengths and weaknesses. Some methods are documented and reviewed in the present section.

3.2.1. Criterion-Based and Database Methods

The least computationally expensive methods for transition prediction are based on empirical criteria or make use of a database to estimate the onset of transition. Although these methods are attractive due to their simplicity, they have limited accuracy in estimating boundary layer transition for arbitrary flows.

Regarding criterion-based methods, for two-dimensional transition dominated by the TS instability, a criterion based on a Reynolds number using the momentum thickness, as in Eq. (3.1), has been used [3]. Alternatively, for transition dominated by the CF instability, a criterion based on a cross flow Reynolds number, as in Eq. (3.2) or (3.3), has been used [3].

$$Re_\theta = \frac{U_e \theta}{\nu} \tag{3.1}$$

$$Re_{\delta_2} = \frac{1}{\nu} \int_0^{\delta_{99}} w_s \, dy \tag{3.2}$$

$$Re_{CF} = \frac{|\max w_s| \delta_{99}}{\nu} \tag{3.3}$$

Database methods rely on the known stability properties of self-similar boundary layer solutions [3]. By using this database of information, interpolation between these results can provide an estimate of the stability of comparable flows [3].

3.2.2. e^N-Method

The e^N-method is an envelope method that uses growth rates of waves, obtained with linear stability theory or PSE theory, within a range of frequencies [2]. The envelope of the maximum amplification over the entire range of frequencies between two locations is represented by the N-factor. The N-factor is thus a measure of the amplification factor between two locations. If the start of amplification is chosen to be the critical location where the disturbances first start to grow, the N-factor is given by Eq. (3.4).

$$N = \ln \frac{A}{A_0} \tag{3.4}$$

The N-factor at transition, which is determined experimentally, is an important parameter for the success of the e^N-method. Because the N-factor only describes amplitude growth, but transition is initiated by a certain absolute disturbance amplitude [2], the initial disturbance environment must be similar in the calibration of the e^N-method and the cases to which it is intended to be applied [3, 49]. This is why Bushnell and Tuttle stress the importance of using low-disturbance validation data [14]. Flight tests would be the best source for validation data, because of the similar atmospheric disturbance conditions [14]. Wind tunnel data may be used with "some confidence" provided that the freestream turbulence and acoustic disturbances are low [14, p. 17]. Even then, wind tunnel data may still yield different N-factors [3], because atmospheric turbulence affects transition less than the freestream turbulence in wind tunnels [45]. So, having good-quality,

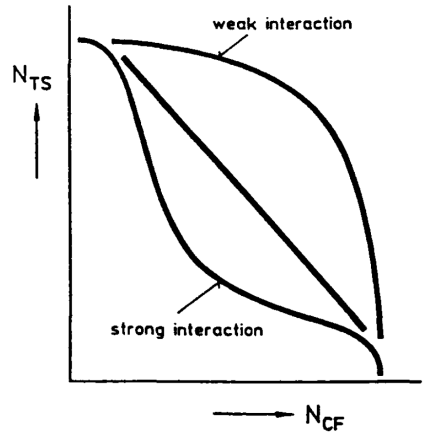

Figure 3.1: Transition N-factors for varying degrees of interaction between TS and CF instabilities [3]

low-disturbance validation data is paramount for the correct estimation of the N-factor at transition.

Furthermore, the N-factor may be different depending on the strategy in which the amplification rate is integrated. A first option is to integrate in the direction of maximum amplification, which is the envelope method [3]. Following this strategy, the effects of the TS and CF instabilities are added into a single N-factor. A second option is to consider separate N-factors for the TS and CF instabilities, N_{TS} and N_{CF}. Then, transition occurs for some combination of these two N-factors. Neither of these solutions take into account a possible interaction between TS and CF instabilities [3]. This interaction may be assessed by a graph such as Fig. 3.1. When comparing N-factors, it is important to ensure that the same integration strategy is used [3]. A limitation of the envelope method, which uses a single N-factor, occurs with the application of suction. For HLFC applications where CF is prevented by suction and transition occurs through TS instabilities, the value of N at transition may depend on the amount of suction [56]. For this reason, it may be preferred to split the contributions of the streamwise and CF instabilities and use two N-factors.

When two N-factors are used to predict transition, there is no reason why the streamwise and cross flow N-factors should have the same critical value. This is because the typical frequency range for these two types of disturbances are distinct [3]. Therefore, they will respond differently to external disturbances. In other words, their receptivity to the external disturbances is not the same.

A limitation of the e^N-method based on linear stability theory is that linear theory is used to predict a nonlinear phenomenon [22]. Once the nonlinear stage of disturbance amplification is reached, the nonlinear effects dominate and will cause transition, even if linear stability theory says that the disturbances should be decaying [35]. Therefore, the goal of laminar flow control is to prevent the growth of disturbances from reaching nonlinear effects which lead to the breakdown into turbulence [49]. Thus, for the design of laminar flow control, the actual N-factor should be kept below the critical N-factor with a certain margin, such that nonlinear effects do not set in over the controlled region.

This point is especially important for transition governed by the CF instability. Here, the nonlinear region is more extensive than for the TS instability [3]. Thus, it is imperative to maintain an N-factor significantly below the critical value for regions dominated by CF, as was used in [4].

Additional complexity arises for the application of the e^N-method, based on linear stability theory, with boundary layer suction. It is not clear whether the critical N-factor will remain the same with suction as without it [3]. This is illustrated by an experiment of suction through perforated strips on a flat plate, in which the results with suction did not agree well with the e^N-method based on linear stability theory, while good agreement was found without suction [21]. For cases with suction, the N-factor at transition varied between 0 and 8 [21]. These results indicate that experimental validation is required when estimating transition for HLFC applications with the e^N-method based on linear stability theory.

Two potential reasons were identified in [21] to explain the varying results of the e^N-method with suction. The first reason was that suction may have been less effective if nonlinear breakdown had been reached. As mentioned previously, once this stage is reached, transition will occur even if linear stability theory indicates that the disturbances should decay. An important note is that this behavior is not expected if N is monotonically increasing [21]. So, for HLFC applications, careful attention should be paid to results from the e^N-method based on linear stability theory if N is not monotonic. The second reason was that oversuction was predicted to have an influence [21]. Indeed, this is likely, because the suction rates were fairly high.

3.2.3. Other Methods for Predicting Transition

More recent and advanced transition prediction methods using large eddy simulation (LES) or direct numerical simulation (DNS) are reported in [33]. The advantages of these methods is that they are based on less restrictive assumptions, and as such their applicability is broader, especially for DNS. However, they require significant computational resources, which prevents the application for industrial transition prediction purposes in the preliminary design stage.

Other methods are also discussed in [33], such as low Reynolds number turbulence models, the intermittency transport method, and the laminar fluctuation energy method. But, as described in [33], they have limited applicability.

3.2.4. Trade-Off

In Secs. 3.2.1 through 3.2.3, transition prediction methods were presented, ranging from simple to advanced. While criterion-based methods and database methods are fast, they are not sufficiently reliable or detailed to predict transition for the design of HLFC technology. The e^N-method has its drawbacks, but is the most developed method. More advanced methods, such as LES or DNS are promising, but are too intensive to be used during the preliminary design stage of HLFC solutions. The advanced methods would be reserved for detail design stages, where computational effort is of less importance. For the same reason, the e^N-method is preferably used based on linear stability theory rather than PSE theory.

Despite its shortcomings, described in Sec. 3.2.2, the e^N-method is still the industry standard for transition prediction [3, 35, 49]. For example, the e^N-method based on linear stability theory was used to design the HLFC system on the Airbus A320 [52]. Furthermore, DLR uses the e^N-method based on linear stability theory for laminar wing design [59]. In conclusion, the e^N-method based on linear stability theory is currently the most suitable tool for the design of an HLFC component.

3.3. The e^N-Method for a Boundary Layer Including Transpiration

The e^N-method, using linear stability theory, was identified in Sec. 3.2 as the most suitable method for predicting transition. So, the present section focuses on how linear stability theory and the e^N-method can be used to assess the stability of a boundary layer with transpiration. First, a base flow solution is required, for which the boundary layer equations for an infinite swept wing including transpiration are used, as derived in Sec. 3.3.1. As the next step, Sec. 3.3.2 describes how the stability of such a boundary layer can be assessed.

3.3.1. Base Flow: Boundary Layer Equations

The concept of a boundary layer was introduced in Sec. 2.2. Here, it was determined that the boundary layer can be considered as a small perturbation of the inviscid flow solution when $Re \to \infty$. Following this concept, the boundary layer equations for high-Reynolds number flow can be derived from the complete set of equations of motion by taking the limit for the Reynolds number tending to infinity.

Reference Frame

The context of this research is a transport aircraft in the transonic flight regime. Thus, this research deals with a swept wing of large aspect ratio. Because of this large aspect ratio, assuming an infinite swept wing does not introduce much error, if the root and tip regions of the wing are excluded. In fact, Saric states that the influence of non-parallel effects is limited [49]. Thus, a parallel flow is obtained that is invariant in the spanwise direction. So, the boundary layer equations will be derived for an infinite swept wing.

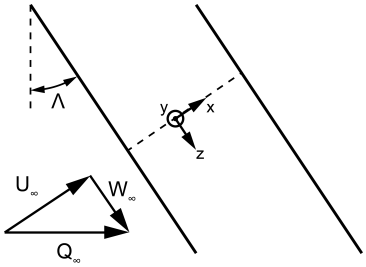

Figure 3.2: Reference frame on infinite swept wing

Figure 3.2 shows an infinite swept wing with sweep angle Λ, along with its Cartesian coordinate system. The x-direction is normal to the leading edge and is at an angle with respect to the streamwise direction; the y-direction is normal to the wall and points out of the image plane; the z-direction points in the outboard spanwise direction.

Because of this reference frame, the incoming flow, Q_∞, can be divided into two components: a streamwise and a spanwise component. The streamwise component aligns with the x-direction and is given by Eq. (3.5a). Similarly, the spanwise component aligns with the z-direction and is given by Eq. (3.5b).

$$U_\infty = Q_\infty \cos\Lambda \tag{3.5a}$$

$$W_\infty = Q_\infty \sin\Lambda \tag{3.5b}$$

Incompressible Boundary Layer Equations for Infinite Swept Wing

The incompressible boundary layer equations for an infinite swept wing including transpiration are derived in App. A. The equations are derived in nondimensional form, but are repeated here in dimensional form for clarity. The continuity and Navier-Stokes equations are given by Eqs. (3.6) and (3.7), respectively. Equation (3.8) presents the corresponding boundary conditions. Compressible flow is reserved for future work.

$$\frac{\partial u}{\partial x} + \frac{\partial v}{\partial y} = 0 \tag{3.6}$$

$$u\frac{\partial u}{\partial x} + v\frac{\partial u}{\partial y} = U_e\frac{dU_e}{dx} + \nu\frac{\partial^2 u}{\partial y^2} \tag{3.7a}$$

$$u\frac{\partial w}{\partial x} + v\frac{\partial w}{\partial y} = \nu\frac{\partial^2 w}{\partial y^2} \tag{3.7b}$$

$$\begin{aligned} y = 0: &\quad u = 0; \quad v = v_w(x); \quad w = 0 \\ y \to \infty: &\quad u = U_e; \quad w = W_e \end{aligned} \tag{3.8}$$

It can be seen that Eq. (3.7b) is decoupled from the others. Therefore, w can be solved for after solving for u and v. Furthermore, the system is parabolic, which means that it can be solved using a marching procedure in the x-direction.

Other important points mentioned in App. A is that the boundary layer equations are only valid for high-Reynolds number flows. Furthermore, the transpiration velocity should remain small. In fact, v must be of the order of the boundary layer thickness.

3.3.2. Linear Stability Theory

Linear stability theory describes the growth of disturbances in the base flow, which follows from the Orr-Sommerfeld equation. Subsequently, the local growth rate must be integrated to obtain an N-factor, for which multiple strategies exist. The present section discusses both of these steps.

Orr-Sommerfeld Equation

Linear stability theory is based on the introduction of three-dimensional disturbances into a boundary layer flow (Sec. 3.1.1). These disturbances are waves with a frequency ω that propagate in the direction of the wave number vector (k), which has a streamwise component (α) and a spanwise component (β) [35].

The Orr-Sommerfeld equation, as a basis of linear stability theory, is based on a simplified base flow boundary layer, onto which the disturbances are added, as shown in Eq. (3.9). The base flow is steady and is indicated with an overbar. The unsteady fluctuations are indicated with a prime. In addition, the notation of App. A is followed, where symbols with a superscript * are nondimensional quantities.

$$u = \bar{u} + u'; \quad v = v'; \quad w = \bar{w} + w'; \quad p = \bar{p} + p' \tag{3.9}$$

The present section briefly discusses the derivation of the Orr-Sommerfeld equation, but more details can be found in App. B. After superimposing the disturbances onto the base flow, the next step is to specify that the perturbed quantities of Eq. (3.9) still satisfy the continuity and Navier-Stokes equations. Substitution and subtracting the mean flow results in a system of equations that is linear in the disturbance quantities [35].

The linear disturbance equations contain mean flow coefficients that only depend on y because of the parallel-flow assumption. This implies the solutions are separable and a possible solution is Eq. (3.10) [35, 49]. The terms $\hat{u}^*$, $\hat{v}^*$, $\hat{w}^*$, and $\hat{p}^*$ describe the shape and amplitude of the modes in the boundary layer, while the exponential term describes that the disturbances are traveling waves in the xz-plane.

$$\begin{bmatrix} u'^* \\ v'^* \\ w'^* \\ p'^* \end{bmatrix} = \begin{bmatrix} \hat{u}^*\left(y^*\right) \\ \hat{v}^*\left(y^*\right) \\ \hat{w}^*\left(y^*\right) \\ \hat{p}^*\left(y^*\right) \end{bmatrix} e^{i\left(\alpha^* x^* + \beta^* z^* - \omega^* t^*\right)} \tag{3.10}$$

When the solutions of Eq. (3.10) are substituted into the linearized disturbance equations, a system of four equations results. These equations may be combined to form a single, fourth order equation for $\hat{v}^*$, given in Eq. (3.11) [35, 49]. Here ϕ is used to indicate $\hat{v}^*$.

$$\begin{aligned} \frac{d^4\phi}{dy^{*4}} - 2\left(\alpha^{*2} + \beta^{*2}\right)\frac{d^2\phi}{dy^{*2}} + \left(\alpha^{*2} + \beta^{*2}\right)^2\phi = \\ iRe_l\left(\left(\alpha^*\bar{u}^* + \beta^*\bar{w}^* - \omega^*\right)\left(\frac{d^2}{dy^{*2}} - \left(\alpha^{*2} + \beta^{*2}\right)\right) - \left(\alpha^*\frac{d^2\bar{u}^*}{dy^{*2}} + \beta^*\frac{d^2\bar{w}^*}{dy^{*2}}\right)\right)\phi \end{aligned} \tag{3.11}$$

For a two-dimensional boundary layer, $\bar{w} = \beta = 0$, and Eq. (3.11) simplifies to Eq. (3.12). This is the Orr-Sommerfeld equation. The three-dimensional version of the Orr-Sommerfeld equation, Eq. (3.11), should be used for three-dimensional boundary layers.

$$\frac{d^4\phi}{dy^{*4}} - 2\alpha^{*2}\frac{d^2\phi}{dy^{*2}} + \alpha^{*4}\phi = iRe_l\left(\left(\alpha^*\bar{u}^* - \omega^*\right)\left(\frac{d^2}{dy^{*2}} - \alpha^{*2}\right) - \alpha^*\frac{d^2\bar{u}^*}{dy^{*2}}\right)\phi \tag{3.12}$$

For the boundary conditions, the no-slip condition at the wall implies that the disturbances in the tangential velocities, u' and w', must be zero there. The no-penetration condition implies that v' cannot vary at the wall. Without any variation in velocity, the pressure also does not fluctuate. Therefore, $\hat{u} = \hat{v} = \hat{w} = \hat{p} = 0$ for $y = 0$. The effect of boundary layer transpiration will be addressed later. Far away from the wall, the disturbances should go to zero, implying $\hat{u} = \hat{v} = \hat{w} = \hat{p} = 0$ as $y \to \infty$.

Equation (3.11) is a fourth order equation for $\hat{v}^*$, or ϕ, so four boundary conditions on ϕ are needed. So far, two boundary conditions have been specified, namely that $\phi = 0$ for $y = 0$ and $y \to \infty$. The other two boundary conditions follow from the continuity equation. The continuity equation for the disturbances says that the divergence of the disturbance velocity components is zero. Since u' and w' are zero at the boundaries of the domain, they are also invariant in the x- and z-directions, respectively. Therefore, the continuity equation implies that the variation of v' in the y-direction is also zero. So, the two additional boundary conditions on ϕ are that $\frac{d\phi}{dy^*} = 0$ for $y^* = 0$ and $y^* \to \infty$.

The next step is to determine whether boundary layer transpiration affects these homogeneous boundary conditions. In fact, the same homogeneous boundary conditions are usually kept in case of suction [49]. This implies that the disturbance velocity is zero even in the region of suction. It was found in [34] that this assumption is reasonable when the permeability of the suction surface is very small. With transpiration, this condition of no perturbation velocity at the wall should be valid, because a steady suction rate should not cause any fluctuations in time. Since the Orr-Sommerfeld equation describes the disturbance velocity, a steady suction velocity should not affect the disturbance at the wall. Therefore, the homogeneous boundary conditions at the wall are maintained with boundary layer transpiration.

Equations (3.11) or (3.12) subject to the previous boundary conditions may be used to assess the stability of a single frequency. The amplification of a disturbance may be assessed either in time or in space, respectively using the temporal or spatial formulation. As mentioned in Sec. 3.1.1, a disturbance is constant in time for a steady base flow but grows in the streamwise direction, which is why the spatial theory is preferred. In the spatial theory, the disturbance frequency ω is real and constant while the wave numbers α and β are complex [35]. Thus, $\alpha = \alpha_r + i\alpha_i$ and $\beta = \beta_r + i\beta_i$. Using Eq. (3.10), it can be seen that $i^2\alpha_i = -\alpha_i$ contributes to the growth rate of a disturbance in the x-direction. So, the sign of the imaginary component (α_i) determines whether a disturbance grows or decays in x. Similarly, β_i governs the growth rate of a disturbance in the z-direction. Regarding the sign of $-\alpha_i$, there are three possible cases:

1. If $-\alpha_i < 0$, a disturbance is damped and thus stable;
2. If $-\alpha_i = 0$, a disturbance is neutrally stable;
3. If $-\alpha_i > 0$, a disturbance is amplified and thus unstable.

The development of the N-factor, which describes the growth of a certain frequency, is given by Eq. (3.13), which is Eq. (3.4) evaluated for the spatial theory. Here, x_0 denotes the start of the unstable region.

$$N = \ln \frac{A}{A_0} = -\int_{x_0}^{x} \alpha_i \, dx = -\int_{x_0^*}^{x^*} \alpha_i^* \, dx^* \tag{3.13}$$

The N-factor from Eq. (3.13) is only valid for two-dimensional disturbances. For three-dimensional disturbances, the propagation direction is an additional unknown, for which several integration strategies exist.

Integration Strategy for N-Factor for Three-Dimensional Disturbances

For three-dimensional disturbances, it is not defined in which direction the amplification should be integrated. Therefore, several options exist. Integration strategies for the N-factor of three-dimensional disturbances were introduced in Sec. 3.1.1. There, a distinction was made between strategies using a single or multiple N-factors. More generally, four strategies are possible [56]:

1. The propagation direction of the disturbance wave is specified;
2. The wavelength of the disturbance is specified;
3. The spanwise wave number of the disturbance is specified;
4. The direction with the maximum local amplification is selected.

Following strategy 4, always selecting the direction that has the maximum amplification rate leads to a single N-factor. This is the envelope method introduced in Sec. 3.1.1, where it was mentioned that is is not the most desirable for the use with suction, because the resulting N-factor may not be unique. The preferred approach was to use two N-factors, N_{TS} and N_{CF}, each describing a single disturbance mechanism, namely the TS and CF instabilities. These N-factors will follow any of strategies 1–3.

For the TS instability, Sec. 2.3.1 stated that the streamwise direction is the most unstable, up to a Mach number of 0.9. Because of this, strategy 1 can be used for TS waves, by specifying the wave propagation to be in the streamwise direction. In this case, β would be zero. Even though this direction is not the most unstable in transonic conditions ($M > 0.9$), this strategy was used for the evaluation of the A320 flight tests [52].

For CF instabilities, strategies 2 or 3 may be used. Strategy 2 is appropriate for cross flow because CF vortices have a wavelength that is approximately constant [56]. If an infinite swept wing is considered, the flow is invariant in the spanwise direction, which implies that the spanwise growth rate β_i is zero. Therefore, setting the spanwise wave number β_r in accordance with strategy 3 is also suitable for CF instabilities. These two strategies provide almost the same results for typical wings of transport aircraft [56]. This is not surprising, as the wavelength and the wave number are related. So, either of these approaches may be used for CF. In fact, strategy 2 was used for the evaluation of the A320 flight tests [52].

For the CF instabilities, there is a further distinction to consider regarding stationary and traveling cross flow. Saric reports that stationary CF is the most important [49]. But, this is not always the case. Traveling cross flow was found to be the most unstable during flight tests of an F14 NLF glove and during the LEFT program [3]. On the other hand, suction was found to damp traveling CF more effectively than stationary CF [1]. Because of this, it is less surprising that traveling CF was most unstable on the F14, because it had no suction. However, it is surprising that stationary CF was not the most unstable for the LEFT program, because traveling CF on this HLFC application should have been most damped by the suction. Still, in most cases stationary CF may be expected to be most unstable. This argument was also used for the A320, where only stationary CF was considered [52]. This implies the additional simplification that $\omega = 0$.

The final N-factors are found from the envelope of the most amplified disturbances spanning a range of frequencies. Using strategy 1, N_{TS} is found by evaluating the amplification $N = \ln \frac{A}{A_0}$ over a range of ω, keeping β at zero. For stationary cross flow, N_{CF} is found by studying the amplification factor for a range of wave numbers at $\omega = 0$. These are either specified directly (strategy 3) or indirectly (strategy 2). Since an infinite wing is considered, $\beta_i = 0$ and the wave number β_r is specified.

When integrating growth rates, the choice of reference frame has an influence. Following the reference frame perpendicular to the leading edge, as in Fig. 3.2, a TS wave would be defined in the x-direction, which is perpendicular to the leading edge. A cross flow wave is defined perpendicular to the TS wave, which would be parallel to the leading edge in this case. On the other hand, in the reference frame aligned with the inviscid streamline, as seen in Fig. 2.5, a TS wave is aligned with the x_s-direction, and a CF wave is in the z_s-direction. These different definitions stress the importance of using the same definition of the N-factor to compare data, as mentioned in Sec. 3.1.1. In fact, the x_s-direction is the most unstable for TS waves up to near-sonic conditions [3]. Furthermore, CF instabilities are most unstable very close to the cross flow direction z_s and this direction is hardly affected by compressibility [3]. If two N-factors are used, the streamline reference frame seems to be the preferred choice because it better aligns with the prime unstable directions.

3.4. Working Principle of Existing Transition Prediction Tool

A transition prediction tool already exists at TU Delft, which was developed as part of the joint research project with Embraer, described in Sec. 1.1. It contains two main components: a boundary layer solver and a stability solver. The desired output is a transition location. However, since the tool is based on the e^N-method, an envelope of N-factor growth will be its final output. As mentioned in Sec. 3.1.1, the predicted transition location must be calibrated with a critical N-factor derived from experimental results.

Performing a stability analysis requires a boundary layer solution of the base flow. The existing tool contains a laminar boundary layer solver to produce the required input. Other methods may also be used to obtain the base flow solution, such as CFD. However, CFD is more time-consuming than a laminar boundary layer solver. Moreover, the current solver is fully integrated into the existing tool, so it is more user-friendly.

The two main components of the transition prediction tool, a boundary layer solver and a stability solver, are examined in Secs. 3.4.1 and 3.4.2, respectively. The input for the stability solver is a boundary layer solution, which requires distributions of pressure and edge velocity as its own inputs, as illustrated by the flow chart of the tool in Fig. 3.3. The input data may be obtained experimentally or numerically, for example with XFOIL[1]. The tool suite consists of solvers developed at TU Delft, which were integrated into a cohesive framework by Boersma, as reported in [9], where the tool is described in more detail.

[1] `http://web.mit.edu/drela/Public/web/xfoil/`

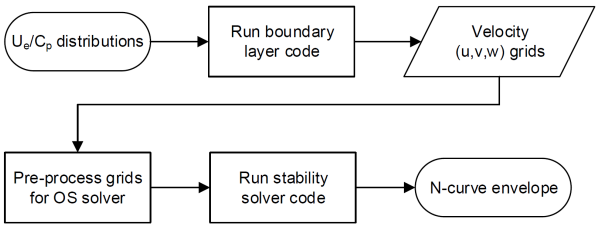

Figure 3.3: Flow chart of the transition prediction tool [9]

3.4.1. Boundary Layer Solver

The boundary layer equations, as presented in Sec. 3.3.1, are solved in dimensional form. The boundary conditions include the no-slip condition, which implies that u and w are zero at the wall. Far away from the wall, u and w are equal to the outer flow. The no-penetration condition is used for v, which implies that wall transpiration is not considered, requiring a modification for HLFC, which will be described in Sec. 3.5.

Solution Procedure

Due to the parabolic nature of the boundary layer equations, as mentioned in Sec. 3.3.1, a marching procedure in the streamwise direction is used to solve them. The initial condition is taken as the solution of a three-dimensional Falkner-Skan-Cooke flow corresponding to the same outer velocities and pressure gradient as the first station. For each discretization step, the surface is assumed to correspond to a flat plate with an outer velocity given by the input data.

Furthermore, only the momentum equation in the z-direction contains terms involving w. Therefore, Eq. (3.7b) is decoupled from the others. So, w may be solved for after u and v have been found. This implies that Eqs. (3.6) and (3.7a) are used to iteratively solve for u and v. In fact, u is solved for using the x-momentum equation, while v is solved for using the continuity equation.

Some rewriting of the continuity equation (Eq. (3.6)) enables solving for v directly. This is indicated by Eq. (3.14). This equation can be used to solve for v up to an arbitrary integration constant. In the original implementation of the boundary layer solver, the integration constant is selected such that v is exactly zero at the wall. In other words, this is used to satisfy the no-penetration boundary condition. Boundary layer transpiration will affect this part of the solver.

$$v(y) = -\int_{y_0}^{y} \frac{\partial u}{\partial x} d\tilde{y} \tag{3.14}$$

The marching procedure progresses until laminar separation. Once laminar separation occurs, it is likely that the flow would have become turbulent before this point, or would become turbulent shortly afterwards. Beyond the point of laminar separation, a laminar boundary layer solution is therefore no longer relevant.

Discretization

In the computational domain, the boundary layer equations are discretized onto a rectangular grid. The coordinate directions are the streamwise direction s and the wall-normal direction y. Because the surface of an aerodynamic body is usually curved, the 'streamwise' direction s follows the trajectory along the surface, parallel to x. Therefore, the length progressed along this path is longer than the usual reference length (chord). At every point along s, the coordinate y is defined perpendicular to the local orientation of the surface.

While the trajectory is curved in reality, at each station the coordinate directions are normal to each other and are thus mapped onto a rectangular domain in the computational space. The domain in the streamwise direction starts from the stagnation point or the attachment line and ends after progressing the entire arc length along one side of the aerodynamic body. In the wall-normal direction, the domain has a fixed height, large enough to capture the boundary layer at the end of the streamwise direction, where it is usually thickest.

The boundary layer solver uses different types of discretization in the tangential (s) and the wall-normal (y) directions. The tangential direction s is discretized with an implicit finite difference scheme with second-

order accuracy. On the other hand, the wall-normal direction y is discretized with a spectral method.

For an implicit finite difference scheme, the solution and all its derivatives are evaluated at the next station. Because a marching procedure is used in s, only the solutions at upstream locations are known. Therefore, the implicit scheme can only make use of the upstream data points. In other words, an upwind differentiation scheme is used in this implicit formulation.

While finite difference schemes represent the solution of a numerical problem with local solutions, spectral methods represent the solution with global basis functions. These basis functions are defined continuously on the entire domain and are combined to recreate the solution. In case of the existing tool, Chebyshev polynomials are used as the basis functions. Chebyshev polynomials are essentially a Fourier cosine series with a change of variable [10]. These basis functions are used to solve the numerical problem at a set of collocation points, where the governing equation is satisfied exactly. In the existing tool, a cosine spacing is used for the collocation points. This distribution puts more points near the edges of the domain, preventing strong polynomial oscillations that occur with uniform spacing. For a collocation method such as this, using cosine-spaced points, derivatives of a discretized function can be written as a matrix multiplication. This is convenient, because derivatives in y appear in the tool as matrices in the discrete governing equations.

3.4.2. Stability Solver

The stability solver uses the three-dimensional formulation of the Orr-Sommerfeld equation (Eq. (3.11)) as its primary option. Homogeneous boundary conditions are used, which should also be suitable for boundary layer transpiration, as stated in Sec. 3.3.2. In agreement with Sec. 3.3.2, the tool evaluates the TS instability with $\beta = 0$ and the stationary CF instability with $\omega = 0$. The existing tool uses the spatial theory to solve the Orr-Sommerfeld equation, which is the preferred formulation as indicated in Sec. 3.3.2.

With either ω or β_r known for a TS or CF disturbance, respectively, the Orr-Sommerfeld equation becomes an eigenvalue problem for the eigenvalue α and the corresponding eigenfunctions. Subsequently, the N-factor is calculated using the imaginary component of α. Performing the analysis over a range of frequencies, both for TS waves and stationary CF, yields the desired output of the tool: an envelope of N-factors.

Discretization of the Orr-Sommerfeld equation in y is also done using the spectral method, similar to the boundary layer solver discussed in Sec. 3.4.1. Using Chebyshev polynomials to represent the eigenfunctions, collocation points are placed with a cosine spacing. Contrary to the boundary layer solver, the placement of the midpoint of this distribution is flexible, allowing more detail near the wall while removing some points far away from the wall where such detail is not required. In fact, it was found that the midpoint should be placed near the point of maximum curvature in the velocity profile, both for TS and CF instabilities [9]. On the other hand, the point furthest away from the wall had to be placed even beyond the extent of the boundary layer thickness, such that the decay of the disturbances far away from the wall is properly captured [9].

Another variable is the number of collocation points, or the number of Chebyshev polynomials that are used to represent the eigenfunctions. The number of polynomials determines the number of eigenvalues and eigenfunctions that are obtained. In fact, there are as many eigenvalues as there are Chebyshev polynomials. However, only one eigenvalue corresponds to the physical disturbance mechanism. In the tool, it is found through a filtering process, explained in more detail in [9].

Essentially, the filter looks at the eigenfunctions corresponding to the eigenvalues. It selects the correct one by eliminating those eigenfunctions that do not look like the expected eigenfunction for a certain disturbance. For example, the eigenfunctions of TS and CF disturbances typically have a single, smooth maximum. Furthermore, the maximum disturbance should be located within the boundary layer thickness.

The number of polynomials affects how accurately a disturbance can be captured. Unstable modes need fewer polynomials to capture the disturbance accurately, while stable modes need more [9]. Because the stability of a certain frequency is not known in advance, the entire parameter space should be studied with many polynomials. In view of computational time, using fewer polynomials in the unstable region is desirable.

Therefore, the solution procedure consists of two parts. First, the disturbance parameter space is dis-

cretized into a coarse grid, containing few points which are resolved using many Chebyshev polynomials. This captures the unstable but also the stable modes. The low number of data points limits the computational time associated to using many polynomials. These results are used to identify the unstable part of the parameter space, within which a second, refined grid is applied. Because the modes are unstable, fewer polynomials are required. This speeds up the computation, allowing more unstable data points to be captured.

The disturbance parameter space is defined by the disturbance frequency and the boundary layer flow. For the frequency of TS waves, the nondimensional frequency ω^* is used as the governing parameter, which is given by Eq. (3.15) according to the scaling conventions from App. B. The boundary layer flow is characterized by the Reynolds number based on the Blasius length scale (Re_l), given by Eq. (3.16). Two-dimensional grids, coarse and fine, spanning ω^* and Re_{δ_r} are used to solve the Orr-Sommerfeld equation. Instead of ω^*, it also possible to use the nondimensional frequency F, given by Eq. (3.17) [35]. For a traveling TS wave, the dimensional frequency ω is constant [35]. However, the nondimensional frequency ω^* varies with x, whereas F remains constant provided that the reference velocity U is constant.

$$\omega^* = \omega \frac{l}{U} \tag{3.15}$$

$$Re_l = \frac{Ul}{\nu} = \sqrt{Re_x} \tag{3.16}$$

$$F = \frac{\omega^*}{Re_l} = \omega \frac{\nu}{U^2} \tag{3.17}$$

For a CF disturbance, a similar parameter space is used, except that now the spanwise wave number β_r characterizes the disturbance wave. In addition to the same Reynolds number, the nondimensional wave number β_r^*, defined by Eq. (3.18), is used. Like for a TS wave, another nondimensional parameter can be defined in a similar way as F, namely the nondimensional spanwise wave number, B, given by Eq. (3.19).

$$\beta_r^* = \beta_r l \tag{3.18}$$

$$B = \frac{\beta_r^*}{Re_l} = \beta_r \frac{\nu}{U} \tag{3.19}$$

Once solutions of the Orr-Sommerfeld equation have been computed on the fine grid of unstable parameters and the correct eigenvalues identified, the N-factors can be computed. One N-factor curve is obtained per frequency and per instability. The growth rates α_i are integrated in the x-direction. As mentioned previously, this integration should be done for a constant dimensional disturbance frequency, which is realized in the existing tool by integrating along lines of constant nondimensional frequency, F, for TS or nondimensional wave number, B, for CF, to obtain the N-curves. These lines pass through the grid on which the solutions were evaluated, requiring interpolation in between the known data. The benefit of this is that an arbitrary number of frequencies can be tested, so long as they lie within the grid. Thereby, many N-curves are obtained, allowing the envelope of maximum amplification to be determined.

3.5. Modifications to Transition Prediction Tool

The existing transition prediction tool described in Sec. 3.4.1 does not account for boundary layer suction, requiring a modification before the tool can be used to predict transition in the context of HLFC. This has several implications, first of which is the necessary modification of the boundary condition on the wall-normal velocity, which is described in Sec. 3.5.1. Furthermore, the input of a suction distribution into the tool is discussed in Sec. 3.5.2. Finally, the effect of boundary layer transpiration on stability is treated in Sec. 3.5.3.

3.5.1. Modification of Boundary Condition on Wall-Normal Velocity

As given by Eq. (3.8), the original boundary layer solver uses a no-penetration condition at the wall. However, HLFC involves boundary layer suction, implying a nonzero wall-normal velocity at the wall. According to Eq. (3.14), v is solved by integrating the continuity equation. After integration, the velocity at the wall is set to zero, so that the no-penetration condition is satisfied. With boundary layer transpiration, the specified transpiration velocity v_w can therefore directly be added to the existing solution for $v(y)$, as shown in Eq. (3.20).

Here, $v|_{y=0}$ is first subtracted to satisfy the no-penetration condition. Then, the transpiration velocity v_w is added. Since v is defined positive away from the wall, suction implies a negative sign of v_w. Note also that this modification allows both positive (blowing) and negative (suction) transpiration velocities.

$$v(y) = -\int_{y_0}^{y} \frac{\partial u}{\partial x} d\tilde{y} - v|_{y=0} + v_w \tag{3.20}$$

The continuity equation remains satisfied by adding a wall transpiration velocity, because it only dictates the variation in $v(y)$, which is left unchanged. The transpiration velocity is part of the integration constant emerging from the integration of the continuity equation, which does not modify $\frac{\partial v}{\partial y}$. This modification does not affect the original capabilities of the boundary layer solver. The no-penetration condition can still be satisfied by setting v_w to zero along the surface. The only difference with the original tool is that an additional input needs to be specified, which is addressed next.

3.5.2. Input of Suction Distribution

Generally, the transpiration velocity varies along the surface, so the tool must enable its user to specify a distribution of transpiration. Two ways of specifying the suction distribution are desired: a direct and an indirect way. The direct approach is useful when the suction velocity distribution is known, as is typically the case for validation data. The indirect approach is related to the practical implementation of an HLFC system, where the pressure difference across the suction surface drives the suction rate. The internal and external pressures are usually known, whereas the suction rate is a dependent variable. Hence, evaluating the suction rate for such an approach requires a model linking the pressure drop across the surface to the suction rate, for which the investigation from Chap. 5 is relevant.

Atkin created a suction system design tool using such an indirect approach to the suction distribution in [4]. The starting point for this tool was the specification of suction chambers, both in terms of their location and internal pressure. The suction rate was estimated using a model for the pressure drop across the skin. Furthermore, the critical suction limit was also taken into account, using an unvalidated criterion.

This approach shows multiple important aspects. First, a good model relating the pressure drop to the suction velocity is needed. This is reflected in the road map in Fig. 1.1, where the capability to design the layout of a suction system requires such a model. Moreover, it is important that this model cover much of the design space if it is intended to be used in a flexible manner. Therefore, it must first be established whether the pressure losses for a wide range of applications can be captured in a single model, which motivated the experimental investigation into the scalability of these pressure losses in the present research (Chap. 5). A second important element of the approach from [4] is that the critical suction limit should not be exceeded for a proper design, which was also identified in the road map from Fig. 1.1.

In addition, it shows the importance of starting the design with a definition of the internal layout of the suction system. Because this layout dictates the suction distribution, not all desired suction distributions are compatible. By designing the internal layout first, the issue of incompatibility with the suction system is avoided. In [4], Atkin used multiple suction chambers, while the trend toward simplified suction systems focuses on single chambers, such as in Fig. 2.16. Still, with a single suction chamber, the flow rate is generally controlled by throttling holes connected to small compartments below the surface. These compartments could also been seen as individual 'pressure chambers' with their own internal pressure. Therefore, both options can be modeled as multiple suction chambers. But, the pressures in the individual compartments should be compatible with the throttling holes and the main pressure in the large pressure chamber. The additional pressure loss due to these orifices must be accounted for in the design of an HLFC component.

Regardless of the way the suction distribution is created, it has to find its way into the solver. The most convenient is to do it alongside the definition of the outer pressure and velocity distributions. These inputs already exist, indicated by the starting point in Fig. 3.3, so it is straightforward to add an additional input here.

However, the distributions of pressure and edge velocity are usually defined with a limited number of points. These are later interpolated onto a more refined grid in the boundary layer solver. Because these distributions are continuous and usually fairly smooth, a low number of points is not a problem for the interpolation. But, the suction distribution may be discontinuous, requiring more points in some places. The

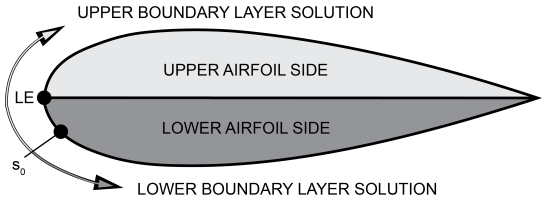

Figure 3.4: Difference between upper and lower boundary layer solutions, divided by the stagnation point s_0, and the upper and lower airfoil surfaces, divided by the leading edge, on which suction distributions are defined

amount and location of the points defining the suction distribution need not agree with the other inputs.

Therefore, a separate grid was introduced on which the suction distribution is defined. This way, the user will have complete flexibility over the definition of the suction distribution, irrespective of the other inputs. It will also be useful whenever a certain suction distribution should be duplicated into the tool. In fact, as the boundary layer solver is executed per airfoil side, two grids for the suction distribution were introduced: one for the upper and one for the lower surface. Again, these two grids need not have the same definition.

Boundary layer solutions are obtained starting from the stagnation point, while the upper and lower sides are divided by the leading edge point, which generally do not coincide. Depending on the location of the stagnation point relative to the leading edge, the suction distributions from both airfoil sides may be required for one boundary layer solution, as illustrated in Fig. 3.4. Hence, the tool was modified to detect where the stagnation point is, and—if necessary—to combine the suction distributions from both sides accordingly.

3.5.3. Modification of Stability Solver

Section 3.4 described that the existing transition prediction tool uses the Orr-Sommerfeld equation in its linear stability solver. This was not created with suction in mind. But, as Sec. 3.3.2 described, the homogeneous boundary conditions can be maintained in the Orr-Sommerfeld equation with transpiration, because a steady transpiration velocity should not introduce any disturbance in the flow.

Because of this, no modifications to the existing stability solver were anticipated. In fact, the stability solver itself did not need to be modified. However, applications with suction showed that the preprocessing for the stability solver required modifications. In particular, the internal process for determining the grid on which the disturbance parameter space is discretized and solved was found incompatible with suction in case of the TS instability. Conversely, no difficulties arose for the CF instability.

Modification of Stability Preprocessing for TS Instability

The issue with the preprocessing for the stability solver was identified with the validation case from Sec. 4.2.4. This case is used here to illustrate the modifications to the stability preprocessing. The case concerns a flat plate, on which suction was applied through a short strip to create a stabilizing effect on the boundary layer. Suction was applied at a point where TS instabilities had already started growing, which led to two unstable regions: upstream and downstream of the suction strip, separated by the stable region where suction was applied. In the existing implementation, only the final unstable region was considered for the TS instability. This was done in order to ignore any minor instabilities upstream. However, with the application of suction, it is important to consider all unstable regions, because instabilities that have grown upstream are not necessarily damped completely with suction. Therefore, it is important in the general case that N-curves are able to pass through stable regions, and can continue growing in the subsequent unstable regions.

In order to do this, the disturbance parameter grid should be a single region enclosing all unstable parts of the domain. A single region is required so that N-curves belonging to a single frequency pass through the entire grid. This is illustrated in Fig. 3.5a, which features two unstable regions. Because there are no data points evaluated in the stable region where suction is applied, lines of constant nondimensional frequency (F), which are straight lines through the origin, do not pass through the stable region. In comparison, the modified grid limits in Fig. 3.5b allow lines of constant F to pass through the stable region, so that the growth and decay of single frequencies is captured over the entire plate.

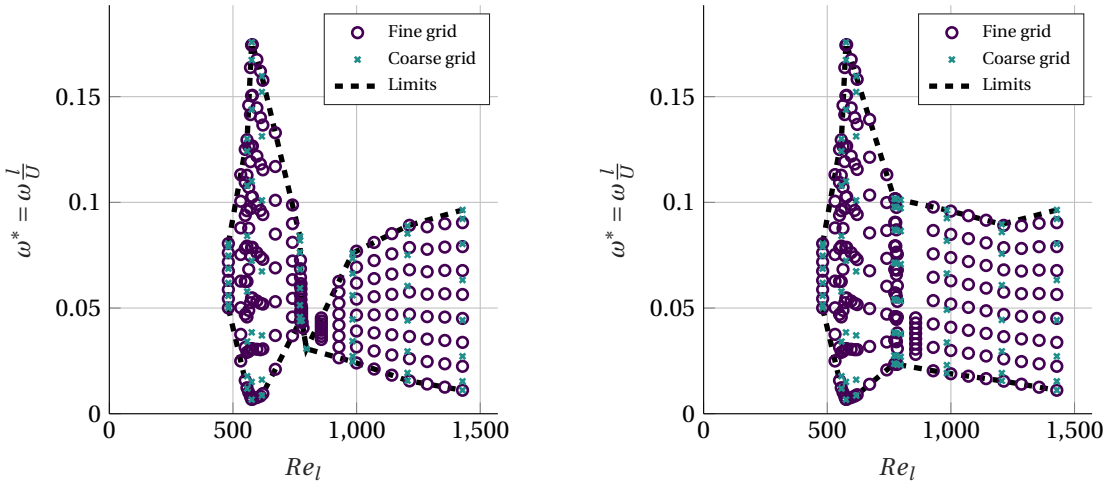

(a) Original (b) Modified

Figure 3.5: Original and modified grid limits for TS instability corresponding to validation case from Sec. 4.2.4

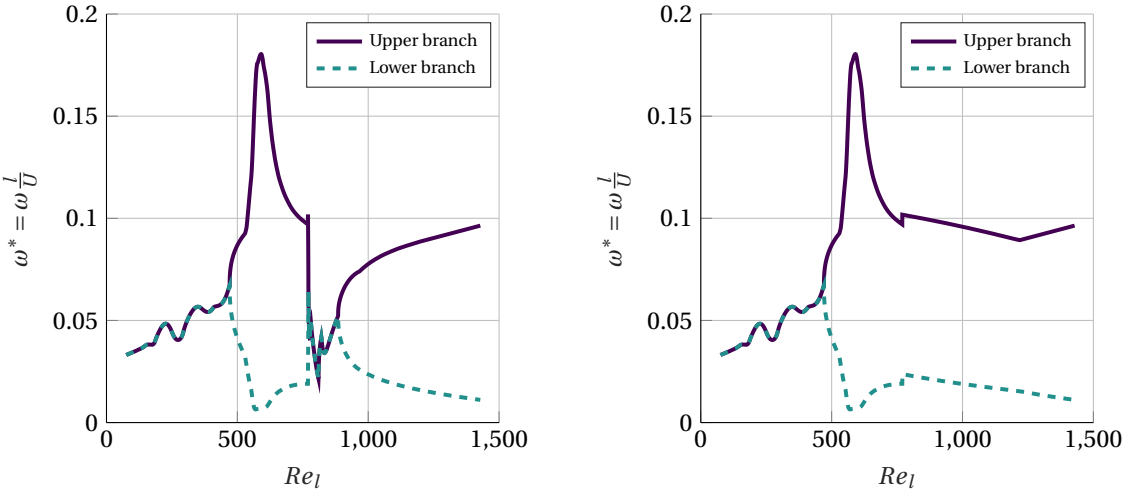

(a) Original (b) Modified

Figure 3.6: Original and modified neutral curves for TS instability corresponding to validation case from Sec. 4.2.4

The question was how the grid limits could be adjusted in such a way that the process is automatic and works for arbitrary cases. To do that, it is first important to understand how the grid limits are set. In fact, the grid limits for the TS instability are set according to an estimate of the neutral curves for the given boundary layer solution, within which the boundary layer is expected to be unstable. The neutral curves are estimated based on the shape factor and the gradient of the velocity profile at the wall. Using H to correlate the neutral curves is supported by the research from van Ingen, who demonstrated that stability diagrams can be characterized by the shape factor [76]. In addition, he showed that the effects of pressure gradient and suction are interchangeable [76], which suggests that this approach is also suitable with suction.

Suction can cause the boundary layer to appear too stable, as evident from the original neutral curves in Fig. 3.6a, where the upper and lower curves overlap in the area of suction, indicating that the solution is stable there. However, it is desired to make the solution appear less stable, such that the neutral curves from the unstable regions get connected, thereby allowing N-curves to be integrated across the stable region.

In order to create an apparent unstable solution, it is desired to treat the boundary layer as if suction was not present. Therefore, the inputs for estimating the neutral curve were modified, such that they negate the

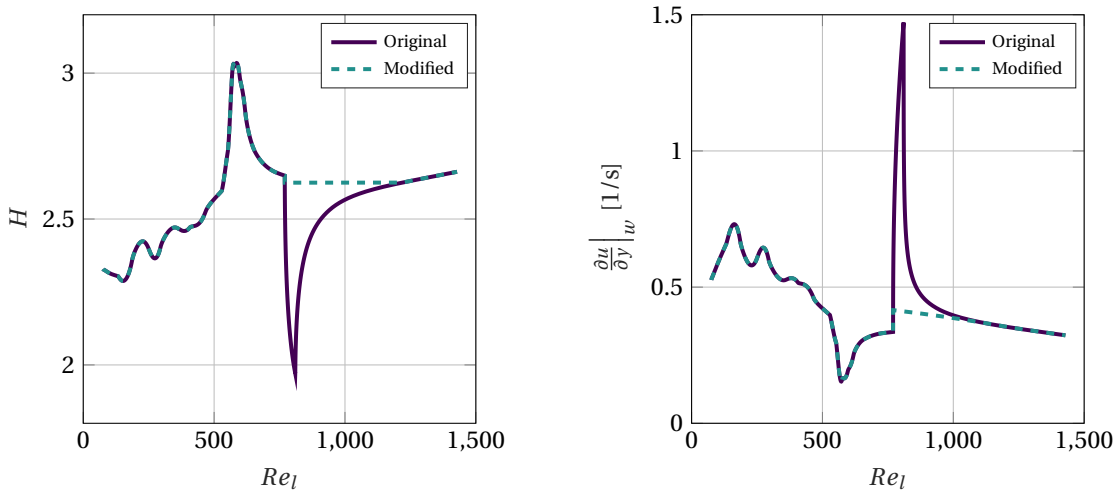

(a) Shape factor

(b) Gradient of velocity profile at the wall

Figure 3.7: Original and modified boundary layer properties to remove the effect of suction for TS instability corresponding to validation case from Sec. 4.2.4

effect of suction. Suction makes the boundary layer profile more full, which implies that H reduces and $\frac{\partial u}{\partial y}$ increases with suction. The effect of suction was removed by constructing an artificial solution, which cuts off those parts of the solution influenced by suction. In fact, the algorithm was to find the first location where H reduces due to the application of suction. Then, the local value of H at this point was taken as a reference. Next, the downstream location where H of the original solution first exceeds the reference value is found. If the location meeting this condition cannot be found, the end of the domain is selected. Finally, a linear interpolation in H is applied between these two locations. Similarly, the gradient of the velocity profile was modified between the same locations as H, also by performing a linear interpolation. The procedure is illustrated in Fig. 3.7. The procedure is repeated when multiple regions with a stabilizing influence of suction are identified. The procedure was not applied with blowing because blowing tends to destabilize the boundary layer, which should be compatible with the original implementation.

With the modified boundary layer properties, the neutral curves are predicted. For the case of Sec. 4.2.4, this led to Fig. 3.6b, which subsequently served to create the solution grid from Fig. 3.5b. This grid contains all unstable parts and is suitable for the integration of N-curves through the stable region.

Other solutions that were considered include using the grid limits from the same case without suction and creating a rectangular grid that encloses the original neutral curves. However, using the case without suction requires a separate boundary layer solution, which must be stored internally and adds computational time. Furthermore, cases without suction may feature laminar separation further upstream that with suction, which leads to an incomplete solution. Finally, using a rectangular grid would be the most robust, but it would include a large part of the stable domain, which yields many unnecessary computations.

Modification of Stability Preprocessing for CF Instability

Modifications to the preprocessing for the CF instability were not required, which became evident from the validation case from Sec. 4.2.5, which deals with a swept wing on which cross flow is dominant. As illustrated by Fig. 3.8, there is little difference between the limits in nondimensional wave number for the case with and without suction. In fact, this is because the limit for the wave number is mainly based on the sweep angle. Therefore, suction is generally not expected to affect the grid limits for the CF instability.

The resulting grid for CF is typically nearly rectangular, which is particularly suitable for the integration of N-curves along lines of constant B, which are straight lines through the origin. Therefore, the existing implementation of the stability solver is compatible with suction.

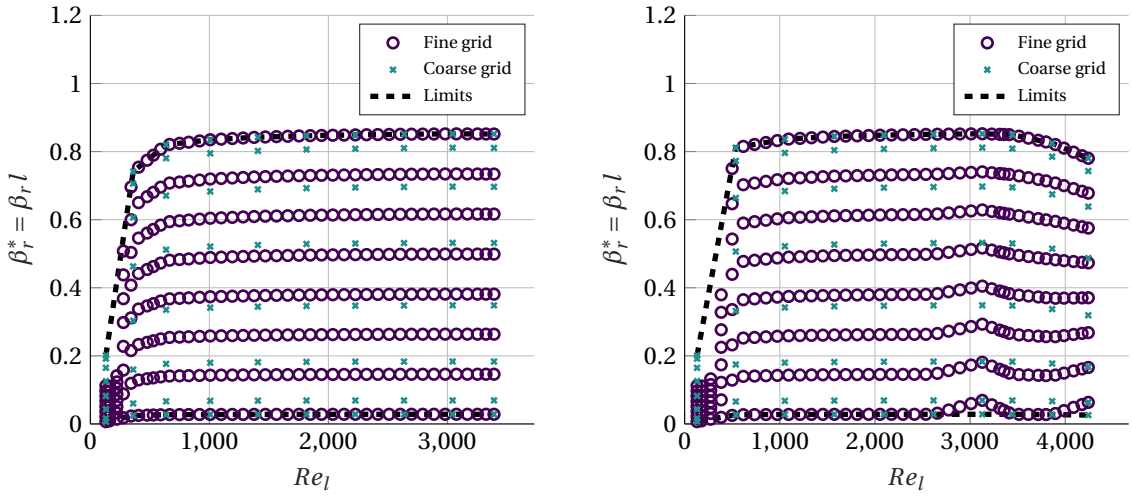

(a) Without suction

(b) With suction

Figure 3.8: Grid limits for CF instability with and without suction corresponding to validation case from Sec. 4.2.5

4

Numerical Results

The modified numerical tool must be verified and validated. Verification is the process of checking that the tool functions properly. That is to say, it should give the expected outcome for a certain case with a known solution. This aspect is treated in Sec. 4.1. On the other hand, validation is the process of checking that the tool meets the original goal of predicting transition for HLFC applications. Subsequently, the tool should enable the design of an HLFC component. This facet is covered in Sec. 4.2.

4.1. Verification

During the verification stage, the modified boundary layer solver is tested with cases involving a boundary layer with transpiration for which an exact solution is available. Two suitable cases emerge from literature, namely a constant suction rate applied to a flat plate and a variable transpiration rate applied to a flat plate, leading to a self-similar boundary layer solution.

4.1.1. Constant Suction Rate on Flat Plate

For a flat plate with a constant suction rate, the boundary layer solution is not self-similar. In fact, the boundary layer profile changes from the Blasius solution at the leading edge into an asymptotic suction profile [78]. This case is interesting because it approaches the asymptotic suction profile, for which the analytical boundary layer solution is known. For a formal derivation, the reader is referred to [50]. This case was also used in [72] for validating a numerical implementation of boundary layer transpiration.

The asymptotic suction boundary layer follows by assuming that $v_w \to -\infty$. In other words, the suction rate is massive. In this case, the wall-normal velocity is constant within the boundary layer, expressed by Eq. (4.1). Usually there is a variation in $v(y)$, but now the suction rate is so large that the change in v is not noticeable. The solution for the tangential velocity profile is exponential and is given by Eq. (4.2).

$$v(x,y) = v_w(x) \tag{4.1}$$

$$u(x,y) = U_e(x)\left(1 - e^{\frac{v_w(x)}{\nu}y}\right) \tag{4.2}$$

In case of a flat plate with uniform suction, both the external velocity U_e and the suction rate v_w are independent of x. This implies also that the boundary layer solution is independent of x. In other words, the boundary layer has constant properties in the streamwise direction. The high suction rate prevents the boundary layer from growing, which is also expressed by the integral properties, given by Eqs. (4.3).

$$\delta^* = -\frac{\nu}{v_w}; \quad \theta = -\frac{\nu}{2v_w}; \quad H = 2 \tag{4.3}$$

When the suction rate on a flat plate is large enough and the plate is sufficiently long, the boundary layer solution should tend towards this asymptotic suction profile. This condition was checked with the modified boundary layer solver, using a flat plate with a length (L) of 10 m, a freestream velocity (U_∞) of 10 m/s, and

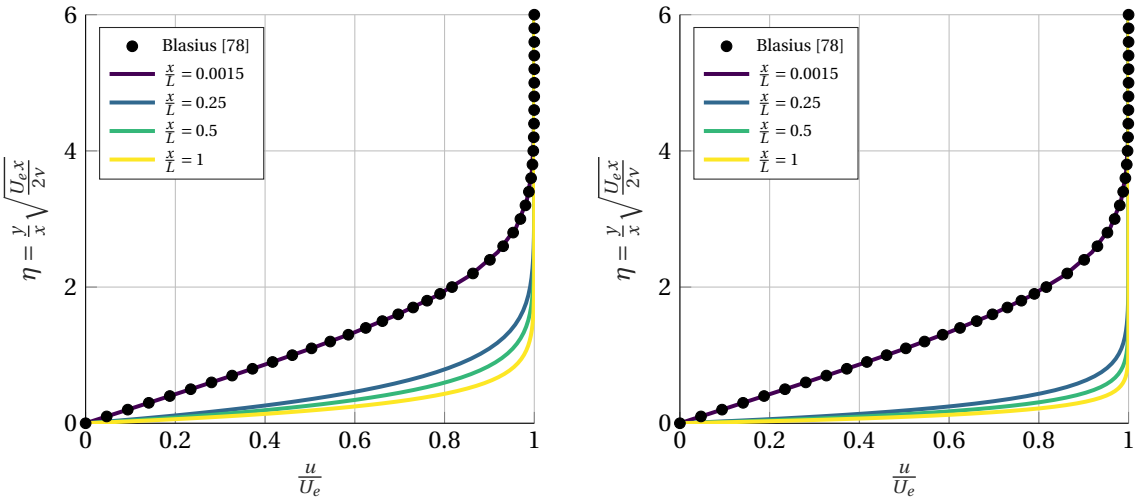

(a) $-\frac{v_w}{U_e} = 0.001$ (b) $-\frac{v_w}{U_e} = 0.002$

Figure 4.1: Nonsimilar velocity profiles on flat plate with constant suction rate

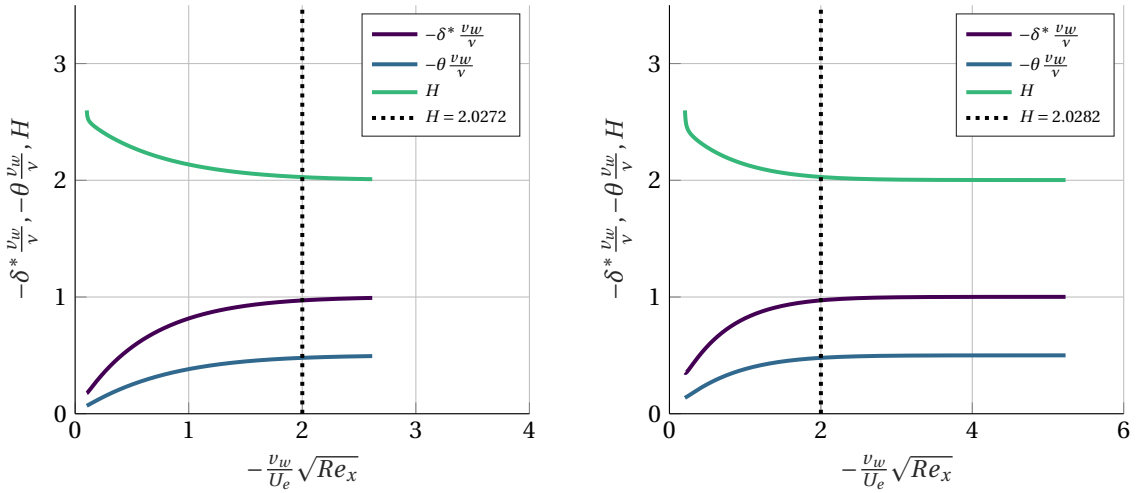

(a) $-\frac{v_w}{U_e} = 0.001$ (b) $-\frac{v_w}{U_e} = 0.002$

Figure 4.2: Development of boundary layer integral properties along length of plate with constant suction rate

standard atmospheric conditions ($T = 288.15$ K, $\rho = 1.225$ kg/m^3, $\mu = 1.79 \cdot 10^{-5}$ kg/(m·s)). Two different suction rates were tested, namely $-\frac{v_w}{U_e} = 0.001$ and $-\frac{v_w}{U_e} = 0.002$.

First, showing the streamwise boundary layer velocity profiles at several positions along the plate, as in Fig. 4.1, proves that the profiles are not self-similar. As expected, the velocity profiles at the beginning of the plate ($\frac{x}{L} = 0.0015$) follow the Blasius solution, after which the profiles rapidly become fuller due to the high suction rate. Moreover, comparing Fig. 4.1b to 4.1a shows the expected result that the velocity profiles are even more full when the suction rate is doubled.

In fact, the development of the velocity profiles can be seen in Fig. 4.2. It shows that the integral properties approach the values for the asymptotic suction profile, as given by Eq. (4.3). Furthermore, according to [50, 78], the asymptotic suction profile is reached when $-\frac{v_w}{U_e}\sqrt{Re_x} \approx 2$. At this point, indicated by the vertical line in Fig. 4.2, H should be less than 2.02 [50], which is closely matched by the boundary layer solver.

Finally, the boundary layer velocity profiles obtained with the modified solver were compared to the asymptotic boundary layer profiles, given by Eqs. (4.1) and (4.2). For the tangential velocity profiles shown in

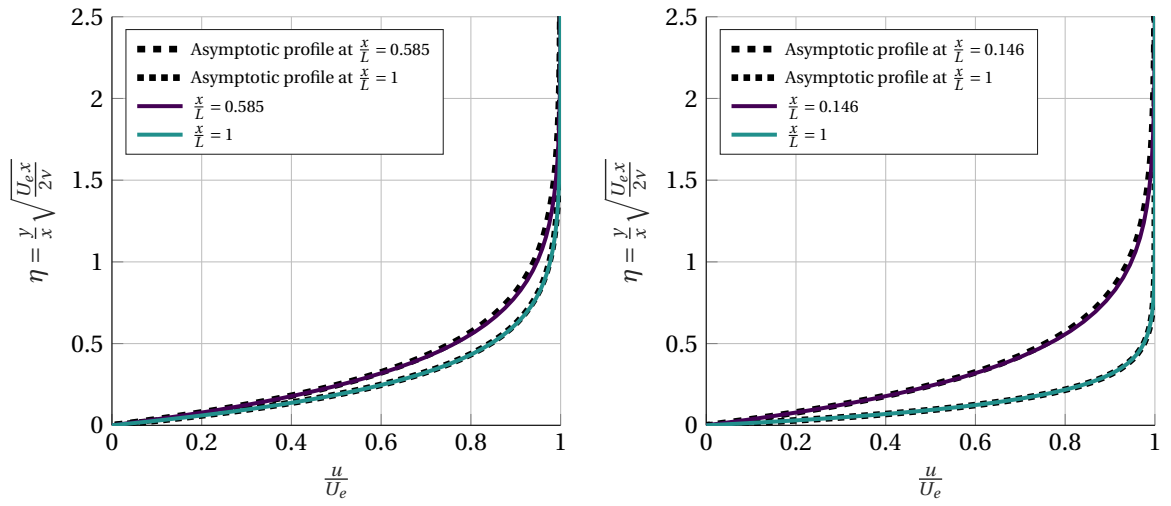

(a) $-\frac{v_w}{U_e} = 0.001$ (b) $-\frac{v_w}{U_e} = 0.002$

Figure 4.3: Comparison of tangential velocity profiles with asymptotic suction profile at the location where $-\frac{v_w}{U_e}\sqrt{Re_x} \approx 2$ and at the end of the plate

Fig. 4.3, the profiles at $-\frac{v_w}{U_e}\sqrt{Re_x} \approx 2$ almost match the asymptotic suction profile, which is as expected for this condition. At the end of the plate, the numerical and analytical profiles essentially overlap. For the wall-normal velocity profiles shown in Fig. 4.4, the profiles at $-\frac{v_w}{U_e}\sqrt{Re_x} \approx 2$ have less than 1.5% error with respect to the analytical solution, with the error decreasing with the distance along the plate. Due to the excellent agreement with theory, verification is considered successful for this case.

4.1.2. Self-Similar Transpiration on Flat Plate

The second verification case is a flat plate that has a variable transpiration rate that results in a self-similar boundary layer profile. This self-similar boundary layer solution is obtained by maintaining a constant value of the suction-blowing parameter, $\tilde{v}_w$, which is given by Eq. (4.4) [78].

$$\tilde{v}_w = \frac{v_w}{U_e}\sqrt{Re_x} \tag{4.4}$$

Self-similar boundary layer profiles result for suction ($\tilde{v}_w < 0$) and for blowing ($\tilde{v}_w > 0$). Some velocity profiles for a range of $\tilde{v}_w$ are presented in [78] and can be used for comparison. These are shown in Fig. 4.5.

Retaining the same values of the suction-blowing parameter as in Fig. 4.5, boundary layer solutions were obtained with the modified tool, using the same external conditions as in Sec. 4.1.1: $L = 10$ m, $U_\infty = U_e = 10$ m/s, and standard atmospheric conditions ($T = 288.15$ K, $\rho = 1.225$ kg/m^3, $\mu = 1.79 \cdot 10^{-5}$ kg/(m·s)). Because of the initial conditions, the boundary layer profile will start as the Blasius solution, but will turn into the self-similar solution dictated by the selected value of the suction-blowing parameter. Allowing for the self-similar solutions to develop, Fig. 4.6 shows the velocity profiles at the end of the plate. Comparing these results to Fig. 4.5 shows good agreement.

The development of the self-similar solutions is illustrated by the evolution of the shape factor over the plate in Fig. 4.7. Note that $\tilde{v}_w = 0$ corresponds to the Blasius solution, which has a shape factor of 2.59 [78]. Furthermore, Fig. 4.7 shows that cases with blowing settle into the self-similar solution slowly, as compared to cases with suction. The two extremes, $\tilde{v}_w = -2$ and $\tilde{v}_w = 0.6$, are illustrated in Fig. 4.8. With $\tilde{v}_w = -2$, the self-similar solution is reached almost immediately, while it takes longer for $\tilde{v}_w = 0.6$, but it is reached eventually. From these results, and the good agreement between Figs. 4.5 and 4.6, it can be concluded that the modified boundary layer solver has been successfully verified.

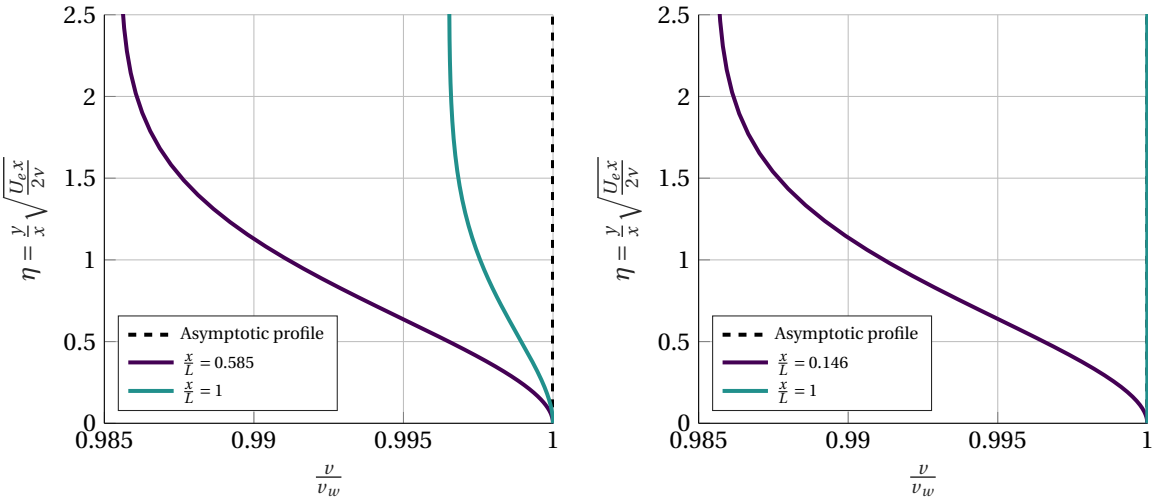

(a) $-\frac{v_w}{U_e} = 0.001$ (b) $-\frac{v_w}{U_e} = 0.002$

Figure 4.4: Comparison of wall-normal velocity profiles with asymptotic suction profile at the location where $-\frac{v_w}{U_e}\sqrt{Re_x} \approx 2$ and at the end of the plate

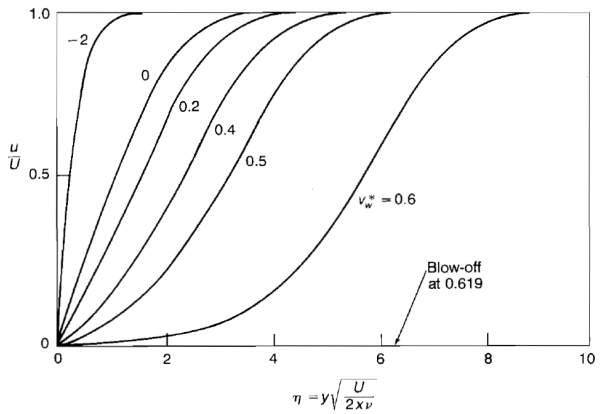

Figure 4.5: Self-similar boundary layer velocity profiles for various values of the suction-blowing parameter [78]. Note that v_w^* is used in the figure whereas $\bar{v}_w$ is used in the text to denote the suction-blowing parameter. This notation in the text is used to avoid confusion with the convention of indicating nondimensional variables

4.2. Validation

For the validation process, the goal is to establish whether the tool—with the incorporated modifications—is suitable to design an HLFC component. The entire chain from the boundary layer solution to the stability analysis and transition prediction should be tested. Therefore, the validation cases should include information about the boundary layer and the transition location. Furthermore, these cases should involve boundary layer suction, where suction through a perforated sheet is preferred to slot suction. Since HLFC on a transonic aircraft involves sweep, validation data obtained on swept wings is valuable.

The bibliography by Bushnell and Tuttle is an excellent starting point to locate validation cases [14]. They categorized validation data according to their application. Preference was given over flight tests, as they were performed in the actual disturbance environment in which HLFC will be applied. Wind tunnel tests are also mentioned, where data acquired in low-disturbance tunnels is recommended.

Since the bibliography by Bushnell and Tuttle was published in 1979, it does not contain any recent experiments. However, more recent validation data that is publicly available is not prevalent, proving the value of older validation cases. Three cases suitable to validate the boundary layer solver emerge from literature. In increasing order of complexity, Sec. 4.2.1 starts with suction applied to a flat plate, Sec. 4.2.2 investigates

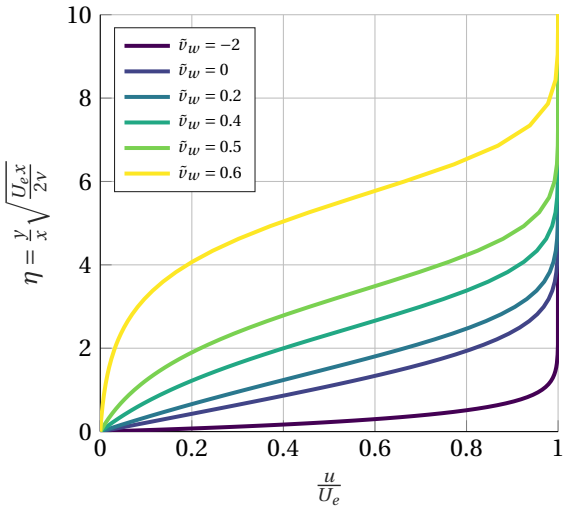

Figure 4.6: Self-similar boundary layer velocity profiles for same values of the suction-blowing parameter as in Fig. 4.5, obtained with numerical tool

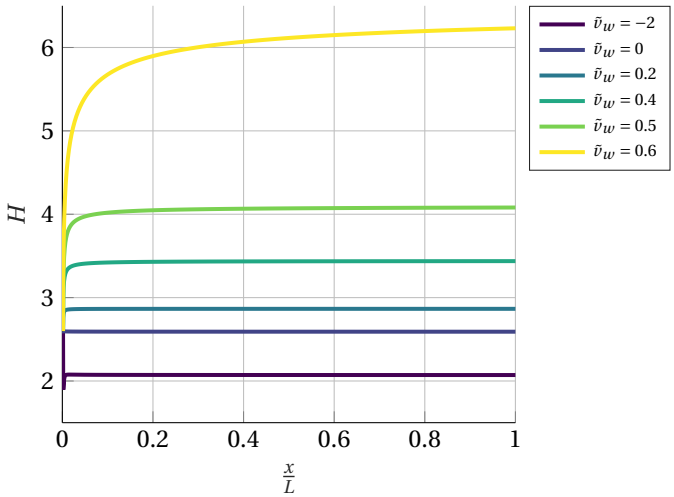

Figure 4.7: Development of shape factor along plate for same values of the suction-blowing parameter as in Fig. 4.5, indicating that solutions trend towards self-similarity

continuous suction applied to a straight wing, and Sec. 4.2.3 concludes with slot suction applied to a swept wing. Furthermore, the validation case from Sec. 4.2.1 contains results for boundary layer stability, which is used to validate the stability solver in Sec. 4.2.4. The stability solver was also tested with a swept wing in Sec. 4.2.5, using the case from Sec. 4.2.3.

4.2.1. Boundary Layer Solver: Flat Plate with Suction

Suction through a short perforated strip on a flat plate was studied in [21]. The experimental study involves both boundary layer development and transition locations for various suction rates, applied between $\frac{x}{c} = 0.291$ and $\frac{x}{c} = 0.322$. The pressure distribution over the flat plate is shown in Fig. 4.9, which was used to reproduce the boundary layer characteristics. The development of the boundary layer displacement thickness is provided for various suction rates, as shown in Fig. 4.10.

The conditions from Figs. 4.9 and 4.10 were reproduced within the modified boundary layer solver, resulting in Fig. 4.11. The agreement with the experimental data is good. Especially the theoretical results from Fig. 4.10 are matched closely by the boundary layer solver, with only minor differences. For example, the 'bump' in δ^* near $\frac{x}{c} = 0.2$ is more pronounced in case of the present results, but this could be due to the interpolation of the pressure distribution from Fig. 4.9. The excellent agreement with the reference data

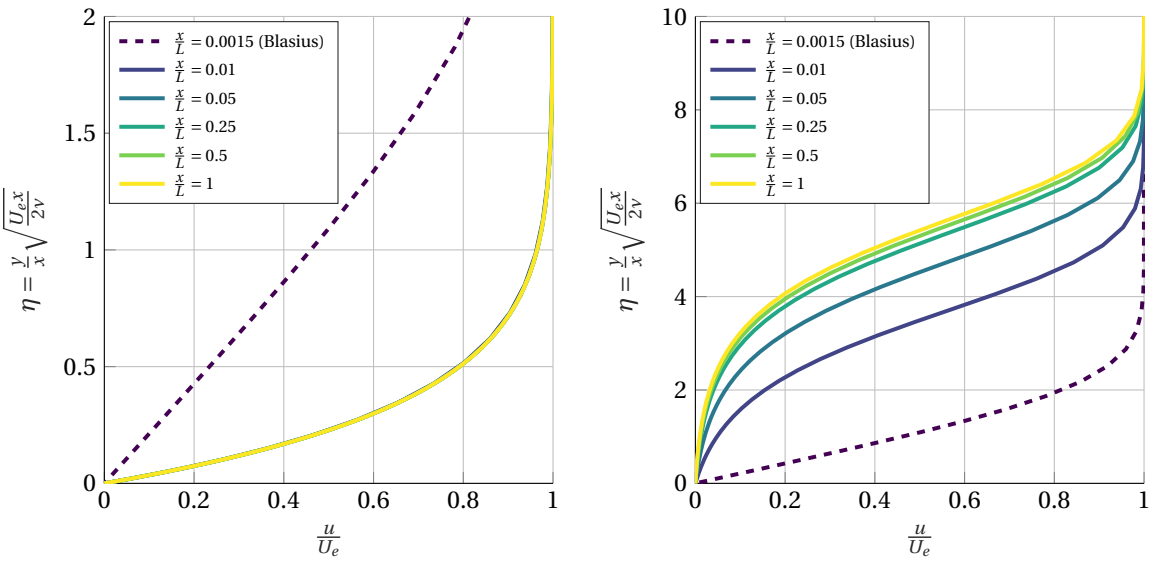

(a) $\tilde{v}_w = -2$ (b) $\tilde{v}_w = 0.6$

Figure 4.8: Development of velocity profiles along the plate, indicating that self-similarity is reached more slowly with blowing

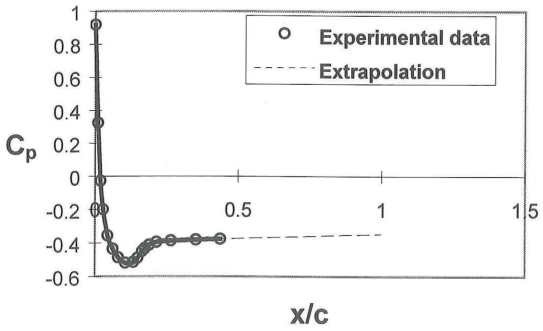

Figure 4.9: Experimental pressure distribution over flat plate [21]

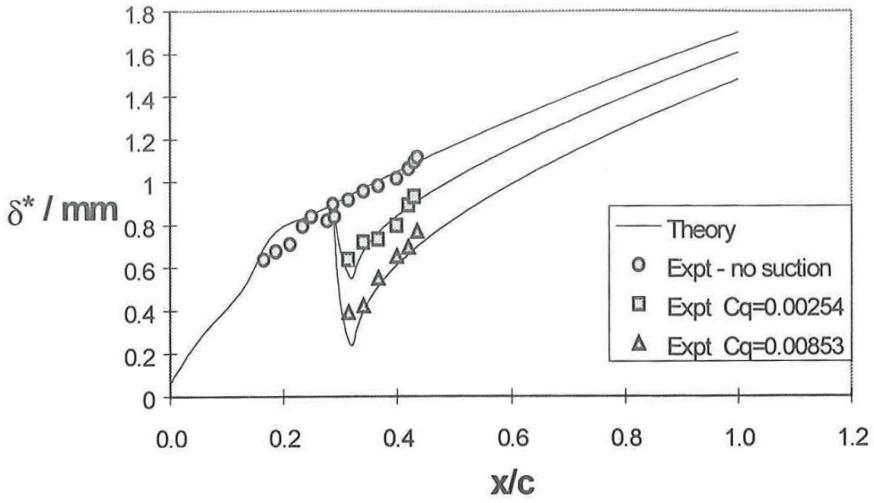

Figure 4.10: Experimental and theoretical development of displacement thickness over flat plate at $Re_c = 2.47 \cdot 10^6$ [21]

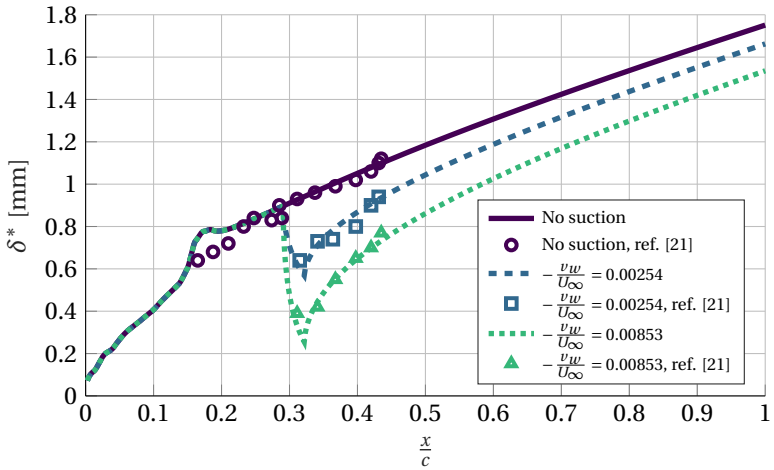

Figure 4.11: Numerical development of displacement thickness over flat plate at $Re_c = 2.47 \cdot 10^6$, compared to reference data from [21]

validates the modified solver for this case.

4.2.2. Boundary Layer Solver: Unswept Wing with Continuous Suction

An extensive wind tunnel investigation of continuous suction on an unswept wing was performed in [75] by van Ingen. Experiments were performed in the low turbulence tunnel at TU Delft. The airfoil was a NACA 64_2A215 where suction was applied between 30% and 90% of the chord.

There are two main parts within the experimental results. The first part consists of detailed experimental boundary layer characteristics for a tabulated velocity distribution and suction distribution. The boundary layer characteristics include profiles at various chordwise locations and the development of integral properties, shown in Fig. 4.12. The second part of the experimental results consists of measured transition locations for various suction distributions. No boundary layer properties are provided, so these results are more suitable to test the stability solver with suction, and may be reserved for future work.

The first set of results are especially useful to validate the boundary layer solver with suction. The tabulated velocity and suction distributions are shown graphically in Fig. 4.13. Experiments were performed at $Re_c = 2.75 \cdot 10^6$ [75]. Combined with a chord length of 1.35 m, the freestream velocity and kinematic viscosity were selected in the numerical tool such that they satisfy the experimental Reynolds number.

The numerical results are shown in Fig. 4.14, consisting of the boundary layer integral properties in Fig. 4.14a and the boundary layer velocity profiles in Fig. 4.14b. The experimental results from [75] are shown for comparison. The first observation is that laminar separation is predicted to be at $\frac{s}{c} = 0.895$ in the present results, while the reference states $\frac{s}{c} = 0.89$ [75], indicating good agreement. The boundary layer integral properties follow the experimental trend well, both before the application of suction and at the start of the suction region. Towards the trailing edge, the integral properties are slightly underestimated. The numerical results from Fig. 4.14a also match well with the computed results from Fig. 4.12. For the velocity profiles from Fig. 4.14b, the numerical results are close to the experimental results initially, but start to deviate towards the trailing edge. This corresponds to the behavior observed for the integral properties. Still, the present numerical results indicate good agreement with the experimental results, validating the modified boundary layer solver for two-dimensional cases involving suction.

4.2.3. Boundary Layer Solver: Swept Wing with Slot Suction

Having validated the modified boundary layer solver for two-dimensional cases, the final component to be tested is the effect of wing sweep, which is addressed in the final validation case. Wind tunnel tests of a swept wing with slot suction are documented in [46]. The wing had a modified NACA 66-012 section in flight direction and had a sweep angle of 30 degrees with a constant chord length. This is an extremely relevant validation case, because it is closely related to the application for which the tool is intended: an infinite swept wing with

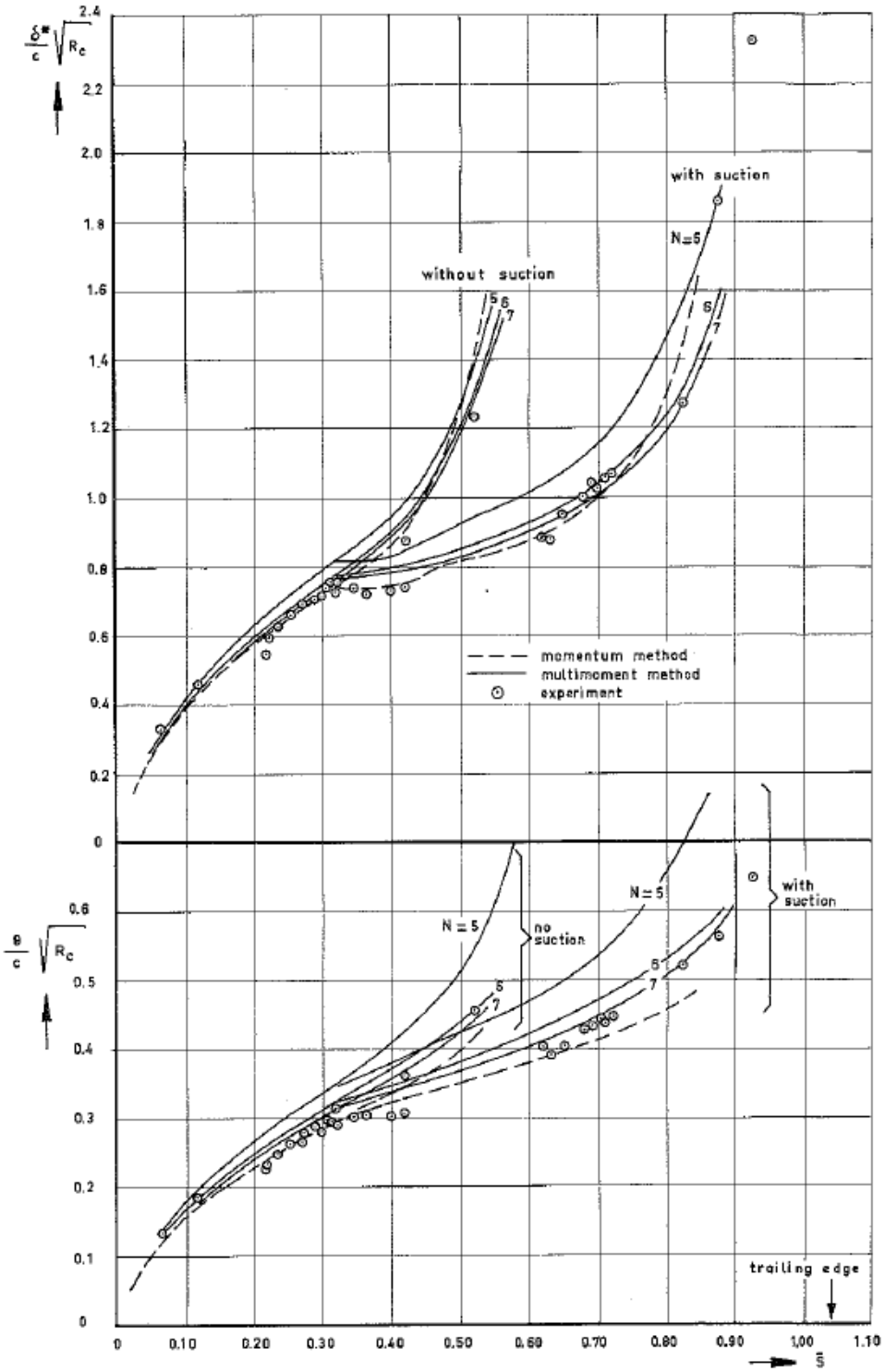

Figure 4.12: Experimental development of displacement thickness and momentum thickness on a wing with suction [75]

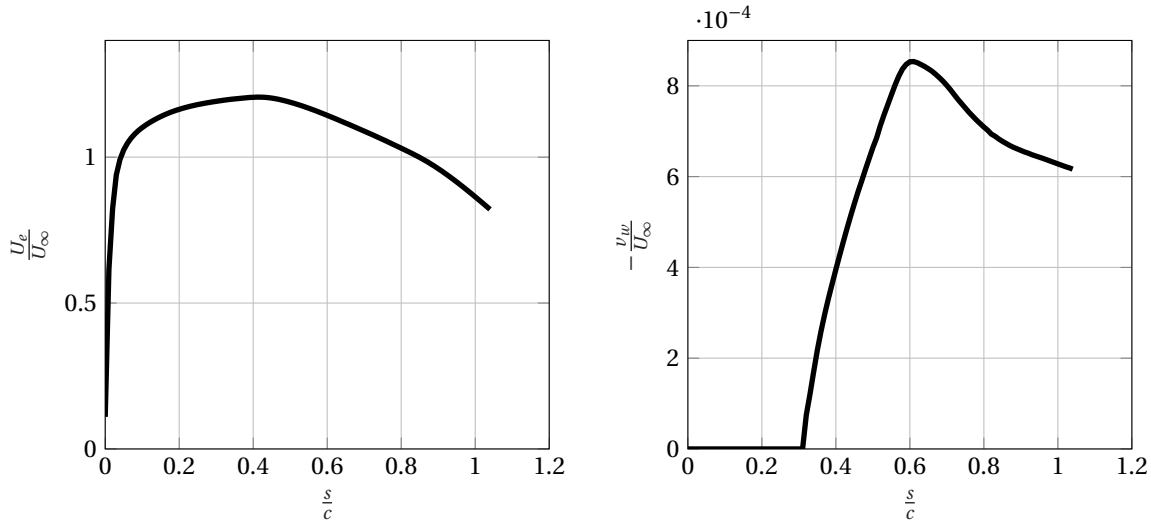

(a) Velocity distribution

(b) Suction distribution

Figure 4.13: Velocity and suction distributions used for determining boundary layer characteristics in [75]

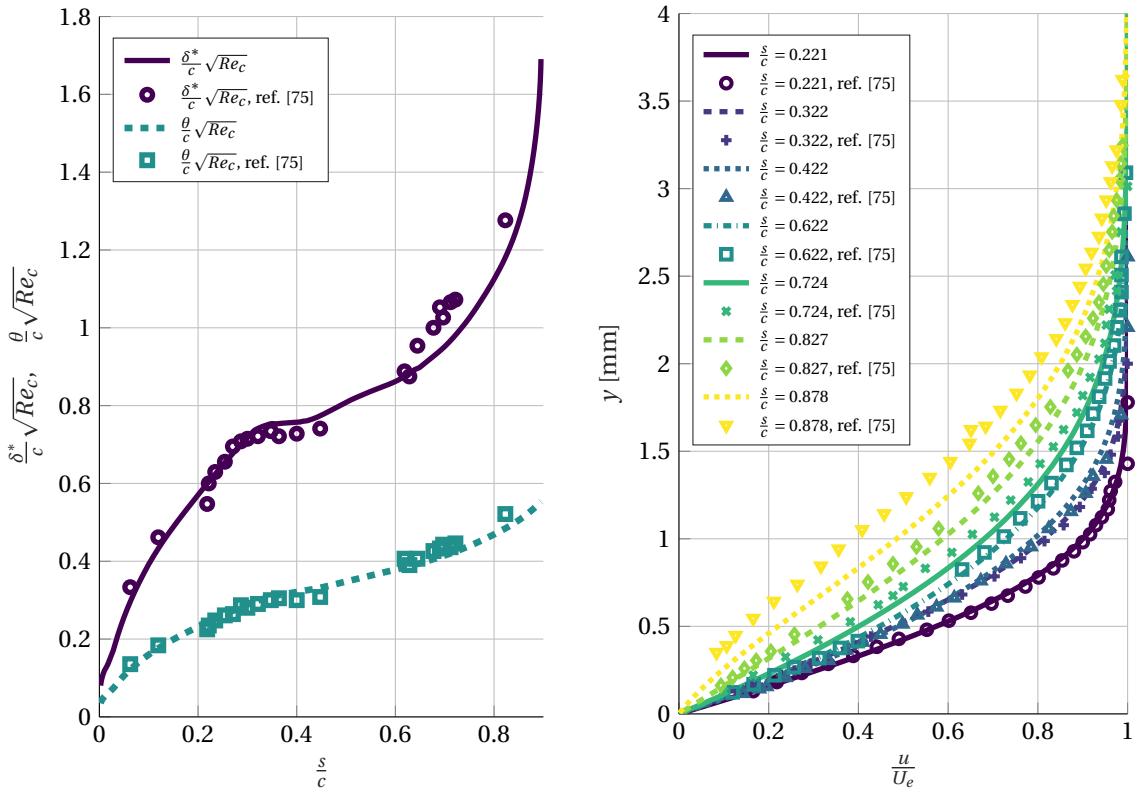

(a) Boundary layer integral properties

(b) Boundary layer velocity profiles

Figure 4.14: Numerical boundary layer characteristics compared to experimental data from [75]

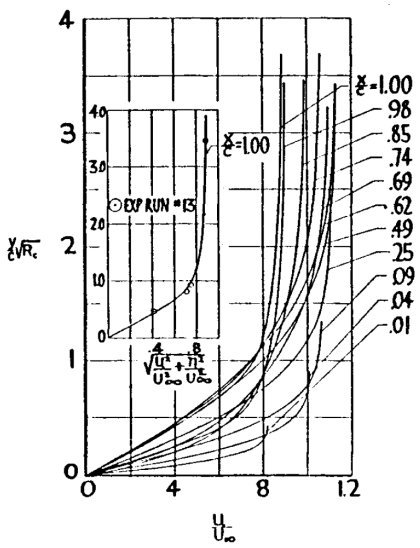

(a) Streamwise boundary layer profiles (u_s) at various chordwise positions. Inset: experimental boundary layer profile at trailing edge

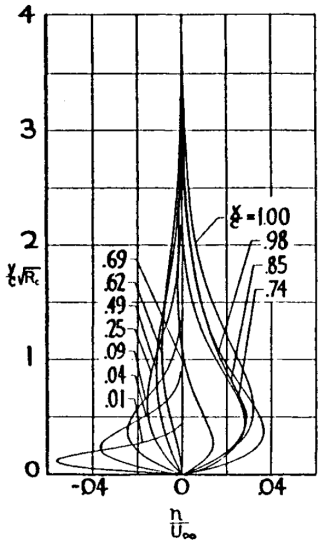

(b) Cross flow boundary layer profiles (w_s) at various chordwise positions

Figure 4.15: Theoretical boundary layer profiles for experimental test of swept wing with suction [46]

suction. In addition, the boundary layer was more unstable for CF disturbances than for TS disturbances, so that the effect of cross flow can be studied. The only difference with typical HLFC is that slot suction is used instead of continuous suction, but [46] conveniently presents suction rates converted to equivalent area suction rates, making it suitable for the numerical tool. The wind tunnel tests were conducted in multiple tunnels, one of which was the Ames 12-foot tunnel, known for having a low freestream turbulence intensity, namely $\frac{u'}{U_\infty} \leq 0.01\%$ [24].

Suction was applied over nearly the entire airfoil in order to obtain full-chord laminar flow. A theoretical and experimental investigation was performed, of which the experiments are of most interest. Most of the presented experimental results are related to drag coefficients, but some boundary layer characteristics are also provided. For one of the experimental runs, the theoretical boundary layer profiles were calculated. These are presented in Fig. 4.15. These correspond to the experiment in the Ames tunnel, for which the experimentally determined boundary layer profile at the trailing edge is also provided in the same figure.

The velocity distribution over the swept model was reproduced by using XFOIL with the airfoil coordinates perpendicular to the leading edge, as presented in [46]. The velocity distribution used to compute the results from Fig. 4.15 is shown in Fig. 4.16a, while the results obtained in the present research are shown in Fig. 4.16b. Some differences between the two results can be observed, namely a stronger acceleration just after the leading edge, in case of the numerical results from Fig. 4.16b. Furthermore, these results show a minor 'bump' in the pressure gradient near $\frac{x}{c} = 0.6$, with flow deceleration starting from this location. Meanwhile, this deceleration regions starts at approximately $\frac{x}{c} = 0.63$ for the reference solution from Fig. 4.16a. The differences are highlighted here because they affect the validation of the numerical results, which will be discussed later. However, it is believed the numerical results from Fig. 4.16b are physically representative, because the experimentally observed pressure gradient presented in [46] also features the 'bump' near $\frac{x}{c} = 0.6$.

Care must be taken to interpret the results from [46] in the correct reference frame. For instance, U_∞ is used interchangeably to represent the total freestream velocity—referred to as Q_∞ in the present document—or the streamwise component of the freestream velocity—referred to as U_∞ here and in Fig. 3.2. Figure 4.16 represents the velocity distributions normal to the leading edge, and are therefore scaled with U_∞. For other data from [46], whenever U_∞ is used as the velocity scale, it should be interpreted as Q_∞. The numerical results obtained in the present research adhere to the sign convention from Fig. 3.2. As such, the Reynolds number at which the experiments were performed was $Re_c = \frac{Q_\infty c}{\nu} = 23.7 \cdot 10^6$ [46]. While Re_c is defined us-

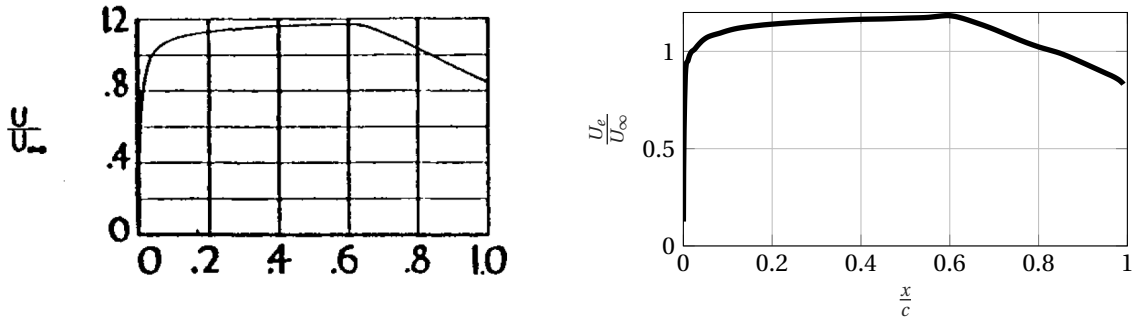

(a) Potential flow solution used in [46]

(b) Numerical results based on airfoil coordinates

Figure 4.16: Tangential flow velocity distributions, perpendicular to leading edge, over the swept wing from [46]

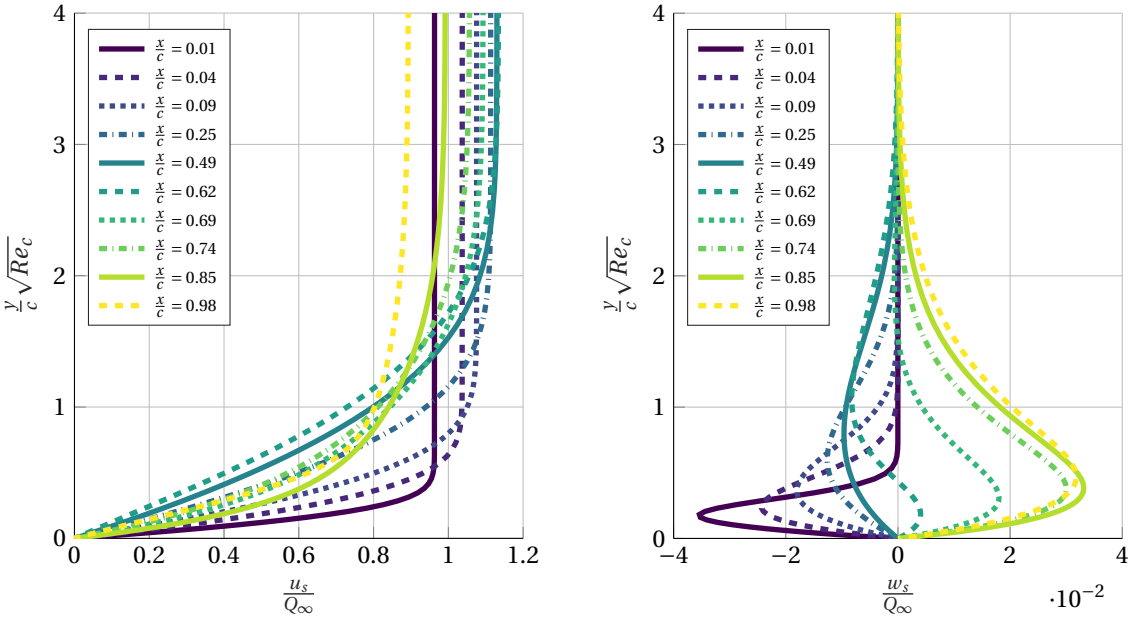

(a) Streamwise boundary layer profiles (u_s)

(b) Cross flow boundary layer profiles (w_s)

Figure 4.17: Numerical boundary layer profiles on swept wing corresponding to experimental data from Fig. 4.15

ing the chord length in the freestream direction (7 feet [46]), the boundary layer equations are solved in the x-direction perpendicular to the leading edge. Therefore, the chord length in perpendicular direction—with a value of 72.96 inches [46]—was used for the solution domain of the boundary layer.

The numerical results obtained with the modified boundary layer solver are shown in Fig. 4.17. Note that a solution at $\frac{x}{c} = 1$ could not be obtained, because laminar separation was predicted at $\frac{x}{c} = 0.991$. Comparing the numerical results to the reference data from Fig. 4.15 shows a good general agreement, with the numerical profiles reaching steady state values at approximately the same height above the wall as the reference. The velocity profiles are largely similar, with a few exceptions. Starting with the streamwise velocity, u_s at $\frac{x}{c} = 0.01$ and $\frac{x}{c} = 0.04$ is higher in Fig. 4.17a than in Fig. 4.15a. This is due to the difference in the velocity distribution that was used to obtain the data sets. Illustrated in Fig. 4.16, there is a stronger acceleration just after the leading edge in case of the numerical solution. Therefore, u_s reaches a higher value in this region compared to the reference. However, by $\frac{x}{c} = 0.09$, the magnitude of u_s is comparable between Figs. 4.15a and 4.17a.

This difference in the velocity distribution also accounts for the variance in the boundary layer cross flow profiles near the leading edge. As Fig. 4.17b shows, the magnitude of w_s at $\frac{x}{c} = 0.01$ and $\frac{x}{c} = 0.04$ is smaller than for the reference in Fig. 4.15b. According to Sec. 2.3.2, cross flow originates from a pressure gradient.

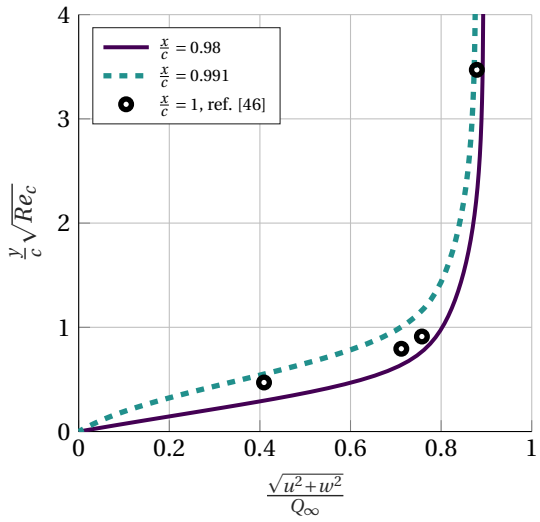

Figure 4.18: Comparison of numerical results with experimental boundary layer profile near trailing edge of swept wing

Because of the stronger pressure gradient for the numerical results, the CF magnitude is large initially, but quickly reduces once the pressure gradient becomes more gradual. In fact, this happens for the numerical results for $\frac{x}{c} = 0.01$ and $\frac{x}{c} = 0.04$, where the flow direction has already curved away from the attachment line and into the streamwise direction. Meanwhile, for the reference data based on Fig. 4.16a, the flow acceleration behind the leading edge is more gradual, leading to stronger magnitude of w_s at $\frac{x}{c} = 0.01$ and $\frac{x}{c} = 0.04$. However, the numerical results become similar to the reference data from $\frac{x}{c} = 0.09$ and onward.

The biggest difference between Figs. 4.17b and 4.15b occurs at $\frac{x}{c} = 0.62$. Here it is observed that cross flow reversal has started for the numerical data, while the reference data is on the verge of reversal. This derives from the difference in the velocity distributions highlighted by Fig. 4.16. In fact, flow deceleration starts around $\frac{x}{c} = 0.63$ for the reference data, which implies CF reversal does not start at $\frac{x}{c} = 0.62$, where the data is presented. On the other hand, flow deceleration starts at $\frac{x}{c} = 0.6$ for the numerical data, upstream of the measurement location, implying CF reversal has set in.

A final comparison is made between the numerical results and the experimentally determined velocity profile shown in the inset in Fig. 4.15a. The experimental profile was obtained at $\frac{x}{c} = 1$, but the numerical solution could only be computed up to laminar separation at $\frac{x}{c} = 0.991$. Therefore, Fig. 4.18 compares the experimental result to the numerical profiles at $\frac{x}{c} = 0.98$ and at laminar separation. In fact, the numerical results are close to the reference data, with the profile at laminar separation just above the reference. Accounting for some uncertainty in the measurement location of the experimental profile, the numerical results are credible.

In conclusion, the application of the modified boundary layer solver to a three-dimensional validation case has shown good general agreement. Minor deviations were observed, which could be attributed to different input data. Combining these observations with the previous validation cases, in which satisfactory agreement with reference data was obtained for increasingly complex situations, all essential components of a three-dimensional boundary layer with suction were validated. Therefore, the modified boundary layer solver is considered wholly validated for use with suction on infinite swept wings.

4.2.4. Stability Solver: Flat Plate with Suction

Besides the boundary layer properties used to validate the boundary layer solver in Sec. 4.2.1, the study from [21] also contains an analysis of boundary layer stability. In fact, N-curves are provided for a case with and without suction, as shown in Fig. 4.19. Since the e^N-method based on linear stability theory was used in [21], a direct comparison can be made with the transition prediction tool described in Sec. 3.4.2.

Both cases were reproduced with the stability solver, including the modifications described in Sec. 3.5.3. The results are shown in Fig. 4.20. Without suction, the results obtained with the stability solver are com-

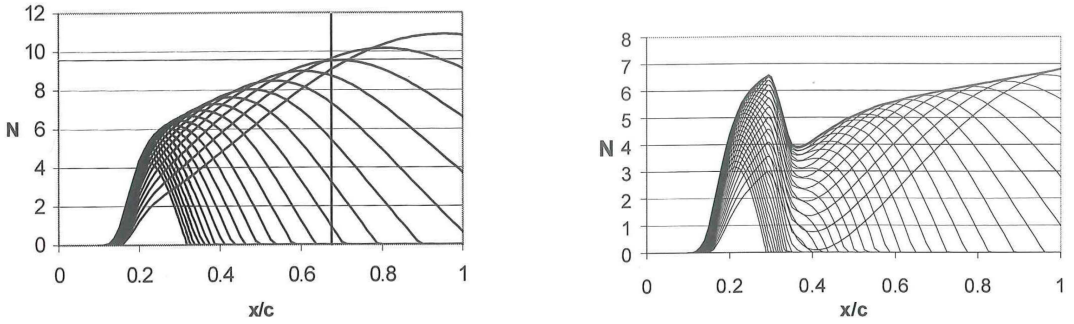

(a) Without suction

(b) With suction: $-\frac{v_w}{U_\infty} = 0.00303$

Figure 4.19: N-curves on flat plate at $Re_c = 2.04 \cdot 10^6$ evaluated with linear stability theory [21]

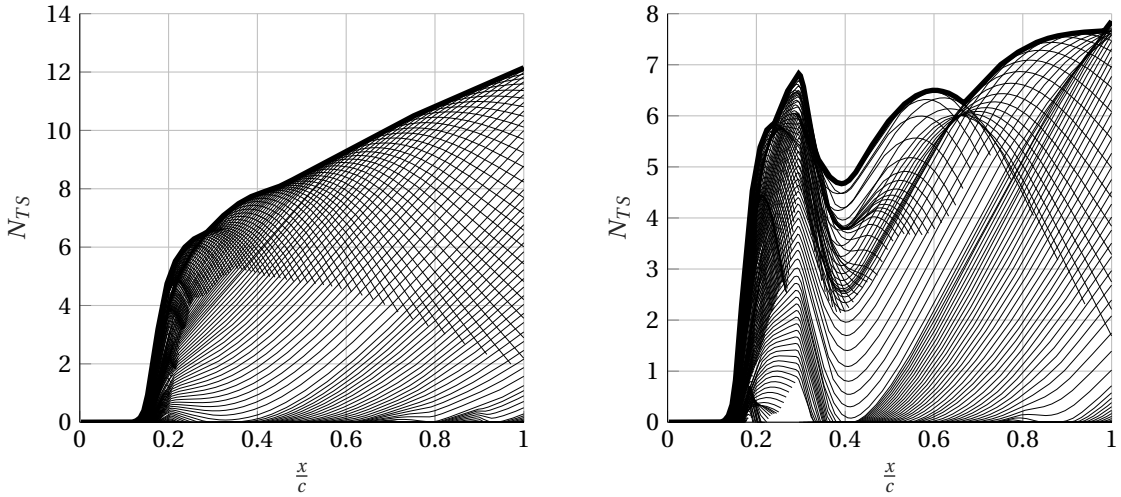

(a) Without suction

(b) With suction

Figure 4.20: N-curves on flat plate at $Re_c = 2.04 \cdot 10^6$ evaluated with transition prediction tool

parable to the reference. The good agreement is not surprising, as the original stability solver was already validated. For example, both indicate an N-factor of about 10 at $\frac{x}{c} = 0.7$. Beyond this point, the N-factor is higher than the reference data, because more modes are included in the present analysis.

The numerical results with suction are presented in Fig. 4.20b. In the first place, the N-curves pass through the unstable region, which indicates that the modifications described in Sec. 3.5.3 meet their goal. The comparison with Fig. 4.19b shows good agreement initially, with N reaching values just under 7 before the application of suction. Downstream of the suction strip, there is a kind of 'bump' in the N-factor, along with an otherwise similar trend as the reference. Again, the occurrence of this bump is believed to be due to the increased number of modes used with the present work. However, the overall agreement with the reference data is satisfactory, and the modified stability solver has therefore been validated for this case.

4.2.5. Stability Solver: Swept Wing with Slot Suction

Even though no modifications appeared necessary for the combination of the stability solver and a swept wing with suction, it is important to check its behavior because CF is an inherent element of transonic aircraft. The swept-wing case from Sec. 4.2.3 was used here again, because the numerical boundary layer solution proved accurate. While the original report does not contain any information about boundary layer stability, knowing that full-chord laminar flow was obtained is useful because it can give an indication of the critical N-factor on a swept wing with suction. In addition, this case was also used to assess the modifications to the TS preprocessing, although the TS amplification was mild.

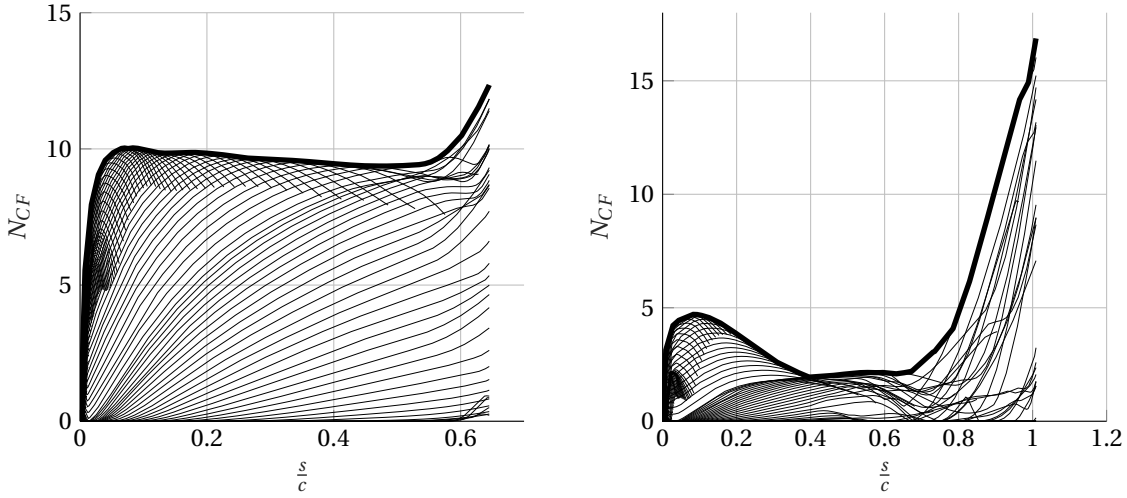

(a) Without suction

(b) With suction

Figure 4.21: Cross flow N-curves on swept wing evaluated with transition prediction tool

Focusing on the CF instability first, its amplification was evaluated with and without suction, so that the effect of suction could be observed. The resulting N-curves in Fig. 4.21 show a dramatic influence of suction. A first observation is that laminar separation occurs further upstream without suction. Furthermore, the strong CF amplification near the leading edge—induced by the rapid flow acceleration—is effectively controlled with the application of suction. Then, CF amplification stagnates in the region of small pressure gradient, according to expectation. The pressure gradient is stronger in the region of pressure recovery, starting around $\frac{s}{c} = 0.6$, which causes further CF amplification. In fact, "severe" cross flow was observed on the rear of the airfoil for this reason [46, p. 1010]. Even with the strong suction rate applied there, significant CF growth is observed in Fig. 4.21b. Given that N_{CF} rises to around 10 without suction, it is likely that transition would have occurred within the first 10% of the chord. With suction, full-chord laminar flow was obtained [46], although N_{CF} seems almost prohibitively large. Therefore, further research into the critical N-factor with suction remains necessary.

Even if transition had not occurred without suction due to cross flow, the TS instabilities would have likely induced transition, as evident from Fig. 4.22a. On the other hand, the strong suction rate required to control CF was more than sufficient to provide stability against TS disturbances [46]. This is confirmed by Fig. 4.22b.

Given that the boundary layer with suction is very stable with respect to TS disturbances, this could prove problematic for the original implementation of the preprocessing of the stability solver. The estimated neutral curves would likely be too restrictive to include all unstable frequencies. In fact, this is exactly what happened, as illustrated by Fig. 4.23a. There is only a slight unstable region at the very end of the domain and a narrow unstable region a little more upstream. However, the grid limits should have been larger to enclose all unstable frequencies. Using the algorithm described in Sec. 3.5.3 as part of the modified preprocessor, the shape factor and the gradient of the velocity profile were adjusted as in Fig. 4.24, such that the estimated neutral curves became further apart, as shown in Fig. 4.23b. These neutral curves yield a suitable grid, as shown in Fig. 4.25. It can be seen that the grid does not start until the solution is expected to become unstable, according to the estimated critical Reynolds number. Furthermore, the fine grid is only evaluated near the unstable frequencies. Therefore, the modified preprocessor behaves as intended.

While no reference data about the stability properties of the boundary layer was available, the computed stability characteristics for CF agreed with the expected behavior, both with and without suction. Hence, the stability solver has been validated for cases combining wing sweep and suction. In addition, the analysis of the TS instability demonstrated that the modified preprocessor produces appropriate grid limits in case of suction. Combined with the satisfactory results of Sec. 4.2.4, it is expected that the modifications will apply in most general cases. However, analysis with additional cases would be helpful to further fine-tune the algorithm. In exceptional cases, manual manipulation of the grid limits may be required.

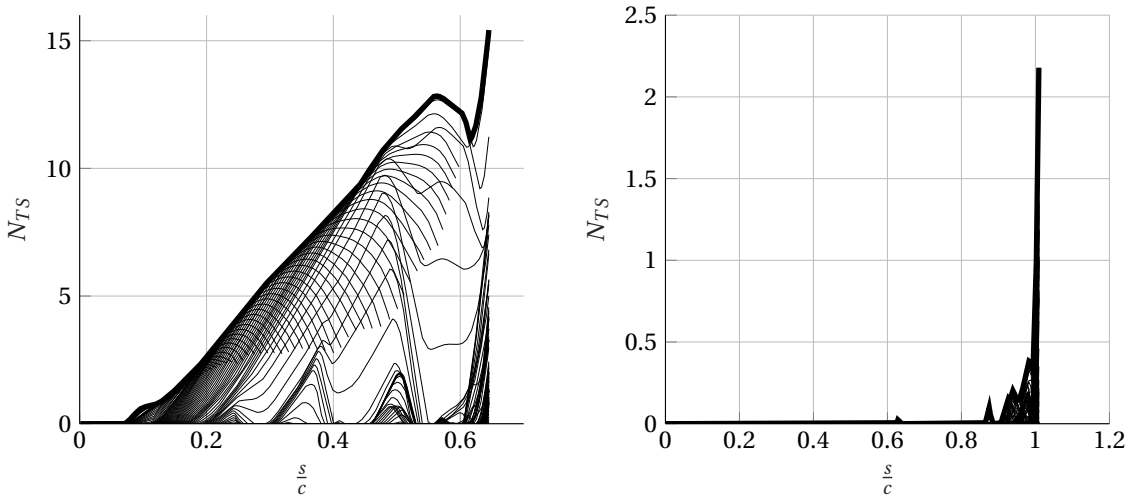

(a) Without suction

(b) With suction

Figure 4.22: Streamwise N-curves on swept wing evaluated with transition prediction tool

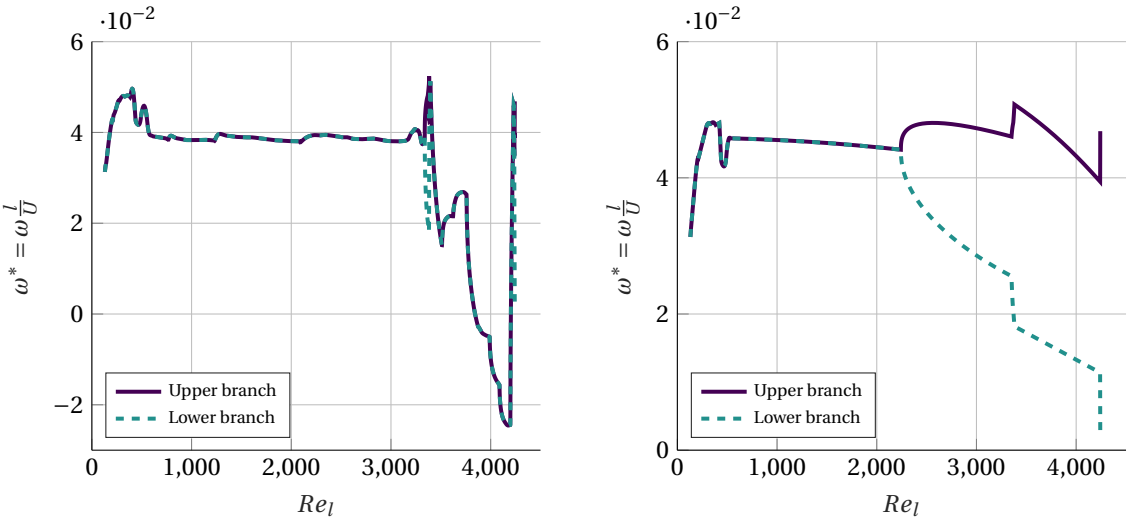

(a) Original

(b) Modified

Figure 4.23: Original and modified neutral curves for TS instability on swept wing

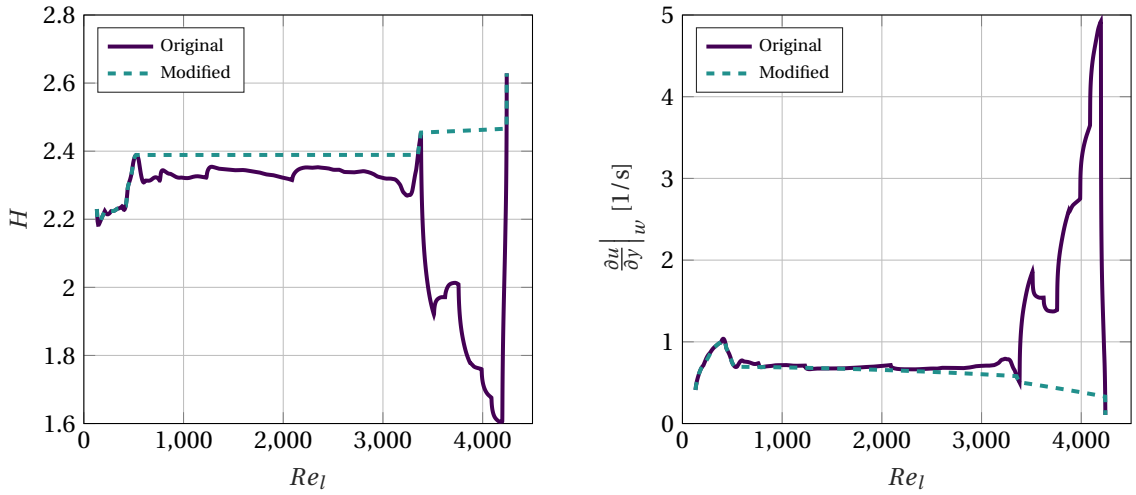

(a) Shape factor

(b) Gradient of velocity profile at the wall

Figure 4.24: Original and modified boundary layer properties to remove effect of suction for estimating neutral curves for TS instability on swept wing

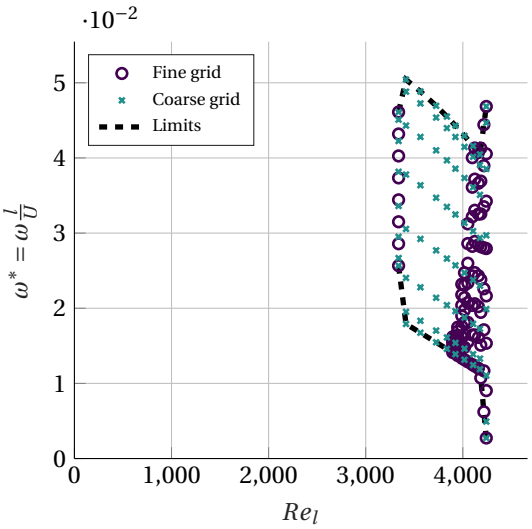

Figure 4.25: Grid limits for TS instability on swept wing obtained with modified stability preprocessing

5

Characterizing the Pressure Losses across Suction-Type HLFC Components

Chapter 2 introduced HLFC and reviewed its practical implementation, from which suction through a perforated surface emerged as the most feasible candidate. Suction requirements vary by application. In order to design a suction surface for generic applications, the governing parameters—both in terms of geometry and flow—for the pressure losses across a suction surface should be determined. Knowing these, the pressure losses across perforated surfaces can be characterized parametrically, enabling a convenient way of designing generic suction-type HLFC components.

Section 5.1 introduces the design considerations regarding the pressure losses associated to suction-type HLFC components. Then, Sec. 5.2 investigates the parameters that govern these losses. Section 5.3 assesses the typical values for these parameters for HLFC systems. Using these parameters, Sec. 5.4 describes the model with which the experiments will be analyzed. Afterwards, Sec. 5.5 discusses how the critical suction limit may be estimated. Finally, Sec. 5.6 covers how to reduce the power required to operate a suction system.

5.1. Pressure Losses across Suction-Type HLFC Components

The performance of a suction-type HLFC component is governed by the pressure losses through the system. A suction system consists of a perforated suction surface, but also includes internal ducting and possibly a pump, all of which introduce losses. These losses may be due to losses of kinetic energy, throttling and mixing, flow separation, or duct wall friction [45]. This chapter focuses primarily on the pressure losses across to the suction surface, since that is a common component for all HLFC systems and typically has comparable properties (Sec. 5.3), whereas the ducting system is specific to the application.

An excellent review of the design considerations for suction surfaces is given by Gregory [26]. A first point is how to obtain the desired suction distribution on a wing with a varying pressure distribution. With a single suction pump, a variable suction distribution can be obtained by varying the porosity along the surface. Another solution is to use multiple or multi-stage pumps, but this can be imagined to be heavy. Therefore, the tendency of simplified HLFC systems (Secs. 2.8.3 and 2.9) has been to use a single pump.

Because a variable porosity along the suction surface complicates manufacturing, the desired suction distribution with a single pump may instead be obtained by creating throttling holes below the surface [26]. These divide the suction surface into smaller cells, where the pressure—and thus the suction rate—is controlled by throttling holes. These holes are larger and less numerous than on the perforated surface, which simplifies manufacturing. In fact, such a solution is used on the simplified HLFC system proposed in Fig. 2.16.

A second important issue of suction surfaces is preventing outflow. Outflow occurs when the pressure on the outside of the suction sheet is lower than on the inside. A reverse flow will start to develop, which can promote transition. Preventing outflow implies that the internal pressure of the suction system should be lower than the lowest external pressure on the suction surface. The lower the internal pressure is, the higher

the sink drag or pump losses will be, depending on whether the system is passive or active. Thus, suction should be avoided in areas of very low pressure [14, 71]. As a result, applying high amounts of suction in high-pressure areas may be more efficient than applying less suction in low-pressure areas [14].

An important parameter for suction holes in a perforated sheet is their aspect ratio. In other words, the length-to-diameter ratio, or sheet thickness-to-diameter ratio ($\frac{t}{d}$), is a governing parameter. Being a sudden contraction, the entrance of a suction hole features flow separation around the corners of the hole. This creates a recirculation region on the wall of the hole, which narrows the core jet flow. The 'vena contracta' is the point at which the diameter of the jet is most reduced by the recirculation region and where the flow velocity is highest [60]. For thin sheets, having $\frac{t}{d} < 0.5$, the separated flow is unlikely to reattach [40]. In this case, the vena contracta is downstream of the sheet. Conversely, for thick sheets, the flow reattaches inside the hole, putting the vena contracta inside the hole [40]. The lower limit for reattachment is between $\frac{t}{d}$ of 1–2 [23, 27, 40]. The effect of the parameter $\frac{t}{d}$ on the flow through a perforation is likely why MacManus and Eaton state that the hole aspect ratio is an important similarity parameter to preserve [37].

An additional factor affecting the performance of suction sheets is the presence of a tangential flow, as shown in Fig. 2.11b. Without a tangential flow over the suction sheet, as illustrated by Fig. 5.1, there is a certain pressure loss associated to the suction through that sheet. A tangential flow creates a blocking effect for transpiration [20]. This creates an additional pressure loss that must be overcome. This effect only occurs for suction but not for blowing [20].

5.2. Similarity Parameters for Flow across a Perforated Surface

For a successful design, it is important to get a good estimate of the pressure losses across porous surfaces [59]. Thus, it is desired to identify the similarity parameters, related either to the geometry or the flow properties, that govern this pressure drop. These parameters should be nondimensional, such that the influence of units is taken out, thereby making them applicable to arbitrary configurations. The present research investigates to what extent scaled suction surfaces can be used to predict the performance of typical HLFC systems. This scalability will be judged according to the degree with which a model using the governing parameters can predict the pressure losses of generic perforated sheets.

An introduction to the governing parameters of the performance of suction surfaces is given in [26]. The parameter of primary interest is the pressure drop across the sheet, which can be made nondimensional by dividing it by a dynamic pressure, giving the 'pressure drop coefficient' [26]. The dynamic pressure is based on a reference velocity, which will be discussed later. Additionally, a Reynolds number characterizes the viscous effects in the suction holes [26]. Furthermore, the Mach number may play an important role [26].

Geometric properties include the porosity of the perforated surface, the hole diameter (d), and the sheet thickness (t) [26]. The porosity may be represented by the open area ratio (β), which is the ratio of the perforated area to the total area of the sheet [26]. This definition is convenient because it can be applied to any hole pattern. β is already nondimensional, but the hole diameter and sheet thickness are not. Combining them yields the aspect ratio of the holes, $\frac{t}{d}$. In addition, d serves as the length scale in the Reynolds number.

The tangential flow over a suction surface, shown in Fig. 2.11b, introduces an additional set of nondimensional parameters. These were identified in the excellent similarity study by MacManus et al. [38]. In this case, a boundary layer is present, which leads to the following additional parameters [38]: the ratio of hole diameter to boundary layer displacement thickness, $\frac{d}{\delta^*}$; the ratio of hole velocity (v_h) to the edge velocity (U_e), $\frac{v_h}{U_e}$; the Reynolds number based on the displacement thickness, Re_{δ^*}; and the unit Reynolds number, Re'. The unit Reynolds number may also be replaced by the Reynolds number based on another reference length. The parameters mentioned earlier, $\frac{t}{d}$ and Re_d, the Reynolds number based on hole diameter, were also included in [38]. The parameter $\frac{d}{\delta^*}$ is one of the most important for the flow through a suction hole, which is why the similarity of this parameter was taken as the highest priority in [38].

Another characterizing parameter for suction systems is the suction coefficient. The suction coefficient is a measure of the amount of air that is sucked through the surface relative to some reference quantity of the main flow. Usually, the suction coefficient is represented as a ratio of velocity or momentum.

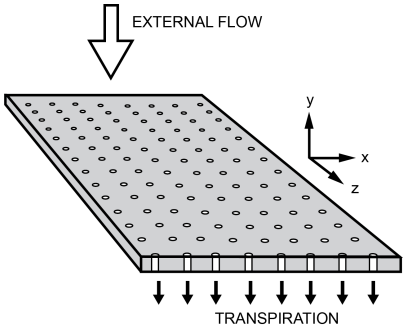

Figure 5.1: Schematic of transpiration through a perforated sheet. External flow is perpendicular to the perforated surface

The next question is which reference velocity should be used to define the pressure drop coefficient and the hole Reynolds number. Gregory indicates the mean transpiration velocity on the suction surface, v_w [26]. However, the hole velocity (v_h) was used in the present research, because it gives a better collapse of the experimental results. For the hole Reynolds number, the mean transpiration velocity is used in [26], whereas the hole velocity is used in [38]. In this case, using the hole velocity is the appropriate choice, because it describes the viscous flow though the suction hole. Consequently, the pressure drop coefficient may be defined as in Eq. (5.1) and the hole Reynolds number may be defined as in Eq. (5.2).

$$C_{\Delta p} = \frac{\Delta p}{\frac{1}{2}\rho v_h^2} \tag{5.1}$$

$$Re_d = \frac{\rho v_h d}{\mu} = \frac{v_h d}{\nu} \tag{5.2}$$

As stated in Sec. 5.1, the pressure drop across a perforated surface may be split up into two components: the inherent pressure loss across the perforated surface, and the additional pressure loss when a tangential flow is present. The effect of tangential flow may be studied with an experimental setup similar to the setup described in [67], where a wind tunnel model with a perforated skin was used, comparable to Fig. 2.11b. Instead, this study focuses on the inherent pressure loss across a perforated sheet. To that end, a test setup was constructed where the effects of tangential flow can be excluded, like in Fig. 5.1. For such a setup, a perforated sheet is placed perpendicular to the flow through a pipe, so that the freestream flow is aligned with the axis of the perforations. Experiments using this type of setup have been performed in [67] and [80].

This experimental setup without tangential flow allows some similarity parameters to be excluded, such as $\frac{d}{\delta^*}$, $\frac{v_h}{U_e}$, and Re_{δ^*}. The suction coefficient is not relevant anymore, because all the freestream air must pass through the perforations, instead of the typical, small amount for HLFC. This enables a more detailed analysis of the influence of the remaining similarity parameters on the pressure losses across perforated sheets. In addition, while the tangential flow over suction surfaces varies depending on the application, all suction surfaces feature a perpendicular flow, giving the present study a wide range of applicability. The remaining similarity parameters for perpendicular flow through a perforated sheet are Re_d, β, and $\frac{t}{d}$. These three parameters, along with $C_{\Delta p}$, were also used in [27, 70], justifying their applicability.

Of these three similarity parameters, the open area ratio, β, was found to be the most important [19]. The sheet thickness ($\frac{t}{d}$) and the shape of the holes were found much less important [19]. It was observed in [19, p. 4] that there was "no appreciable effect on the results when the sheet was tested in the reverse direction." Because these tests were performed at $\frac{t}{d} < 1$, the flow inside the holes would not have reattached. Therefore, the influence of the shape of the hole would have been negligible. For typical HLFC components, however, the holes are usually laser-drilled, which produces tapered holes. This implies that the pressure losses depend on the orientation of the sheet, as was observed in [80]. Therefore, the perforated sheets should be tested in both directions, to account for any deviations in the geometry. Furthermore, it may be possible that the pressure drop coefficient is a unique function of $Re_d \cdot \frac{d}{t}$, in order to account for the effect of sheet thickness [14, 26].

5.3. Evaluating the Similarity Parameters for Typical HLFC Systems

Knowledge of the typical values of the similarity parameters of HLFC systems was used in Sec. 6.5 to design a scaled experiment which still represents real HLFC systems applied onto a transport aircraft, provided that the results are scalable. This section collects the available information about the similarity parameters—β, $\frac{t}{d}$, and Re_d—evaluated on HLFC systems.

The first source of information is a study on the durability of HLFC surfaces performed by Young et al. [80]. They showed that the titanium suction surface outperformed the aluminum and composite surfaces. Therefore, only the properties of the titanium sample are considered here. The porosity of the perforated sheet was about 0.8%, with a hole diameter of approximately 72 μm. Combining this diameter with a sheet thickness of approximately 0.9 mm gives $\frac{t}{d}$ of about 12.5.

The second set of information comes from the LEFT program (Sec. 2.8.1), for which the properties of the suction sheet are provided in [11]. Only geometric properties of the suction surface are available, namely a hole diameter of 0.0025 inches (64 μm), a sheet thickness of 0.025 inches (0.64 mm), and a hole spacing of 0.035 inches (0.89 mm). This results in an open area ratio of 0.4%, and a $\frac{t}{d}$ of 10.

For the HLFC system on the Boeing 757 (Sec. 2.8.2), the properties of the suction surface are available in [6]. The hole diameter and pitch between the holes were variable, with d between 0.0016 and 0.0023 inches (40–60 μm), and the pitch between 0.01 and 0.029 inches (0.25–0.74 mm). This yields β between 0.5% to 2%. The sheet thickness was 0.04 inches (1 mm), resulting in $\frac{t}{d}$ between 16 and 25. In addition, the suction distribution and the cruise flight conditions were provided. With a suction coefficient going up to 0.003, the maximum velocity in the suction holes may be estimated to be around 140 m/s, giving Re_d up to 180.

The study of the flow field induced by a suction hole performed by MacManus et al. in [38] also includes a list of typical values for the similarity parameters of an HLFC system. For example, they state that the ratio of the pitch between the holes and the hole diameter is approximately 10, which yields a β of 0.8%. Furthermore, the typical $\frac{t}{d}$ is around 17. Regarding the flow through the suction holes, the mean velocity in the hole may be 20% of the local streamwise velocity. Using the fact that the Mach number may be as high as 1.4 on a typical transonic wing cruising in standard atmospheric conditions at an altitude near 11 km, a typical hole velocity would be about 80 m/s. For high suction, the hole velocity may be higher. For a single suction hole, it was found that premature transition due to oversuction may start at a hole velocity that is near 60% of the local streamwise velocity [36]. This gives a hole velocity up to 240 m/s for strong suction. The corresponding hole Reynolds number would be around 300. As found in [38], Re_d for typical suction rates is around 100.

Finally, reference [25] states that the typical hole diameter for HLFC systems ranges between 40 and 100 μm. This is in line with the previous references. Information about other parameters is not provided.

The information collected in this section is summarized in Tab. 5.1. The hole diameter is not a similarity parameter because it is dimensional, but it is included to provide an idea of the size of typical HLFC setups.

Table 5.1: Typical values for similarity parameters of HLFC systems

Source	d [μm]	β [%]	$\frac{t}{d}$ [-]	Re_d [-]
Young et al. [80]	72	0.8	12.5	-
LEFT program [11]	64	0.4	10	-
Boeing 757 [6]	40–60	0.5–2	16–25	0–180
MacManus et al. [38]	50	0.8	17	0–100
MacManus and Eaton [36]	-	-	-	0–300
Gerber [25]	40–100	-	-	-
Typical HLFC system	40–100	0.4–2	10–25	0–300

5.4. Pressure Drop Model

The governing similarity parameters for the pressure drop across a perforated sheet were identified in Sec. 5.2. The present section investigates how these parameters are expected to influence the pressure drop. A model will be developed with which the experimental results will be analyzed.

Fundamentally, the pressure loss across a thin perforated sheet is attributed to the sudden contraction and expansion at the entry and exit of the perforation [23]. For a thick perforated sheet, having $\frac{t}{d} > 1$ (Sec. 5.1), friction inside the hole creates an additional contribution to the pressure losses [23]. Both types of pressure loss are expected for HLFC surfaces, given their typical range of $\frac{t}{d}$, as per Tab. 5.1. The friction losses inside the hole are linear with respect to the hole velocity, and may be assessed with the Darcy equation [26]. The entry and exit losses are inertial effects that scale with the square of the hole velocity [26]. The exit losses are normally dominant [57]. These two effects are generally modeled as in Eq. (5.3) [33, 57].

$$\Delta p = \tilde{A}\mu v_h + \tilde{B}\rho v_h^2 \tag{5.3}$$

The coefficients $\tilde{A}$ and $\tilde{B}$ are usually derived from experiments, as described in [57]. The present research investigates the scalability of pressure drop characteristics of perforated sheets, as a function of the governing similarity parameters. To assess scalability, the results should be independent of dimensional properties, but rather be only dependent on nondimensional properties. While $\tilde{B}$ is nondimensional, $\tilde{A}$ has dimensions m^{-1}. Therefore, $\tilde{A}$ is replaced by $A\frac{t}{d^2}$, such that A becomes nondimensional, and Eq. (5.3) is replaced by Eq. (5.4). The reason for introducing the term $\frac{t}{d^2}$ becomes apparent from the Darcy equation, used to describe the pressure loss in a pipe due to friction, which is given by Eq. (5.5) [18].

$$\Delta p = A\frac{t}{d^2}\mu v_h + B\rho v_h^2 \tag{5.4}$$

$$\Delta p = \frac{1}{2}\rho f \frac{L}{D} U^2 \tag{5.5}$$

Treating a suction hole as a pipe, and using the laminar friction coefficient from Eq. (5.6), evaluating Eq. (5.5) inside a hole results in Eq. (5.7). It can be seen that A takes part of the role of the friction coefficient.

$$f = \frac{64}{Re} \tag{5.6}$$

$$\Delta p = \frac{1}{2}\cdot 64 \cdot \rho \frac{\mu}{\rho v_h d}\frac{t}{d} v_h^2 = 32\frac{t}{d^2}\mu v_h \tag{5.7}$$

Expressing the pressure drop across a perforated sheet, given by Eq. (5.4), as a pressure drop coefficient using Eq. (5.1) results in Eq. (5.8). Now the dependency on the similarity parameters can be seen. A combination of Re_d and $\frac{t}{d}$ governs the viscous losses through a hole. Here the aforementioned result that the parameter $Re_d \cdot \frac{d}{t}$ should account for the sheet thickness reappears. The influence of β is absorbed in the definition of $C_{\Delta p}$, because the hole velocity is related to the mean velocity in the pipe through the open area ratio, as indicated by Eq. (5.9), which holds for incompressible conditions.

$$C_{\Delta p} = 2\left(A\frac{1}{Re_d \cdot \frac{d}{t}} + B\right) \tag{5.8}$$

$$v_h = \frac{v_w}{\beta} \tag{5.9}$$

Using Eq. (5.4) to model the pressure drop is further substantiated by analyzing another model for the pressure loss across a thick perforated sheet. As described in [30, 77], the pressure drop coefficient consists of a constant term and a viscous term, expressed by Eq. (5.10). Here the pressure drop coefficient was adapted so that it is based on the hole velocity instead of the mean pipe velocity, as was done in the reference.

$$C_{\Delta p} = K_0 + f\frac{t}{d} \tag{5.10}$$

The constant term K_0 is a function of β and $\frac{t}{d}$, which could be simplified with the knowledge of Tab. 5.1. Because $\frac{t}{d}$ of typical HLFC systems is large, it does not affect K_0. Furthermore, β of typical HLFC systems is in

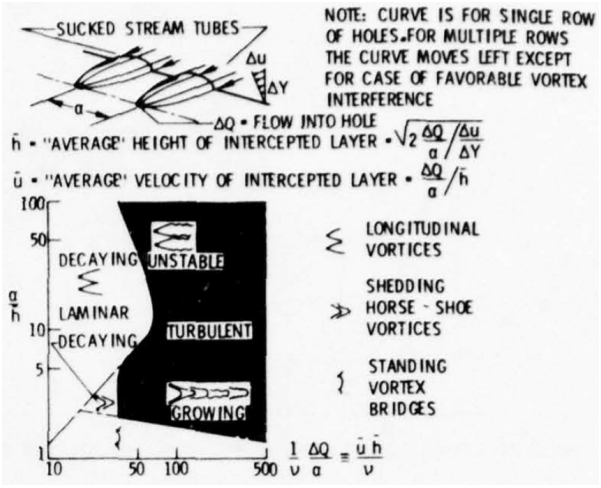

Figure 5.2: Critical suction limit for a single row of holes evaluated by Pfenninger [45]. Note the distinction in the type of vortex: streamwise vortices are formed at sufficiently large hole spacing and low suction rates, horseshoe vortices that shed periodically are formed at a denser hole spacing and at higher suction rates, and standing vortex bridges may form at high suction rates and dense hole spacing

the order of 1%. By assuming that $\beta \to 0$, K_0 simplifies to $\frac{3}{2}$. Even though the model is valid for turbulent conditions, taking the value of the laminar friction coefficient from Eq. (5.6) yields a prediction for the pressure drop coefficient, as shown in Eq. (5.11).

$$C_{\Delta p} = \frac{64}{Re_d \cdot \frac{d}{t}} + \frac{3}{2} \tag{5.11}$$

Comparing this result to Eq. (5.8) supports the validity of the model from Eq. (5.4). From this it may be expected that A will be in the neighborhood of 32, while B will be near $\frac{3}{4}$.

5.5. Estimating the Critical Suction Limit

Not only the pressure drop across a suction surface is a relevant consideration in the design on an HLFC component. The critical suction limit, which was introduced in Sec. 2.6.2, should also be considered. It is the suction rate at which premature transition occurs downstream of the suction hole because of the growth of the vortices induced by the suction hole. A goal is to find a practical design criterion that can be used to predict the critical suction limit for generic suction surfaces.

As reported in [67], there are many authors who developed a criterion for critical suction. Of these, the results obtained by Pfenninger are one of the most important [45]. They are presented in Fig. 5.2. A distinction is made between the type of vortex that is induced by the suction holes. These were discussed in Sec. 2.6.2.

A more recent investigation into the critical suction limit was performed by MacManus et al. in [36–38]. They developed a criterion for the critical suction limit of a single hole in [38]. For multiple rows of holes, each row induces more vorticity [37]. This is why the critical suction limit is reduced with multiple rows of suction holes. In fact, this is also what Pfenninger reports in Fig. 5.2. Unfortunately, there is no statement regarding by how much the critical suction limit is reduced for multiple rows of holes.

In spite of not knowing the critical suction limit for multiple rows of holes, MacManus and Eaton proceeded with the development of a parameter to be used as an engineering criterion for predicting the critical suction limit [36]. They presented a streamtube parameter, G_k, which may be used to estimate the critical suction limit. Given by Eq. (5.12) [36], it is a convenient parameter, because it uses parameters that are known to the designer, namely the volume flow rate into the suction hole, Q_h, and the slope of the velocity profile at the wall, $\left.\frac{\partial u}{\partial y}\right|_w$. The experimental results on a single suction hole demonstrate that G_k has approximately a single value at the critical suction limit, proving that G_k is suitable for use as a design criterion.

$$G_k = \frac{1}{\nu} Q_h^{2/3} \left(\left. \frac{\partial u}{\partial y} \right|_w \right)^{1/3} \tag{5.12}$$

The extension to multiple rows of holes for using the streamtube parameter G_k as a design criterion for critical suction was studied by means of a CFD study in [37]. The computational results supported the conclusion that the parameter G_k should be suitable for characterizing the critical suction limit in transonic flight conditions of HLFC suction surfaces containing multiple rows of holes. However, further experimental research is required to estimate the critical suction limit. A potential starting point would be to evaluate the experimental data from [67] with the parameter G_k.

Another important effect to consider on swept wings is the possible interaction between the suction holes and the cross flow vortices. Introduced in Sec. 2.6.2, the streamwise vortices coming from the suction holes are contra-rotating while the CF vortices are co-rotating. It can be imagined that there is some hole layout that promotes the interaction of the vortices coming from the suction holes with the CF vortices. With a constructive interaction, the CF vortices may amplify and boundary layer transition may be triggered due to the presence of suction holes. MacManus and Eaton present guidelines for when this constructive interaction may occur in [36]. This can provide a first order estimate for design purposes.

5.6. Suction Power for HLFC Components

Boundary layer suction does not come for free, but always features an associated drag. Depending on the system, this drag may be sink drag or pump drag, or a combination of both. Sink drag originates from the air sucked into the wing which loses some or all of its momentum [8]. Sink drag can be overcome by pumping the suction air back to freestream total pressure before exhausting it [8, 12]. However, this requires a pump, which is the source of pump drag. Hence, a suction system will always create additional drag, even if it is passive. A passive suction system will not be able to exhaust the suction air at freestream conditions, so it will create sink drag. Still, a passive system may be more efficient than an active system, because a pump introduces additional efficiency losses.

Pump drag and sink drag depend on the internal layout of the suction system, including all the ducts, and the inlet and outlet locations. It is not the aim of this section to assess the drag of any arbitrary suction system. Instead, the focus will be on minimizing the pump requirements, in turn reducing associated losses.

A first solution for reducing the pump requirements is to place the suction inlets and outlets in convenient locations, as was studied in [71]. Because the suction air has to be pumped back to freestream conditions, the lower the pressure at the suction inlet, the greater the pumping losses will be. Therefore, it is more efficient to apply suction in regions with higher pressure. If the outlet is at lower pressure than the inlet, part or all of the required suction can be realized passively. This reduces the pump requirements further. A trade-off must be made between pump drag and sink drag in the design of the suction system.

In the design of a suction system, it may be tempting to apply suction early on to prevent the amplification of disturbances. However, there is very little memory effect in the stability of the boundary layer [75]. The shape of the velocity profile is primarily determined by the local pressure gradient and the suction velocity, which implies that the upstream history of the boundary layer does not have much effect [75]. Therefore, it is not efficient to apply suction too early. Instead, the suction distribution should be designed according to the local stability requirements of the boundary layer [75].

Besides focusing on optimizing the boundary conditions for the suction system, pump requirements may be reduced further by designing the airfoil in a smart way so that it achieves the desired transition delay with the least amount of suction provided. Because a swept wing is susceptible to the CF instability, suction will be required. However, with a clever airfoil design, the required suction rates are reduced.

In fact, this design philosophy is used at DLR (German Aerospace Center). Guidelines for NLF on a swept wing are outlined in [59]. Of course, suction can be used to overcome any reasonable problem with disturbance growth. But, applying these guidelines to the design of HLFC wings can limit the required amount of suction [59]. If the airfoil section already suppresses much of the growth of the TS and CF instabilities due to

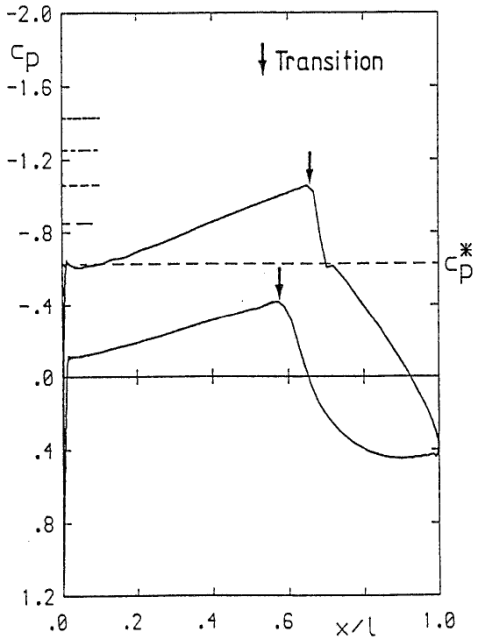

Figure 5.3: Design pressure distribution for minimizing the suction requirements for HLFC on a swept wing [59]. Note the strong initial acceleration over the upper surface, followed by a brief deceleration, after which a mild, favorable pressure gradient is used up to the point of transition

its shape, only a small amount of additional suction may be required to obtain the desired transition delay.

DLR has developed target pressure distributions for NLF or HLFC on swept wings [59]. An example is shown in Fig. 5.3 and contains several interesting features. While a pressure gradient promotes CF (Sec. 2.3.2), it is needed to create lift, requiring a reduction in pressure on the upper surface. The approach used at DLR is to 'get it over with.' In other words, a region of very strong acceleration is used to get to the required low pressure [59]. Because the acceleration is strong, the target pressure is reached very quickly. Therefore, the CF disturbances grow quickly in this region but only for a short distance. After this short region, the pressure gradient must be reduced so that the CF disturbances do not grow dangerously high [59].

The cross flow instabilities can be controlled even more effectively if a very small, local suction peak is created at the end of the strong acceleration [59]. Behind this suction peak, also visible in Fig. 5.3, the flow briefly decelerates, changing the direction of cross flow. This is intended to suppress stationary CF vortices that form in the acceleration region [59].

Behind the region of strong acceleration, the pressure gradient becomes very mild, as seen in Fig. 5.3. This is intended to prevent the strong growth of CF instabilities. Still, a slightly favorable pressure gradient is maintained in order to suppress the TS waves [59]. With such a pressure distribution, the TS and CF instabilities are already suppressed to a large extent just by appropriate airfoil shaping. This may not always be sufficient to achieve laminar flow up to the shock wave, which is why suction may be incorporated. But, because the airfoil is shaped favorably, the suction requirements will be low, leading to small pump requirements.

6

Experimental Setup

An essential aspect of designing an HLFC component is an accurate estimate of the required pressure difference across the surface in order to obtain the desired suction rate. Section 6.1 outlines the experimental setup used to measure the pressure drop across perforated sheets. The manufacture of these sheets is discussed in Sec. 6.2. Subsequently, Sec. 6.3 describes the optical setup used to characterize their geometric properties. This method was calibrated with external measurements, which is documented in Sec. 6.4. Finally, Sec. 6.5 presents the experimental matrix of perforated articles that was used for the experiments.

6.1. Experimental Setup Pressure Drop for HLFC

As Chap. 5 indicated, the pressure loss across suction sheets consists of two components: the primary pressure loss due to the flow through the perforated sheet, and a secondary pressure loss due to the presence of a tangential flow. This tangential flow, illustrated in Fig. 2.11b, introduces additional boundary layer properties that govern the pressure loss. Therefore, the experimental setup and subsequent analysis of results is simplified by excluding tangential flow, resulting in the situation portrayed in Fig. 5.1. This allows a more detailed analysis into how the remaining similarity parameters affect the primary pressure loss of suction surfaces.

An experimental setup excluding tangential flow can be realized by the flow through a pipe. The perforated sheet is placed inside the pipe, perpendicular to the flow, aligning the axes of the perforations with the freestream direction. With this setup, all air passing through the pipe must go through the perforations, rendering the concept of a suction coefficient irrelevant. The experimental setup used in this research is shown schematically in Fig. 6.1, indicating how the test section is oriented perpendicular to the flow.

The configuration shown in Fig. 6.1 starts with a supply of pressurized air at 10 bar. Afterwards, a pressure regulator reduces the pressure to roughly 3 bar. The pressure regulator also damps out some fluctuations in the air supply system, providing a steadier inflow to the subsequent mass flow controller. A Bronkhorst

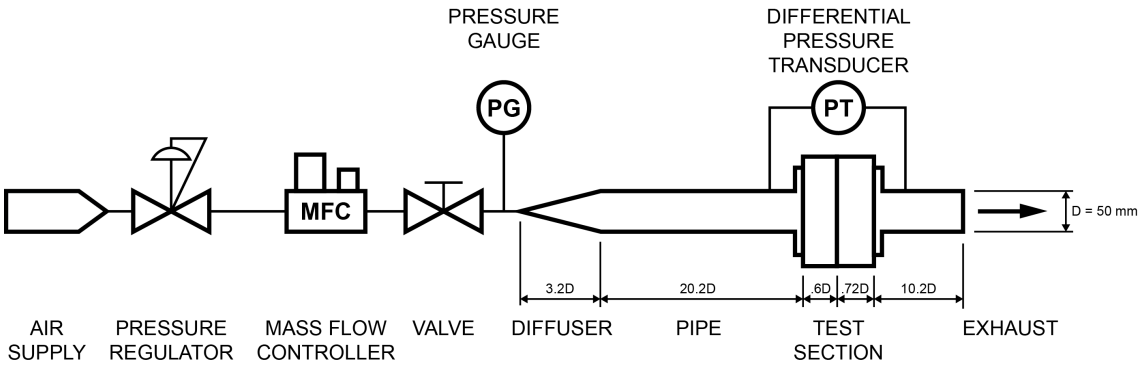

Figure 6.1: Schematic of experimental setup for testing the primary pressure loss of perpendicular flow through a perforated sheet. Not to scale

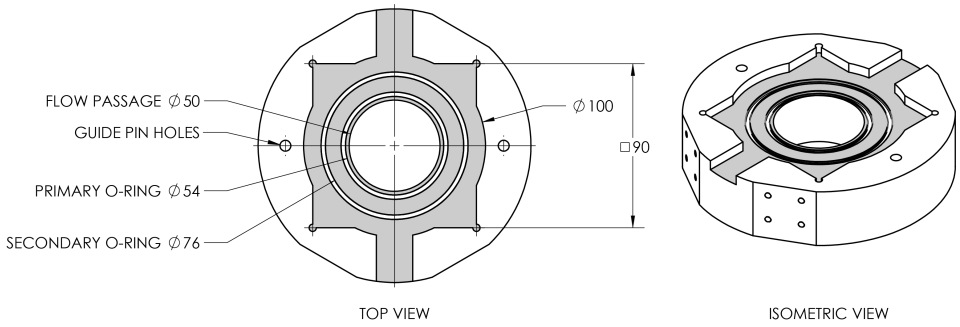

Figure 6.2: Schematic of lower test section holder, indicating the seating surface for a perforated sheet in gray

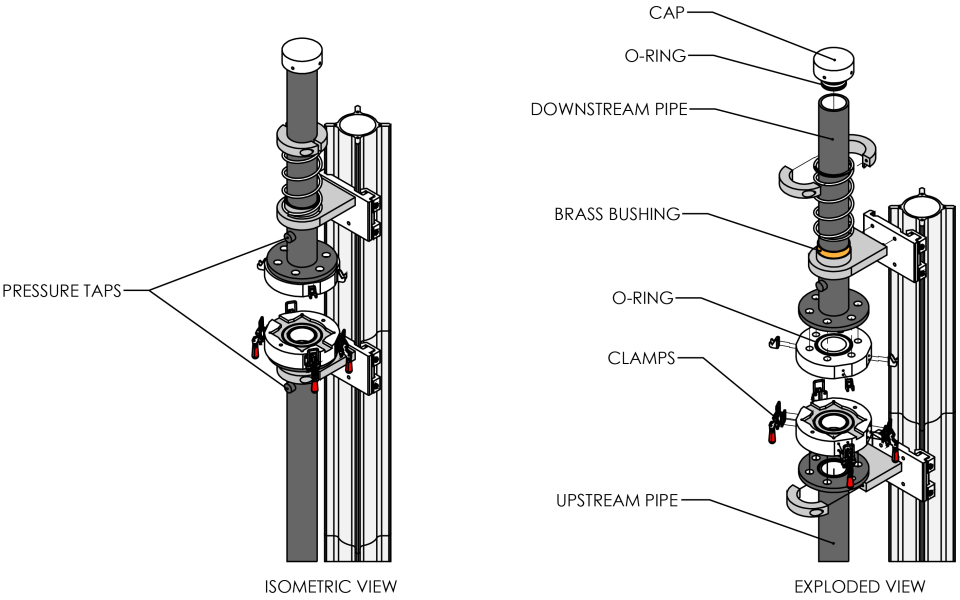

Figure 6.3: Assembly drawing and exploded view of the experimental setup, indicating how the test section holders are mounted to the pipes, along with the location of the clamps, pressure taps, and the cap that is used for leakage tests

F-202AV-M20-DGD-55-V mass flow controller sets the desired mass flow rate through the test section. The controller is computer-actuated and registers the flow rate along with the flow temperature at an acquisition frequency of 5 Hz. The next components are a valve and a pressure gauge, which are used for leakage tests. Air then flows into a diffuser, which adapts the cross section of smaller, flexible hoses used upstream to the 50-mm inner diameter of the pipe. Two holders, as illustrated in Fig. 6.2, keep the test article in place. The internal diameter remains constant until reaching the outlet, where the flow is exhausted into the ambient air.

The test section holders were designed to fit sheets with a perforated area of 50 mm in diameter (Fig. 6.5b), matching the pipe diameter. The sheets have to be larger than the perforated area so they can be clamped in the experimental setup. The test section holders were designed such that they allow circular sheets with a diameter of 100 mm and square sheets with sides of 90 mm, as shown in Fig. 6.2. This area also contains grooves for O-rings, in order to ensure proper sealing of the flow rig. Two sets of O-rings are used on either side of the test article, providing redundancy. The smallest O-ring has an inner diameter of 54 mm, leaving a ring of 2 mm around the main passage of the pipe. Air can flow into this region, but it will remain stagnant, because the perforated sheets only contain holes inside the main diameter of the pipe. Therefore, this space should not affect the measured pressure losses. The holders are bolted to the pipes, with an O-ring in between to ensure a proper seal, as indicated in Fig. 6.3. The holders are clamped together by means of four adjustable clamps, also shown in Fig. 6.3. These clamps allow sheets of different thicknesses to be mounted in the setup. Two guide pins are fitted in the holders, ensuring a proper alignment of the two pipes.

Figure 6.4 shows that the pipes were mounted vertically. This was done for two reasons. The first is that

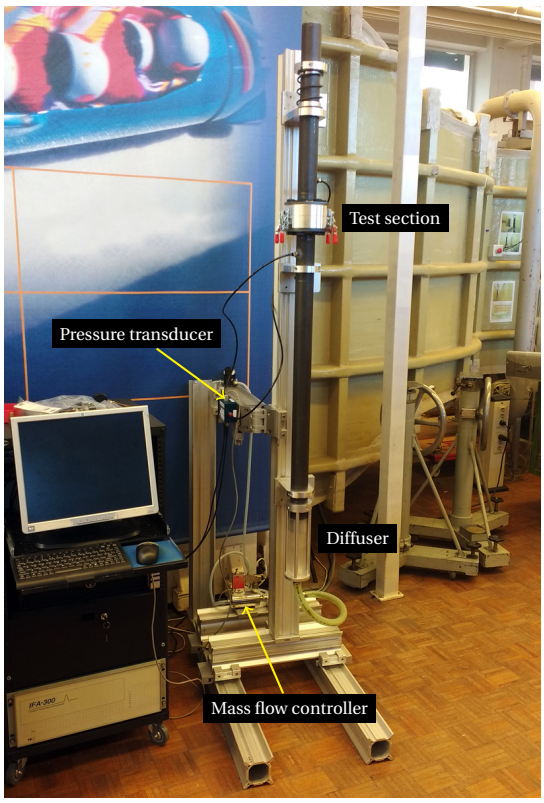

Figure 6.4: Experimental setup for measuring pressure drop across perforated sheets. Note the location of the components from Fig. 6.1

test articles can be laid on top of the bottom holder before closing the system. This prevents test articles from falling out easily, which could occur if the pipes were mounted horizontally. Convenient switching of test articles is facilitated by a spring on the upper pipe. This spring is compressed when the setup is closed, causing the spring to hold the setup open when the clamps are undone. This way, the test section can be opened without manual support, freeing both hands for changing the test article. The second reason the pipes were mounted vertically is that the assembly takes up less floor space than if it were mounted horizontally.

The pressure drop across a perforated sheet is measured with a differential pressure transducer. Two different pressure sensors were used: the primary sensor, a Honeywell SSCSAAN600MDAA5, has a range of ±60 kPa covering the entire expected pressure range; the secondary sensor, a Mensor DPG 2400, has a range of -1 kPa to 6 kPa intended to provide more accuracy for lower pressure differences. These sensors were installed such that they could rapidly be interchanged.

The locations of the pressure taps were at $2.2D$ upstream and $2.32D$ downstream of the test article, taking into account the thickness of the test section holders. As Malavasi et al. state, the standard for the upstream pressure tap is to locate it between $0.5D$ and $2.5D$ [39], so the upstream tap was placed appropriately. On the other hand, the proper location of the downstream pressure tap is affected by the pressure recovery after the recirculation regions behind the test article. This effect was studied in Sec. 7.2, which demonstrated that the downstream pressure tap was appropriately located.

The airtightness of the system was ensured by placing O-rings between the perforated test article and the test section holders (Fig. 6.2), and also between these holders and the pipes (Fig. 6.3). Furthermore, threaded fittings between components of Fig. 6.1 were applied with thread seal tape. Airtightness was tested by performing a leakage test on the part downstream of the mass flow controller, since leaks upstream of the flow controller are not critical. The system was sealed by plugging a cap with an O-ring into the outlet, as indicated in Fig. 6.3. Then, the mass flow controller was opened to elevate the gauge pressure in the system to over 2 bar, after which the valve downstream of the mass flow meter (see Fig. 6.1) was closed. The pressurized

system retained some residual elevated pressure when left overnight. Therefore, any leak was considered so small as to not influence the flow measurements.

Because this experimental setup deals with pipe flow, the entrance length should be considered. The entrance length is the distance required to reach fully developed pipe flow, where the velocity profile does not change anymore. For laminar flow, the entrance length L_e is given by $L_e/D = 0.06Re_D$ [79]. Flow in a pipe remains laminar up to approximately $Re_D = 2,000$ [18], which implies a required entrance length of $120D$. In the present research, the length of the pipe up to the test article is $20.8D$, as follows from Fig. 6.1, only guaranteeing fully developed pipe flow up to $Re_D = 347$. However, the criterion for the entrance length considers that the flow converges into the pipe from a large reservoir, which means the boundary layer on the pipe walls develops from scratch. But, upstream of the pipe, Figs. 6.1 and 6.4 show that the flow already goes through hoses and the diffuser before entering the pipe. Therefore, a boundary layer would have already developed, making it likely that fully or nearly fully developed pipe flow is reached up to $Re_D = 2,000$.

6.2. Manufacturing of Perforated Test Articles

Section 6.1 introduced the experimental setup with which perforated sheets can be tested. However, before performing an experiment, these perforated sheets have to be manufactured. A cost-effective solution is described in this section, allowing a large test matrix of geometric parameters to be explored experimentally.

As mentioned in Sec. 6.1, the test articles are sheets with a perforated area of 50 mm in diameter, and should be either a disk of 100 mm in diameter or a square with 90-mm sides. The hole size of typical HLFC applications is in the order of 0.1 mm (Tab. 5.1), which is time-consuming to obtain with mechanical drilling. Obtaining such a hole diameter combined with the values of $\frac{t}{d}$ typical for HLFC is especially difficult for mechanical drilling. Instead, laser drilling is more suitable to these kinds of holes. In fact, a company[1] specialized in laser drilling acrylic sheets manufactured the test articles for the present research. Sheets with thicknesses of 1–8 mm can be drilled with holes as small as 0.2 mm at a cost of around 10 euros each.

6.3. Optical Setup to Characterize Hole Properties

After manufacturing, the geometric properties of the perforated sheets should be quantified. An optical setup was used in this research. Shown in Fig. 6.5a, it consists primarily of a light table and a digital camera. A perforated test article is placed on the light table, which emits fluorescent light that passes through the holes and is captured by the camera that hangs over it. The focal length of the lens was 200 mm, leading to an object distance of approximately 0.8 m. These and other camera properties are summarized in Tab. 6.1. This allows the perforated region to be captured in a single image with little perspective or distortion. A typical result is shown in Fig. 6.5b.

Table 6.1: Camera properties and settings used during experiments

Property	Value
Camera model	NIKON D80
Image size	3872 × 2592 pixels
Sensor size	23.6 mm × 15.8 mm
Pixel pitch	6.1 μm
Object distance	~0.8 m
Focal length	200 mm
Magnification factor	~0.33
F-stop	f/13
Exposure time	1/4 s
ISO	100

After acquiring the images of the perforated sheets, they were analyzed with a boundary recognition algorithm to identify the holes, using the image processing toolbox from MATLAB[2]. The image was first con-

[1] http://www.laserbeest.nl/
[2] https://www.mathworks.com/products/matlab.html

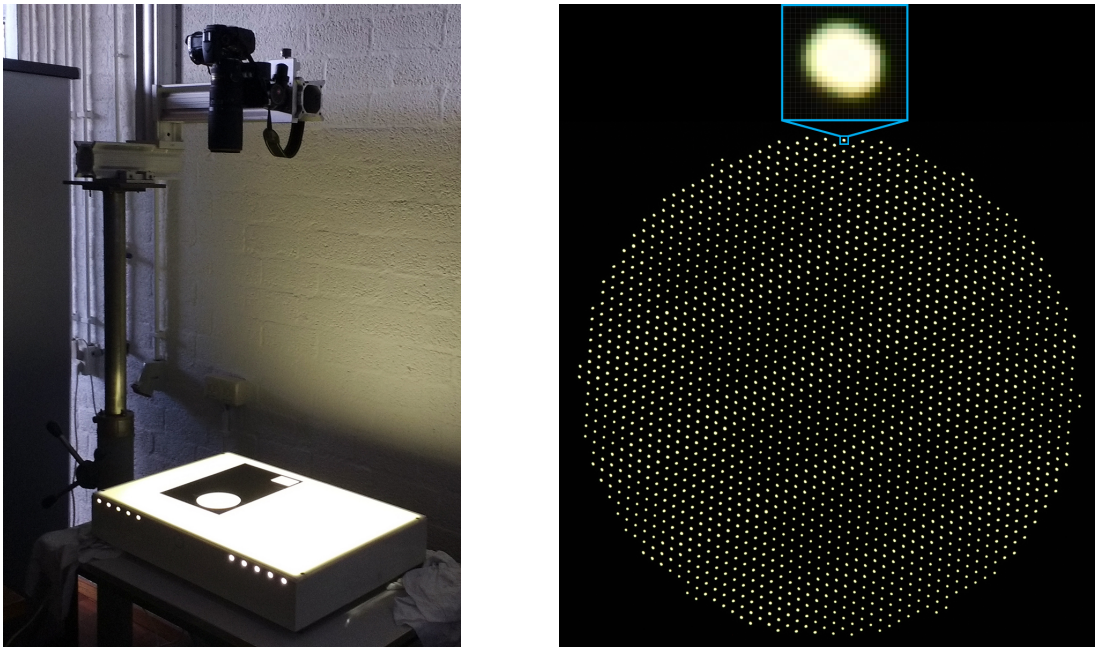

(a) (b)

Figure 6.5: Optical setup for quantifying hole properties of perforated sheets using a light table and a digital camera. (a) Optical setup showing the light table emitting fluorescent light and the camera above the table, hanging from a stand. (b) Typical image captured with this setup including zoom onto a single hole

verted to grayscale and then binarized. The default method to select the threshold was used, which comes from Otsu [44]. After binarizing, the hole boundaries can be traced, from which statistics such as hole area and equivalent diameter can be deduced. For an accurate estimate of the hole size, a single hole should be covered by a sufficient amount of pixels. In fact, even the perforated acrylic article with the smallest holes, illustrated in Fig. 6.5b, featured 143 pixels per hole on average, which was deemed sufficient. Converting dimensions from pixels into units of length was done by taking a calibration image of a sheet of graph paper with the camera in the same position.

The benefit of taking a single image of the entire perforated area is that all holes are measured at the same time. Therefore, an accurate representation of the variation in hole size is obtained. This also implies that this method provides a good estimate of the total open area. This method is thus faster than techniques that measure holes individually, for example using a microscope.

However, the accuracy of this method must be validated. Because a camera is used, diffraction of light may be an issue. Furthermore, the entire perforated area is captured in a single image. This means most holes are not aligned directly with the line of sight of the camera. The large focal length of the lens reduces this effect, since the object distance is about 0.8 m, but it does not eliminate the fact that some of the internal walls of the holes can be seen. In order to account for this, the exposure time must be set such that the walls do not produce shadows. On the other hand, overexposure may lead to holes appearing larger than they are in reality. Because of these uncertainties, a comparison with another measurement technique is called for.

6.4. Calibration of Optical Setup

In order to validate the results obtained with the optical setup described in Sec. 6.3, a comparison was performed with measurements of individual holes obtained with a microscope: a Keyence Digital Microscope VHX-2000E. It is capable of magnifications between 100 and 1000 times, where 100 times was used in the present research. Because the microscope zooms in on a single hole, its size can be estimated more accurately. This information can be used to calibrate the results obtained with the optical setup. The strength of the optical method lies in its ability to measure all holes. This means relative hole sizes are captured well, even if the absolute size is offset compared to the more accurate measurements with the microscope. Com-

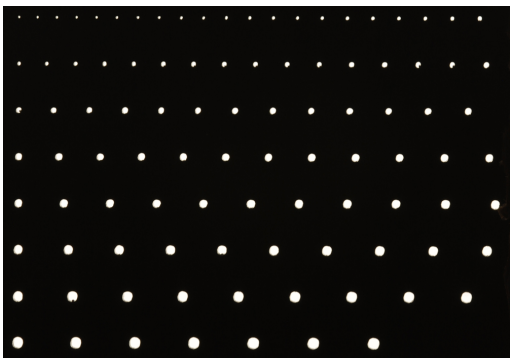

(a) Laser-drilled acrylic article

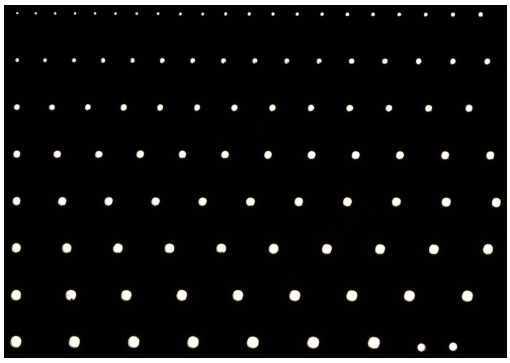

(b) Article (a) containing two additional mechanically drilled holes in lower right corner

Figure 6.6: Perforated acrylic articles used for calibration of optical setup

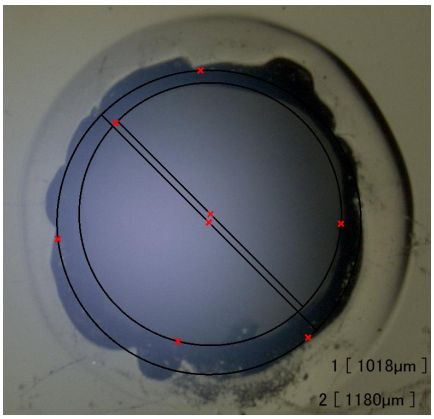

(a) Laser entry side

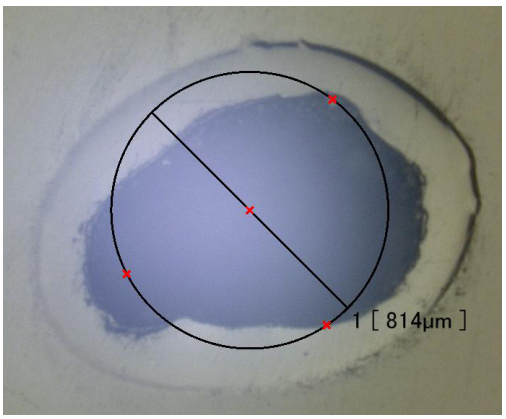

(b) Laser exit side

Figure 6.7: Microscope images of individual laser-drilled holes

bining these techniques should therefore provide a good estimate of the open area of a perforated sheet.

A dedicated set of perforated acrylic articles was manufactured, containing holes with a specified diameter between 0.02 mm and 1 mm, in increments of 0.01 mm, as illustrated in Fig. 6.6a. These articles were made in thicknesses between 2 and 8 mm, because a different thickness leads to a slightly different object distance for a fixed position of the camera. The purpose of these dedicated articles was twofold: first, to compare the diameter obtained with the optical setup and the microscope for a subset of holes, in order to calibrate the optical method; and second, to have a relation between the specified diameter and the diameter resulting after manufacturing. This second piece of information was used to design the desired test matrix.

Data points for the calibration were obtained primarily on the laser entry side of the acrylic articles, because the holes were more circular compared to the laser exit side. In fact, the nonuniformity of holes on the laser exit side prevented good measurements of the diameter, as illustrated by Fig. 6.7. Moreover, Fig. 6.7a highlights an ambiguity in the definition of the hole: the inner part of the hole has a lighter color than the surrounding, darker ring. It was hypothesized that only the lighter part constitutes the actual hole through which fluid passes, because holes on the laser exit side (Fig. 6.7b) featured a smaller surrounding ring.

In order to test this hypothesis, additional holes were mechanically drilled into the laser-drilled articles, as shown in Fig. 6.6b. While laser-drilling produces holes with an unknown size before calibration, mechanical drilling produces holes comparable to the drill size itself. Microscope images of these holes (Fig. 6.8) indicate that the inner region is the actual hole, because the observed diameter was near the drill size of 0.8 mm. It is believed the dark rings around the holes represent surface damage from the drilling process. In order not to bias the calibration due to the drilling method, only the data points from laser-drilled holes were used.

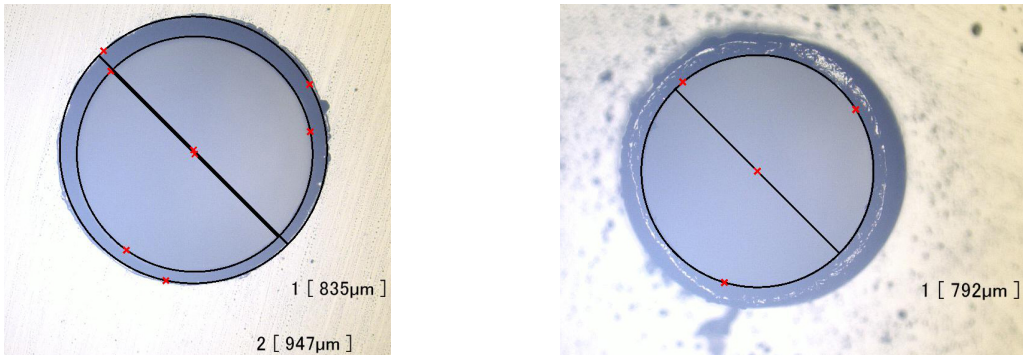

(a) Drill entry side (b) Drill exit side

Figure 6.8: Microscope images of mechanically drilled holes with 0.8-mm drill

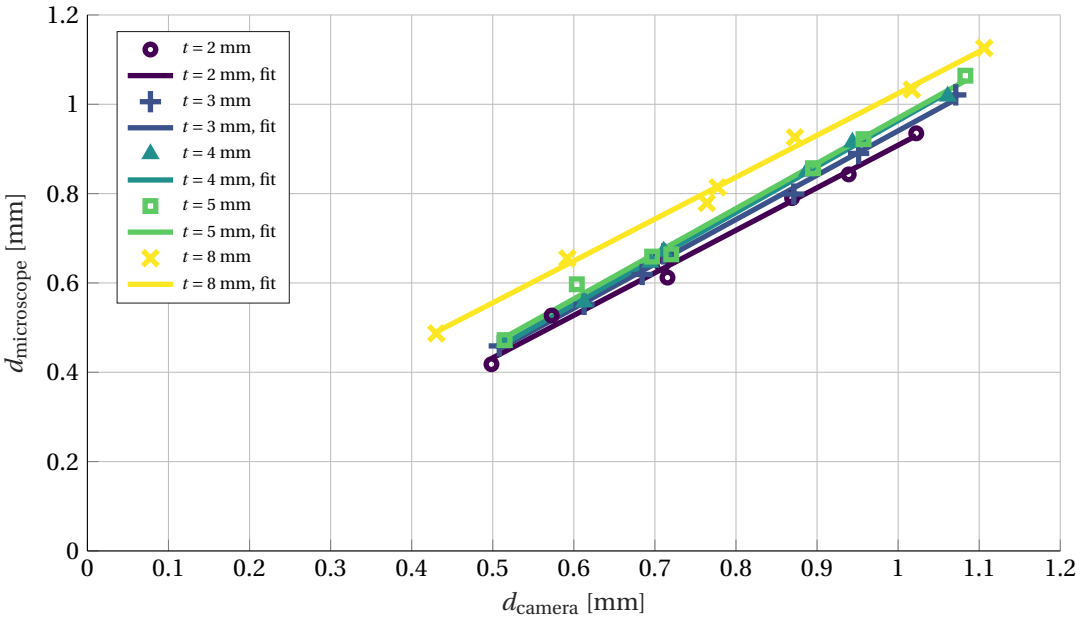

Figure 6.9: Calibration of optical setup with microscope: fit between observed (camera) and actual (microscope) hole diameter allows correction of measurements taken with optical setup

The results of the calibration procedure are shown in Fig. 6.9, containing the measurement data obtained with the microscope, along with a linear fit on the data. The calibration was performed on sheets with several thicknesses, in order to account for optical effects, such as diffraction and varying object distance with thickness. The trend lines were used to correct the processed results from the images captured with the optical setup, so that the actual hole diameter—as determined with the microscope—was assessed. Note that the calibrated hole diameter increases with thickness, likely due to higher laser power for thicker sheets.

Treating the microscope measurements as the true reference, the calibration procedure accounts for all errors in the optical setup and boundary recognition algorithm. These errors include diffraction, varying object distance with thickness, errors in the image processing algorithm, shadows within long holes, and errors in the threshold for binarizing the images. The remaining error is the standard deviation of the measurement data in Fig. 6.9 relative to the linear trend line, which can be considered as the uncertainty of the calibration. In order to retain the validity of the calibration results, images of the perforated articles used for calibration and those used for the flow measurements were all taken using the same settings from Tab. 6.1. Moreover, the light table was covered with opaque material around the perforated articles and room lights were turned off, such that mainly the light passing through the perforated articles was captured by the camera.

6.5. Test Matrix

The test matrix was intended to cover the typical ranges of the similarity parameters for HLFC systems, as presented in Tab. 5.1. While the typical hole diameter of 0.1 mm or less could not be obtained with the laser-drilled acrylic sheets, the other nondimensional similarity parameters could be matched. The open area ratio is a function of the hole diameter and the number of holes. So, for the acrylic articles with a scaled-up diameter, the number of holes was adjusted such that β was in the order of a few percent. Holes were always placed in an equilateral triangular pattern.

The typical aspect ratio of HLFC perforations was the most difficult to achieve. Generally, the higher $\frac{t}{d}$, the more difficult manufacturing becomes, either by mechanical or laser-drilling. Therefore, most of the test matrix was designed to have $\frac{t}{d}$ near 10, the lower limit of typical HLFC systems, such that production was feasible. Still, the final test matrix features some spread in $\frac{t}{d}$, so the effect of that parameter could be assessed.

The hole Reynolds number is controlled primarily by the flow rate, enabling a wide range of data points. However, in order to stay within the typical range of Re_d, a lower hole diameter was preferred. Furthermore, the variation in flow rate was limited to $Re_D < 2,000$, such that laminar flow in the pipe was guaranteed.

The design philosophy of the test matrix was to feature several variations in parameters, to study their effect. First, a variation in open area ratio, keeping both d and t constant, enabling the assessment of the effect of β. Furthermore, a variation in d, keeping β and $\frac{t}{d}$ constant, allowing a study on the scalability of the experiments. Next, a variation in $\frac{t}{d}$, keeping β and d constant, so that its effect could be studied. This was realized by drilling the same pattern into sheets of multiple thicknesses.

An initial set of nine test articles was produced, intended to provide an estimate of the expected pressure drop and an initial insight into the effect of the similarity parameters. Because these articles were produced before performing the calibration described in Sec. 6.4, their exact geometric properties were unknown in advance. But, the results of these tests helped refine the test matrix for the second set of test articles.

After performing the calibration procedure, a relation between the specified hole diameter before drilling to the calibrated diameter obtained after drilling could be established, as shown in Fig. 6.10. The second set of ten acrylic test articles was produced with this relation, allowing the desired geometric properties to be obtained. The effect of $\frac{t}{d}$ was intended to be studied using three articles with thicknesses of 4, 5, and 8 mm, into which the same pattern of 0.4-mm holes would be drilled. This would have resulted in a variation in $\frac{t}{d}$ of 10–20, covering a large part of the typical range indicated by Tab. 5.1. However, the thickest article contained some blind holes and many that were nearly blind. Therefore, its open area ratio could not be reliably estimated and this article was excluded from further analysis. A total of 18 acrylic articles was tested.

Additionally, a set of three perforated titanium test articles was produced at the Sirius Laser Facility at TU Delft, intended to demonstrate the capabilities for laser-drilling of titanium at TU Delft. The facility involves a pulsed, 1-kW XeCl laser that operates at the ultraviolet wavelength of 308 nm and is especially suited to laser drilling. The laser-drilled titanium articles are valuable, because they feature the typical hole diameter of HLFC systems, namely 50 μm. This enables a comparison of the large-scale acrylic articles to the industrial scale of HLFC components. However, since the titanium articles were made to test the laser-drilling process, the drilling settings were not yet perfected. Therefore, there is a relatively large spread in the hole diameter in the titanium articles. In addition, a significant share of holes was blind, in the order of 10%, which was determined using the optical setup. The open area ratio was adjusted accordingly.

Even though the hole diameter is not a similarity parameter, the test matrix includes it because it concerns the scalability of the experiments. The other parameters included in the test matrix are β and $\frac{t}{d}$. Because $\frac{t}{d}$ was kept near 10 for most articles, the test matrix can be represented in a simplified, two-dimensional way in Fig. 6.11. The variation in $\frac{t}{d}$ is indicated in the three-dimensional representation of the test matrix in Fig. 6.12. The test matrix is tabulated in Tab. 6.2.

The uncertainty of the hole diameter can be represented in two different ways. The first is the calibration uncertainty associated to errors with the optical setup, which only applies to the acrylic articles. This is indicated in Fig. 6.11. The propagation of this uncertainty to the open area ratio is treated in App. C. The sec-

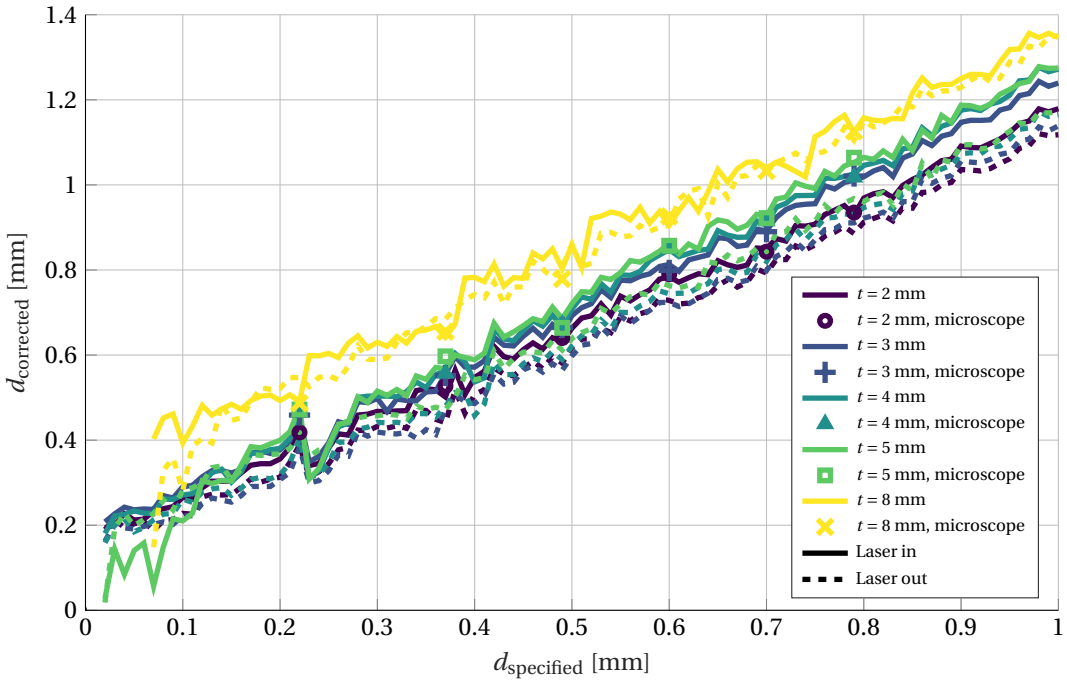

Figure 6.10: Corrected diameter as function of specified diameter, used for design of test matrix

ond uncertainty is the spread in hole size within each article. For the acrylic articles, all holes are measured with the optical setup. Therefore, the spread in hole size need not be considered for the uncertainty of the open area ratio, because β is the sum of the known areas of each individual hole, as illustrated by Eq. (6.1). However, each hole size is first calibrated, thereby introducing the calibration uncertainty.

$$\beta_{\text{acrylic}} = \frac{\sum_{j=1}^{N} d^2_{\text{calibrated}}}{D^2} \tag{6.1}$$

In contrast, the holes in the titanium articles were measured with the same microscope as mentioned in Sec. 6.4. Therefore, the calibration uncertainty need not be considered. A subset of the total number of holes was measured, which implies in this case that the spread in hole size *is* an uncertainty that propagates into the open area, because the open area is now derived from the mean hole diameter, as shown by Eq. (6.2).

$$\beta_{\text{titanium}} = N\frac{d^2_{\text{mean}}}{D^2} \tag{6.2}$$

Besides the spread in the hole size, the nonuniformity of the hole shape can also be investigated using the optical setup. The departure from a circular shape was assessed by means of a roundness error, which can be defined in multiple ways, according to [68]. In the present research, the roundness error is defined using the minimum circumscribed circle method, which was found to be simple and reliable. For this method, the roundness error is the largest deviation from the smallest circle that encloses the hole [68].

For the perforated acrylic test articles, the spread in diameter and the roundness error are presented in Fig. 6.13. Here the roundness error is expressed as a fraction of the radius of the minimum circumscribing circle. It can be seen that the roundness error is generally larger on the laser exit side, which goes hand in hand with the larger spread in hole diameter on the laser exit side. The titanium articles were not analyzed with the optical setup, so no information about the roundness of the holes is available. However, the spread in hole diameter for the titanium articles is presented in Fig. 6.11.

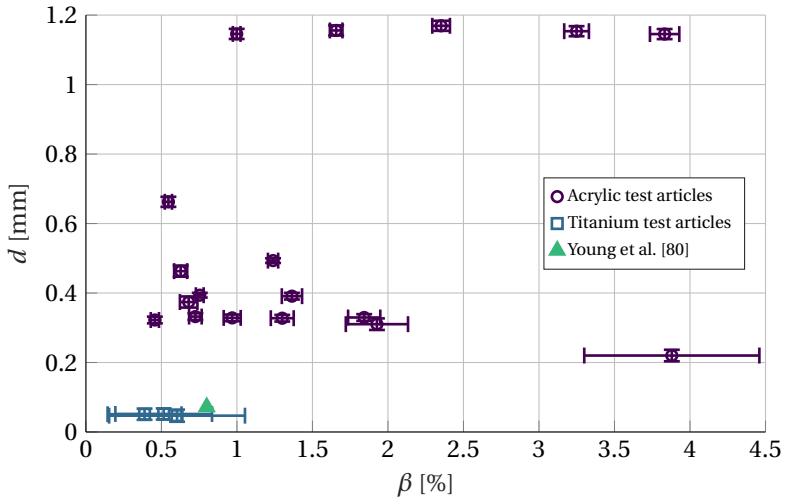

Figure 6.11: Two-dimensional test matrix showing perforated acrylic and titanium articles including uncertainty on hole diameter (1σ)

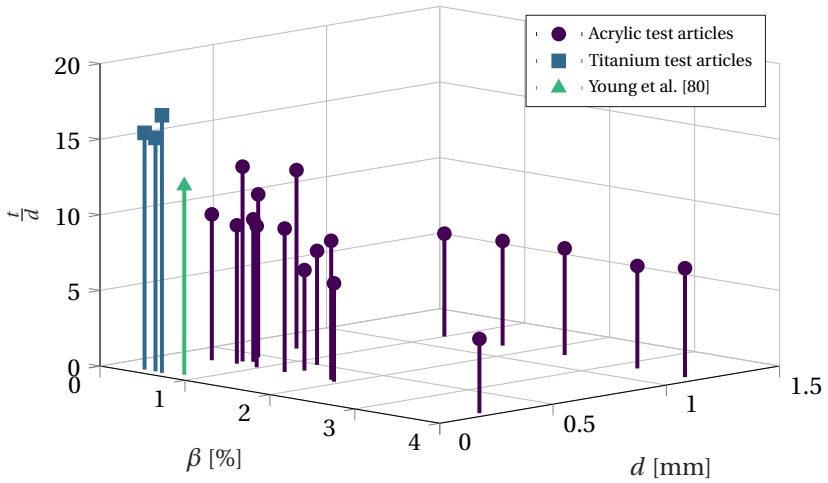

Figure 6.12: Three-dimensional test matrix showing perforated acrylic and titanium articles

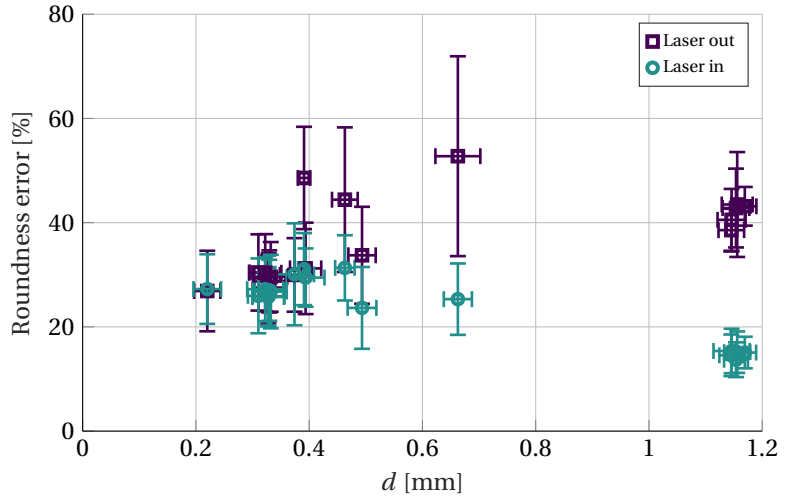

Figure 6.13: Roundness error versus hole diameter for acrylic test articles including spread in hole size and spread in roundness (1σ)

Table 6.2: Test matrix of the perforated acrylic and titanium articles, including properties of both the laser entry and exit sides. $\frac{t}{d}$ evaluated using d of most restrictive side. σ_d denotes the spread in calibrated hole diameter (d) but does not include calibration uncertainty. RND denotes the roundness error according to the same definition used in Fig. 6.13

						Laser entry side				Laser exit side			
ID	Material	N	Pitch [mm]	t [mm]	$\frac{t}{d}$ [-]	β [%]	d [μm]	σ_d [μm]	RND [%]	β [%]	d [μm]	σ_d [μm]	RND [%]
S1	Acrylic	163	3.72	3.04	9.2	1.23	433	28	26.8	0.72	332	29	29.6
S2	Acrylic	421	2.31	3.03	9.2	3.05	425	29	27.0	1.84	330	29	28.7
S3	Acrylic	301	2.72	3.11	9.5	2.37	443	28	25.7	1.30	328	27	27.1
S4	Acrylic	223	3.14	3.07	9.3	1.72	438	28	25.9	0.97	328	27	27.5
S5	Acrylic	109	4.47	3.11	9.6	0.85	439	32	27.2	0.46	322	29	30.4
S6	Acrylic	121	4.28	3.71	9.4	1.12	479	33	29.5	0.75	394	28	31.2
S7	Acrylic	73	5.45	4.99	10.8	1.04	595	17	31.3	0.63	463	23	44.4
S8	Acrylic	121	4.28	4.82	12.9	1.06	467	34	30.1	0.68	374	26	30.0
S9	Acrylic	31	8.72	7.82	11.8	0.88	842	25	25.3	0.55	663	40	52.8
S10	Acrylic	43	6.96	8.25	7.1	2.35	1169	20	15.1	2.43	1189	20	43.1
S11	Acrylic	31	8.40	8.00	6.9	1.66	1156	23	15.2	1.66	1158	27	43.5
S12	Acrylic	73	5.44	8.25	7.2	3.83	1145	21	14.6	3.98	1167	23	38.6
S13	Acrylic	61	6.00	7.82	6.8	3.31	1164	21	13.7	3.25	1154	24	42.8
S14	Acrylic	19	10.4	7.80	6.8	1.05	1173	32	15.4	1.00	1146	25	40.5
S15	Acrylic	127	4.12	3.72	7.5	1.80	595	25	23.6	1.24	493	24	33.7
S16	Acrylic	223	3.15	2.60	6.7	2.19	496	11	31.1	1.36	391	11	48.6
S17	Acrylic	499	2.12	2.02	6.5	2.92	382	18	26.0	1.93	310	16	30.4
S18	Acrylic	1981	1.07	1.08	4.9	5.30	257	24	27.3	3.88	220	23	26.9
S19	Ti	6845	0.50	0.80	17.0	-	-	-	-	0.60	47	17	-
S20	Ti	4801	0.60	0.80	15.4	-	-	-	-	0.52	52	16	-
S21	Ti	3720	0.70	0.80	15.7	-	-	-	-	0.39	51	16	-

7

Experimental Results

The present chapter presents the experimental results, starting with the way in which the data was processed in Sec. 7.1. Then, the pressure recovery distance was investigated in Sec. 7.2, in order to validate the experimental setup. The entire set of experimental results regarding the pressure drop across perforated sheets is presented in Sec. 7.3. Afterwards, more attention is given to the influence of individual parameters, starting with the effect of the open area ratio in Sec. 7.4, then the effect of the aspect ratio of the holes in Sec. 7.5, and the influence of compressibility in Sec. 7.6. The scalability of the experimental results is discussed in Sec. 7.7. Finally, an uncertainty analysis was performed in Sec. 7.8.

7.1. Data Processing

In the subsequent analysis of the experimental results, the data was processed based on several definitions and assumptions. First of all, the presented results are all based on the upstream conditions, because that represents the external conditions of an HLFC component, which are usually available during the design stage. Therefore, the pressure drop coefficient was scaled with the upstream density of the flow. Using the ideal gas law, Eq. (7.1), the density depends on the upstream temperature and pressure. The upstream temperature was recorded by the mass flow controller, and was assumed to be equal to the temperature upstream of the test section. The upstream pressure was not recorded, but was approximated by assuming that the ambient pressure at the pipe outlet plus the pressure drop across the sheet give the upstream pressure. This assumption requires that the viscous losses in the downstream pipe be negligible. In fact, the results from Sec. 7.2 demonstrate that this condition was valid. As an additional input, the ambient pressure was recorded at the start of every day whenever measurements were performed.

$$p = \rho R T \tag{7.1}$$

For defining the geometric parameters, they were selected based on the most restrictive side, because the flow must eventually pass through the narrowest opening regardless of the orientation of the perforated sheet. Generally, the laser exit side of the perforated articles was the most restrictive. The mean hole diameter was taken as the mean of each individual hole diameter on the most restrictive side. The open area ratio followed from Eq. (6.1) as the sum of the areas of each hole. The hole velocity was taken as the mean velocity through the holes, based on the open area ratio, using Eq. (5.9), which follows from the continuity equation. In turn, the mean pipe velocity was obtained from the mass flow rate, by dividing out the upstream value of the density and the area of the pipe. To obtain the Reynolds number, μ was evaluated using the Sutherland law, given by Eq. (7.2), where $\mu_0 = 1.716 \cdot 10^{-5}$ kg/(m·s), $T_0 = 273$ K, and $S = 111$ K [78]. The sheet thickness was obtained with a caliper as an average of multiple readings around the perimeter of each article.

$$\frac{\mu}{\mu_0} = \left(\frac{T}{T_0}\right)^{\frac{3}{2}} \frac{T_0 + S}{T + S} \tag{7.2}$$

7.2. Pressure Recovery

In order to ensure that the downstream pressure tap was located appropriately, as discussed in Sec. 6.1, an experimental investigation into the pressure recovery distance was performed. The sudden expansion behind

suction holes creates recirculation regions, which decreases the pressure level downstream of the perforated sheet. After some distance downstream of the recirculation regions, the flow redevelops into a pipe flow, where the pressure increases and settles at a constant level, which is the pressure recovery distance.

Literature suggests that the pressure recovery distance is governed by the number of holes in the perforated sheet. Generally speaking, the fewer holes, the longer the pressure recovery, as evidenced by the investigation performed by Singh and John Tharakan, who state that "[the] recovery of flow in multi-hole [perforated sheets] is faster compared to the single-hole orifice" [61]. This was because of better mixing with multiple holes [61]. In order to substantiate these observations, several results regarding the pressure recovery distance were collected from literature and summarized in Tab. 7.1.

Table 7.1: Pressure recovery distance as function of number of holes for various investigations from literature

Number of holes	Recovery	Type of fluid	Method	Source
1	~$8D$	Air	Experiment	Gan and Riffat [23]
1	~$4D$	Air	CFD	Gan and Riffat [23]
1	~$5D$	Water	CFD	Singh and John Tharakan [61]
3–52	$< 8D$	Water	Experiment	Malavasi et al. [39]
9	~$2D$	Water	CFD	Singh and John Tharakan [61]
25	~$1D$	Water	Experiment/CFD	Barros Filho et al. [5]
145	~$6d$	Air	CFD	Gan and Riffat [23]
∞	$7.5d$	Gaseous mix	CFD	Tseng and Li [70]
∞	$8d$	Air	CFD	Guo et al. [27]

The general trend indicated by Tab. 7.1 is that the pressure recovery region shrinks with an increasing number of holes, going from several pipe diameters (D) for few holes to the order of several hole diameters (d) for many holes. While the number and arrangement of holes affect the recovery on a case-by-case basis, the results serve to highlight the aforementioned trend, especially when comparing results from the same researchers with an increasing number of holes. Since the research concerns pipe flow, the presence of the wall affects the results significantly for a single hole, but its influence diminishes with more holes. In fact, the effect of the wall may be neglected when the number of holes exceeds 100–1,000 [70].

Based on the results presented in Tab. 7.1, the pressure recovery distance was investigated for the perforated article containing the fewest holes (19). This represents the worst-case scenario, because all other articles containing more perforations are expected to have a faster pressure recovery. Hence, if the location of the downstream pressure tap proves satisfactory for the worst case, it should also be valid for the other cases.

The pressure recovery was studied by measuring the static pressure at several positions downstream of the perforated article. This was done by inserting a static pressure probe 6 mm in diameter into the outlet pipe, as illustrated in Fig. 7.1. The probe was supported from above the exhaust, to prevent additional back pressure in the pipe. Downstream pressure measurements were taken between $1D$ and $6D$ from the perforated article. Positions between the sheet and $1D$ were not physically possible, because the probe would hit the sheet. For comparison, an additional measurement was taken with the pressure tap in the outlet pipe of the experimental setup, located at $2.32D$, while the probe was installed. The perforated article had an open area ratio of roughly 1%, representative of HLFC applications.

Results of the pressure recovery measurements are shown in Fig. 7.2. Here y denotes the position downstream of the perforated article, mirroring the convention from Fig. 5.1. The error bars indicate the uncertainty in the pressure measurements, which is detailed in Sec. 7.8. The variation in pressure is less than 0.3% over the range of downstream positions. Hence, it can be concluded that the pressure recovery has completed within $1D$ downstream of the sheet. In addition, it can be concluded that the influence of the friction inside the pipe is negligible. Combining these results validates the placement of the downstream pressure tap.

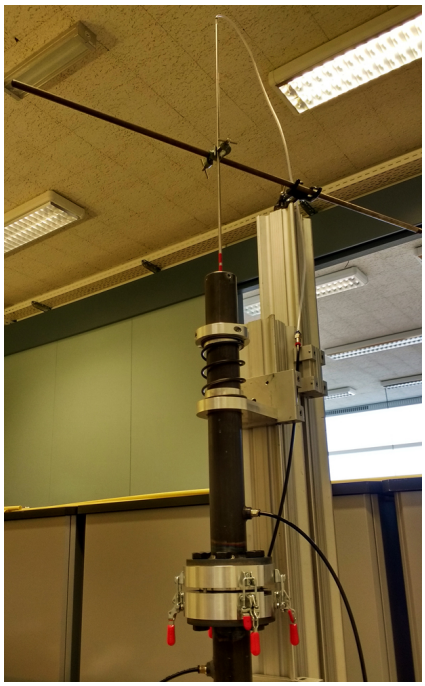

Figure 7.1: Experimental setup for measuring pressure recovery distance by inserting static pressure probe into outlet

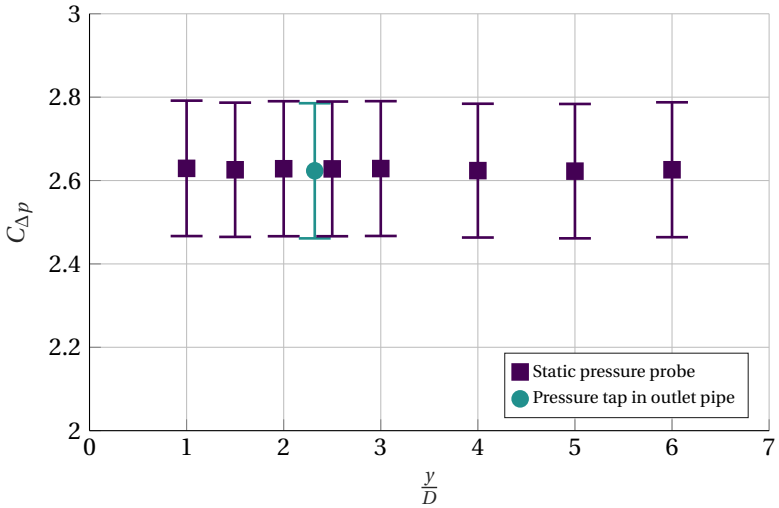

Figure 7.2: Pressure drop coefficient at several downstream positions. Tested at $Re_d = 1{,}551$, $\frac{t}{d} = 6.8$, $\beta = 1.0\%$, $N = 19$

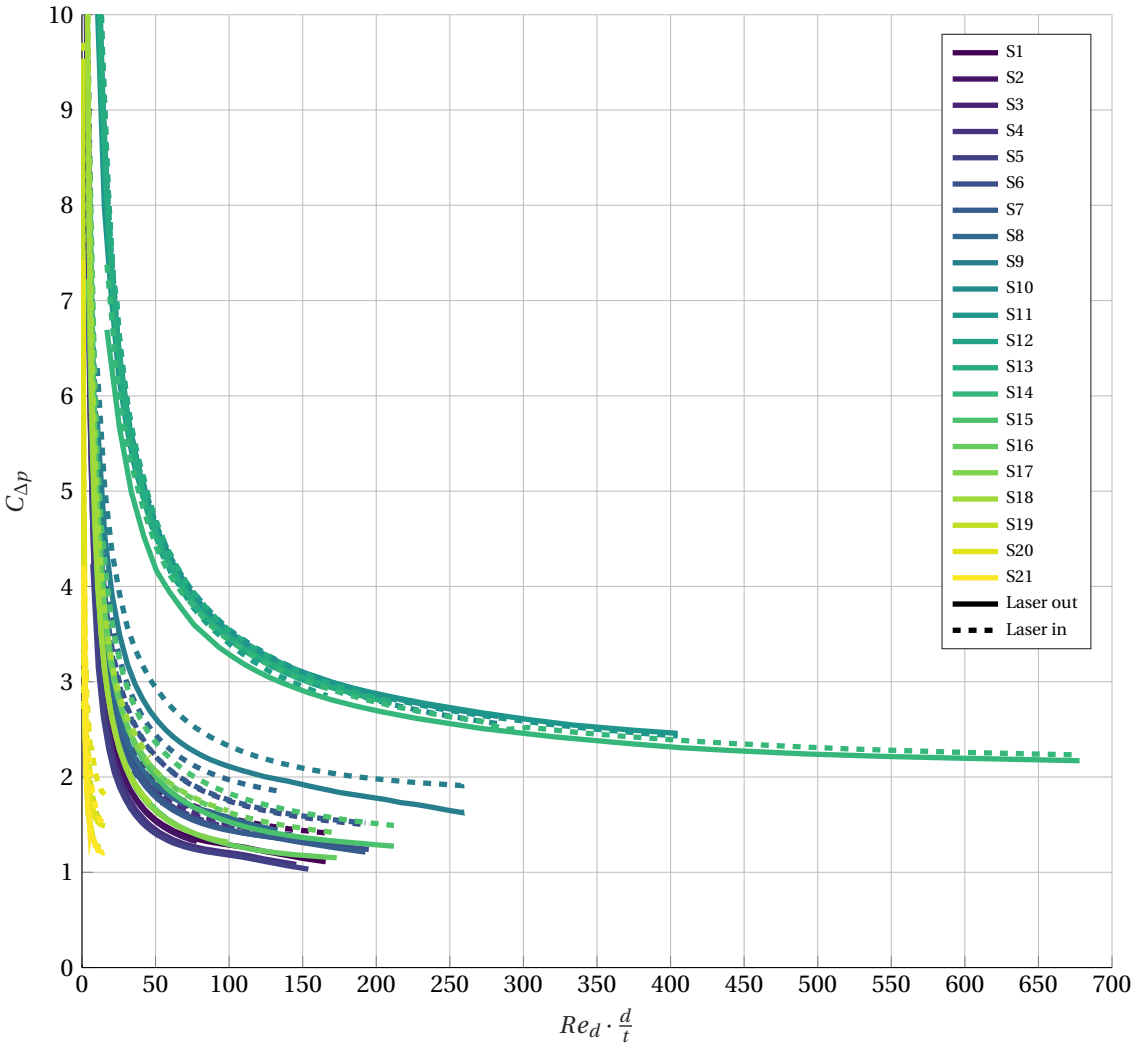

Figure 7.3: Pressure drop coefficient versus $Re_d \cdot \frac{d}{t}$ for all acquired data. Titanium articles clustered in far left, terminating within $Re_d \cdot \frac{d}{t} < 25$. Results presented for $M_h < 0.2$. Legend corresponds to Tab. 6.2

7.3. Complete Experimental Results

Flow measurements were performed for the entire experimental matrix of acrylic and titanium perforated articles, as discussed in Sec. 6.5. Results are presented in Fig. 7.3, in terms of $C_{\Delta p}$ versus $Re_d \cdot \frac{d}{t}$, in accordance with the model from Sec. 5.4. In order to avoid the influence of compressibility, results are shown up to a hole Mach number ($M_h = \frac{v_h}{a}$) of 0.2. This is clarified in Sec. 7.6.

Three distinct regions may be identified in Fig. 7.3. While most data is clustered in the central region, some perforated articles clearly fall out of this band. In fact, the articles with the greatest thickness and hole diameter are all grouped at a higher pressure drop coefficient than the others. On the opposite side of the test matrix, the titanium articles—with the smallest sheet thickness and hole diameter—all feature a rapid decrease in pressure drop coefficient at low $Re_d \cdot \frac{d}{t}$, placing them on the other side of the central band. Because the perforated articles that were most scaled up are located furthest away from the titanium articles, an apparent limitation to the scalability exists. This is investigated further in Sec. 7.7.

Another result observed in Fig. 7.3 is that the pressure drop coefficient is consistently higher when the laser entry side is facing the upstream flow. This is related to the difference in hole diameter on either side of the perforated articles. Apart from the largest-scale articles with $t \approx 8$ mm and $d \approx 1.2$ mm, the hole diameter on the laser exit side was smaller than on the laser entry side. This implies that a greater pressure

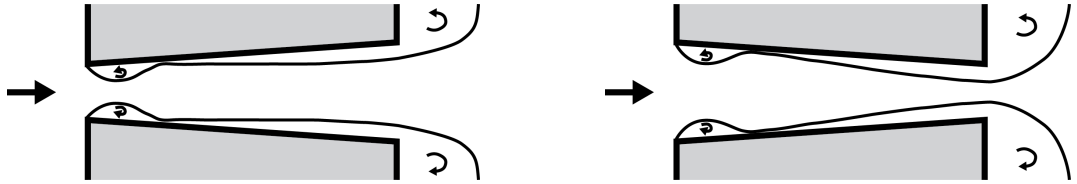

(a) Diverging hole (b) Converging hole

Figure 7.4: Effect of hole taper on development of inviscid streamline through a hole

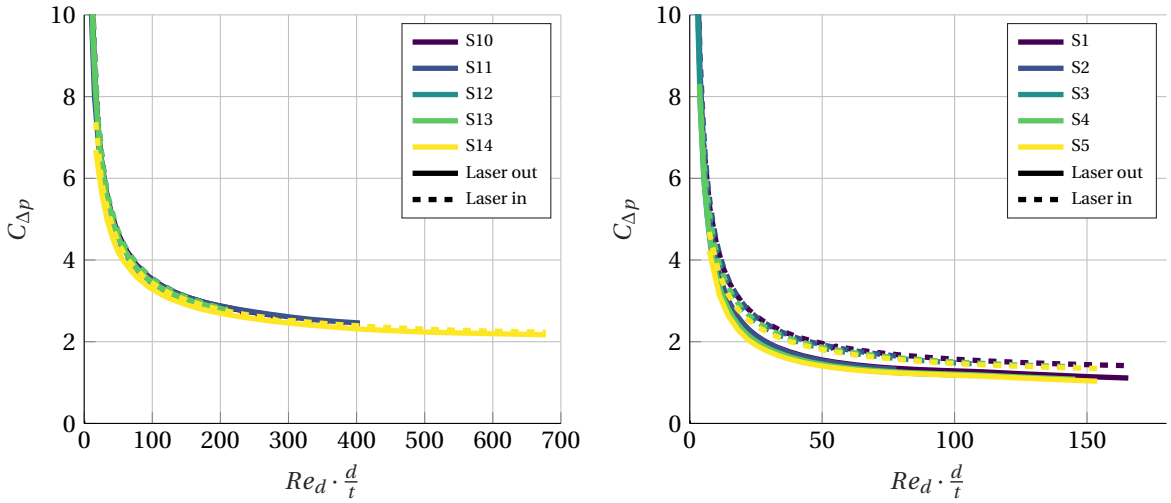

(a) Variation in β for $t \approx 8$ mm and $d \approx 1.2$ mm (b) Variation in β for $t \approx 3$ mm and $d \approx 0.3$ mm

Figure 7.5: Effect of varying open area ratio on pressure drop coefficient, keeping all other parameters constant. Legends correspond to Tab. 6.2

drop arises when the flow passes through a converging hole, as opposed to a diverging hole. This result was also reported in [80]. A possible explanation to this behavior is illustrated in Fig. 7.4, which schematically shows the development of the inviscid streamline through a hole. At the hole entrance, the flow separates but later reattaches when $\frac{t}{d}$ is sufficiently large. Then a boundary layer starts to grow, which creates a restriction for the core jet flow. For a diverging hole, the boundary layer has little effect on the pressure drop, because it does not restrict the core flow significantly. However, the boundary layer has a significant influence for a converging hole, because it is thickest at the narrowest section of the hole, creating a greater restriction for the core flow. As a result, the pressure drop increases.

7.4. Effect of Open Area Ratio

The influence of the open area ratio was assessed by means of two sets of perforated articles, each having nearly constant geometric properties, except for the number of holes, and therefore, β. The experimental results are shown in Fig. 7.5. Both figures seem to indicate no dependency of $C_{\Delta p}$ on β, since the results from different articles collapse onto the same curve. However, this is exactly the intended result, because the influence of β is absorbed in the definition of the pressure drop coefficient, as given in Eq. (5.1). So, while the nondimensional $C_{\Delta p}$ is independent of β, the dimensional pressure drop depends strongly on it.

Figures 7.5a and 7.5b highlight the effect of the hole taper. The largest-scale perforated articles, presented in Fig. 7.5a, had nearly the same hole diameter on either side of the sheet, and are therefore not affected by the orientation of the sheet. On the other hand, the smaller-scale articles from Fig. 7.5b feature tapered holes, so the resulting pressure drop depends on the orientation of the sheet, as illustrated by Fig. 7.4.

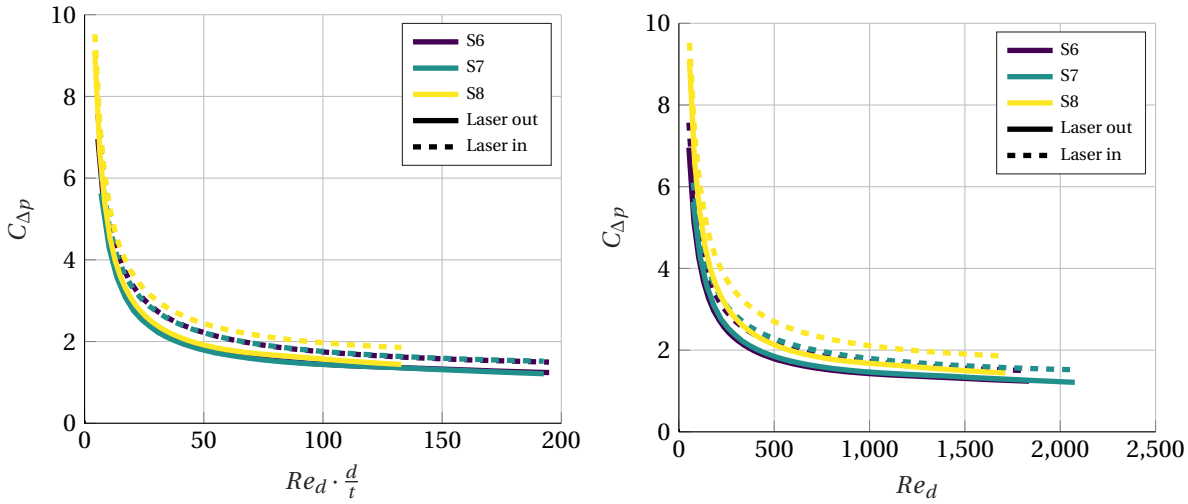

(a) Taking $\frac{t}{d}$ into account in Re_d

(b) Not taking $\frac{t}{d}$ into account in Re_d

Figure 7.6: Effect of $\frac{t}{d}$ on pressure drop coefficient. Legends correspond to Tab. 6.2

7.5. Effect of Hole Aspect Ratio

The flow pattern through and behind a hole is strongly affected by the aspect ratio of the hole: $\frac{t}{d}$. For a thin perforated sheet, the flow into the hole that separates around the edges does not reattach within the hole, as discussed in Sec. 5.1. On the other hand, reattachment inside the hole does occur in thick sheets, with an aspect ratio greater than 1–2. Consequently, the inertial pressure losses are largely unaffected by the thickness of the sheet when $\frac{t}{d} > 2$ [23, 27], which is the typical domain of HLFC components.

Instead, $\frac{t}{d}$ affects the frictional losses inside the hole. The longer the hole in terms of $\frac{t}{d}$, the greater the pressure loss, as indicated by Eq. (5.7). In fact, the influence of $\frac{t}{d}$ on the viscous losses is accounted for when the viscous losses, governed by Re_d, are combined with the hole aspect ratio to form the parameter $Re_d \cdot \frac{d}{t}$, as was cited in [14, 26]. The experimental results, presented in Fig. 7.6, confirm the use of the parameter $Re_d \cdot \frac{d}{t}$ to account for the effect of the aspect ratio of the hole. The experimental matrix contained two articles having the same hole pattern drilled into two different thicknesses, thereby creating articles with a $\frac{t}{d}$ of 9.4 and 12.9, with all other parameters being virtually identical. When $\frac{t}{d}$ is not taken into account, like in Fig. 7.6b, the experimental results for these articles do not fall onto the same curve. However, taking $\frac{t}{d}$ into account, as like Fig. 7.6a, collapses the curves of these articles onto each other.

The use of $Re_d \cdot \frac{d}{t}$ is further supported by the results presented in Fig. 7.7, containing several articles with a spread in $\frac{t}{d}$ but also a variation in other geometric parameters. Despite this variation, the influence of $\frac{t}{d}$ is properly accounted for, as the data falls onto nearly the same curve.

7.6. Effect of Compressibility

For some perforated articles, their combination of open area ratio and the tested flow rate was such that the Mach number inside the holes became relevant for compressibility effects. While the Mach number is a similarity parameter (Sec. 5.2), the scope of the present research is to investigate the scalability of suction surfaces with respect to geometric properties. Consequently, the effect of compressibility is not studied.

However, the dependency of the results on the Mach number was assessed, in order to identify the part of the results that may be considered to be incompressible. Using Fig. 7.8, it can be seen that the pressure drop coefficient starts to increase after a certain Mach number has been reached. Between M_h of 0.2–0.3, the pressure drop coefficient starts to gradually increase as a consequence of compressibility. Some articles start to exhibit compressibility effects at lower M_h than others, especially the titanium articles. This may be due to the relatively large spread in hole diameter for the titanium articles. The large spread implies that there were some extremely small holes with a larger flow velocity than the mean, which could have promoted compress-

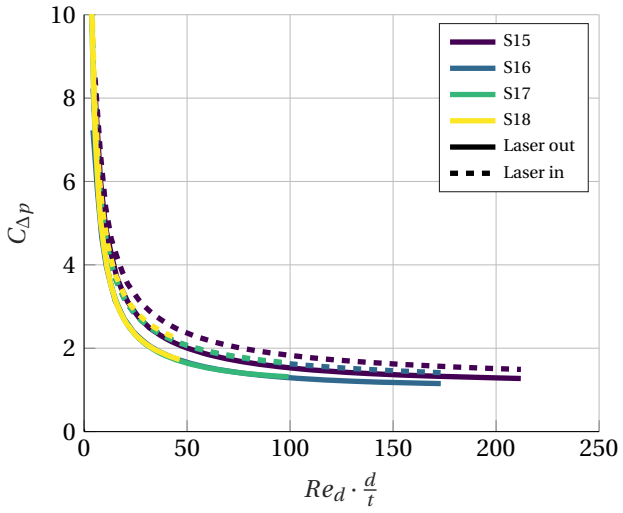

Figure 7.7: Effect of $\frac{t}{d}$ on pressure drop coefficient for sheets with various t and d. Legend corresponds to Tab. 6.2

ibility effects at lower mean Mach numbers.

Accounting for the differences between articles, a general limit of $M_h = 0.2$ was taken as the limit for incompressible flow. The following investigation into the scalability of the experimental results uses only the data up to $M_h = 0.2$, in order to avoid any bias from dissimilar Mach numbers.

7.7. Scalability of Results

Evident from Secs. 7.4 and 7.5, the experimental results for the pressure drop coefficient generally behave in agreement with the expected, theoretical dependency on β and $Re_d \cdot \frac{d}{t}$, as was discussed in Sec. 5.4. However, the experimental results from Fig. 7.3 showed a clear distinction between the small-scale titanium articles and the large-scale acrylic articles. This warrants an investigation into the scalability of the results.

Because the dependency of the experimental results on the similarity parameters behaved as expected from the theoretical model, the differences due to the scale of the perforations will be assessed from the point of view of the constants A and B that appear in Eq. (5.8). A governs how quickly the pressure drop coefficient drops off and tends towards the constant value B. As illustrated by Fig. 7.3, the asymptotic value of $C_{\Delta p}$ was largest for the largest-scale acrylic articles. In fact, there appears to be a direct correlation between the final value of $C_{\Delta p}$, represented by B, and the diameter of the hole. With a large diameter, the number of holes is small, so both the hole diameter and the number of holes have an influence on B.

The dependency on the number of holes was also observed for the pressure recovery length in Sec. 7.2. The pressure recovery distance depends on the recirculation regions behind the perforated sheet. B represents the entry and exit losses, and is therefore also related to the recirculation regions behind the sheet. Hence, it is not surprising that a dependency of B on the number of holes is observed.

For a given hole diameter, a sheet with a higher open area ratio contains more holes. In order to isolate the effect of scale, the number of holes (N) is divided by the open area ratio to yield the parameter $\frac{N}{\beta}$. It represents the number of holes per unit of open area. The behavior of B with $\frac{N}{\beta}$, presented in Fig. 7.9, shows an interesting trend: with increasing $\frac{N}{\beta}$, B decreases and eventually settles at a constant value. In fact, the trend fits a power law with a constant offset. The steady-state value of B is approximately 0.5–0.6, which is slightly less than the estimate of 0.75 found in Sec. 5.4.

The constant value for B is reached at approximately $\frac{N}{\beta} > 10{,}000$. This implies that a sufficient number of holes is required to accurately predict the inertial pressure losses for a perforated sheet. The results for the titanium articles agree well with the acrylic articles for which $\frac{N}{\beta} > 10{,}000$, although B seems slightly high for

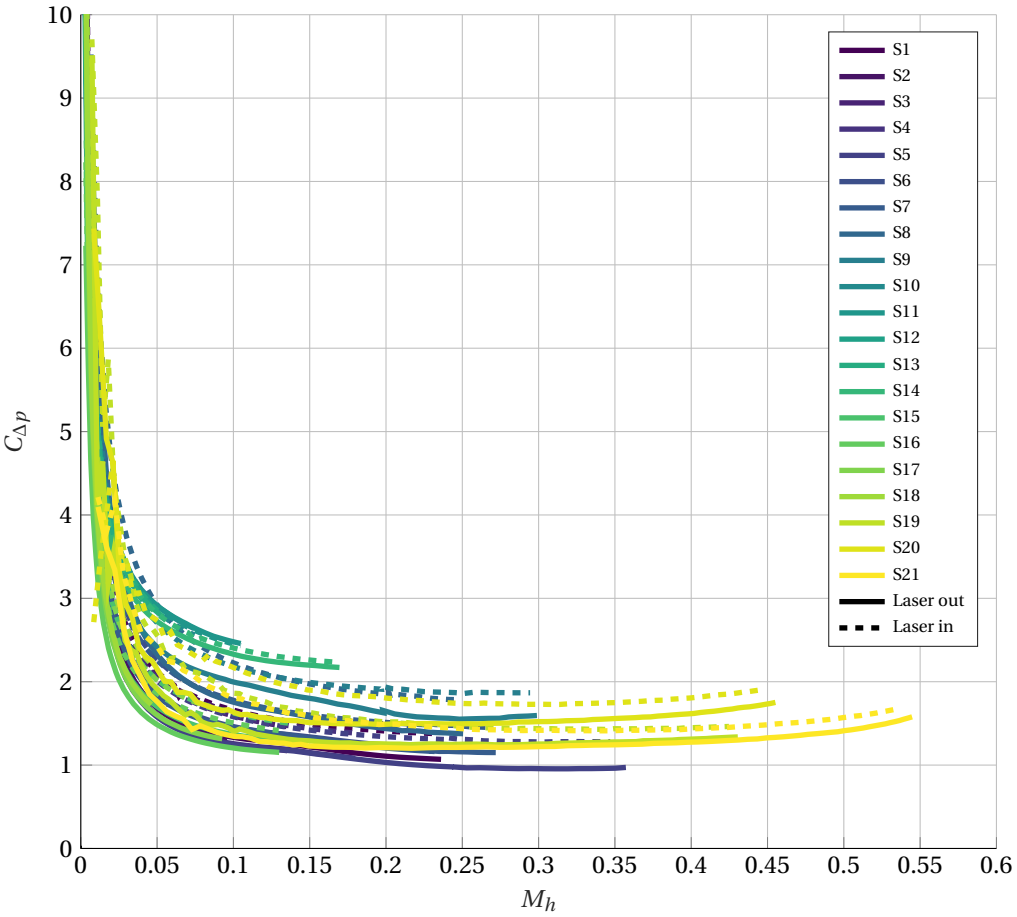

Figure 7.8: Effect of Mach number inside holes on pressure drop coefficient. Legend corresponds to Tab. 6.2

the titanium articles, likely due to the relatively large uncertainty on the open area ratio. Furthermore, Fig. 7.9 shows the effect of the orientation of the sheet, exhibiting higher pressure drop for converging holes.

The parameter $\frac{N}{\beta}$ may also be thought of as a measure of how well the perforated sheet mimics a perforated sheet of infinite size. For the pressure drop across an infinite perforated sheet, there is no influence of the walls of the experimental setup. The limit on $\frac{N}{\beta}$ before a steady value is reached therefore represents the point at which the influence of the wall-bounded flow in the experimental setup is negligible. The link with the experimental setup can be illustrated by substituting the definition of β, as given in Eq. (6.2), which shows that $\frac{N}{\beta}$ is roughly equivalent to $\left(\frac{D}{d}\right)^2$. The limit of $\frac{N}{\beta} > 10{,}000$ corresponds to $\frac{D}{d} > 100$, which is to say that the hole diameter should be at least two orders of magnitude smaller than the diameter of the pipe in order to mimic an infinite perforated sheet. However, this limit is specific to the experimental setup, because a different pipe diameter also affects the number of holes in a perforated plate, given the same β. Therefore, this condition is not generally applicable.

Because of the link between B and the recirculation regions behind the sheet, the dependency of B on $\frac{N}{\beta}$ should be argued through the behavior of the recirculation regions with $\frac{N}{\beta}$. At low $\frac{N}{\beta}$, there are few holes for a given open area ratio. The recirculation regions behind the sheet will therefore be relatively large, causing larger pressure losses. At higher $\frac{N}{\beta}$, there are many small holes closer together, which break up the recirculation regions behind the sheet, thereby reducing the pressure losses. The exit losses settle at a constant value, because the increase in the number of holes balances the reduction in intensity of each recirculation region.

For the coefficient A, a similar dependency on the parameter $\frac{N}{\beta}$ was observed, as illustrated in Fig. 7.10. Again, the trend fits a power law and the effect of hole taper is clearly visible. However, contrary to B, which

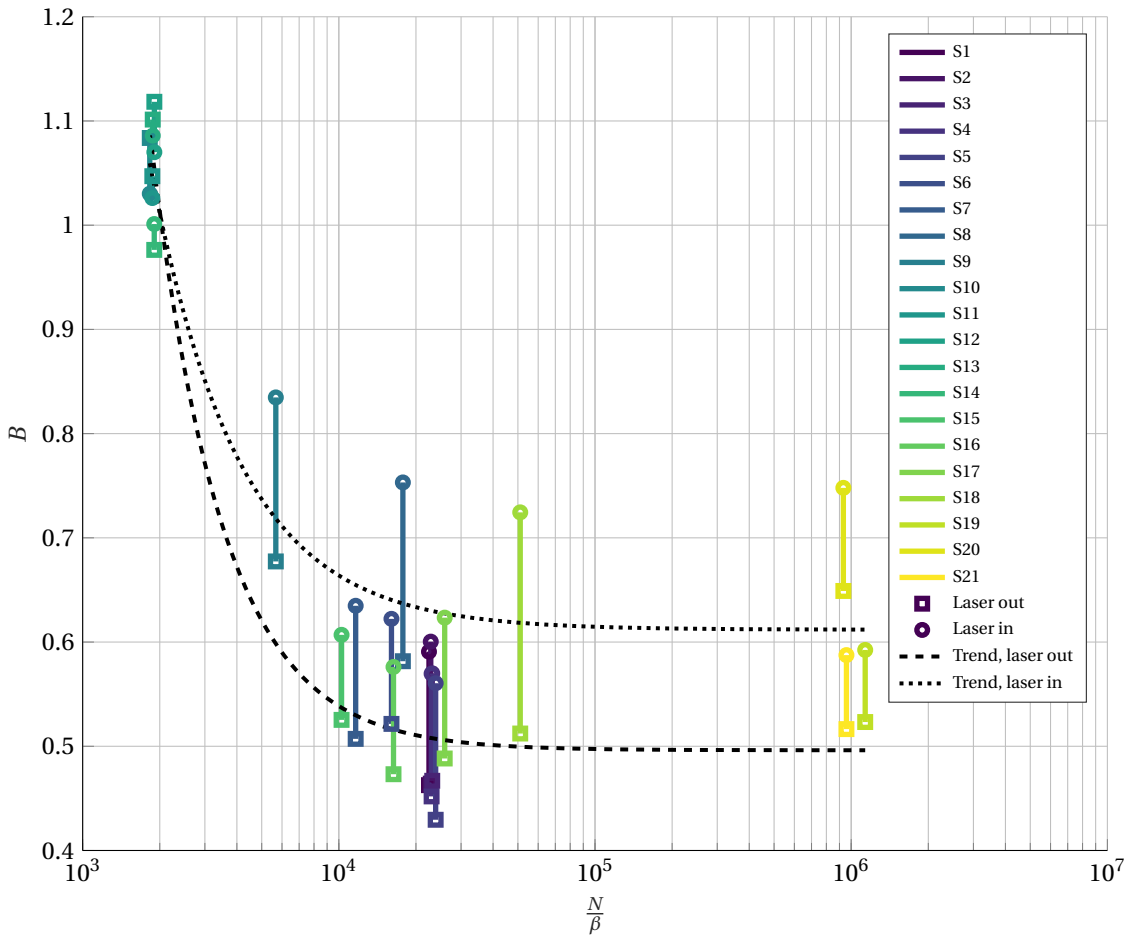

Figure 7.9: Scalability of B, representing inertial losses, expressed as a function of $\frac{N}{\beta}$ including power law trend lines on laser entry and exit sides. Legend corresponds to Tab. 6.2

settled at a constant value, A seems to continue decreasing with $\frac{N}{\beta}$. This implies that the frictional losses inside the holes reduce for a sheet with many small holes, compared to a sheet with few, larger holes.

A limitation of the scaled acrylic articles is therefore that the frictional losses are overpredicted compared to the titanium articles representative of typical HLFC components. However, the frictional losses are only relevant at low flow rates. So, the scale of the perforated article is important for an accurate estimation of the pressure drop at low flow rates, but not at high flow rates, provided that there are sufficiently many holes.

The validity of the experimental results was assessed by means of a comparison with literature. It was desired to compare the results with those obtained by Young et al. in [80], because they also performed flow measurements of the pressure drop across a perforated titanium sheet with typical properties of an HLFC component. However, not all test conditions are clear, so unfortunately the data cannot be represented in a nondimensional way. If atmospheric conditions at room temperature are assumed, poor agreement with the present experimental results is found. Other data was extracted from [67], where experiments were performed on perforated sheets with many holes and $\frac{t}{d}$ of about 2. The resulting estimates for A in the order of 10 and B between 0.25 and 0.7 agree with the present results. This is the only source from which A could be estimated, making it a valuable result. In addition, A was found to be decreasing with more holes, which is what the experimental results from Fig. 7.10 also suggest.

Further estimates of the value of B could be obtained from other references. Malavasi et al. tested the pressure drop across multiple perforated sheet, but mainly at low $\frac{t}{d}$ and in turbulent conditions [39]. Still, for the highest $\frac{t}{d}$ of 1.4, B of around 0.5 could be extracted, in agreement with the present results. Further data

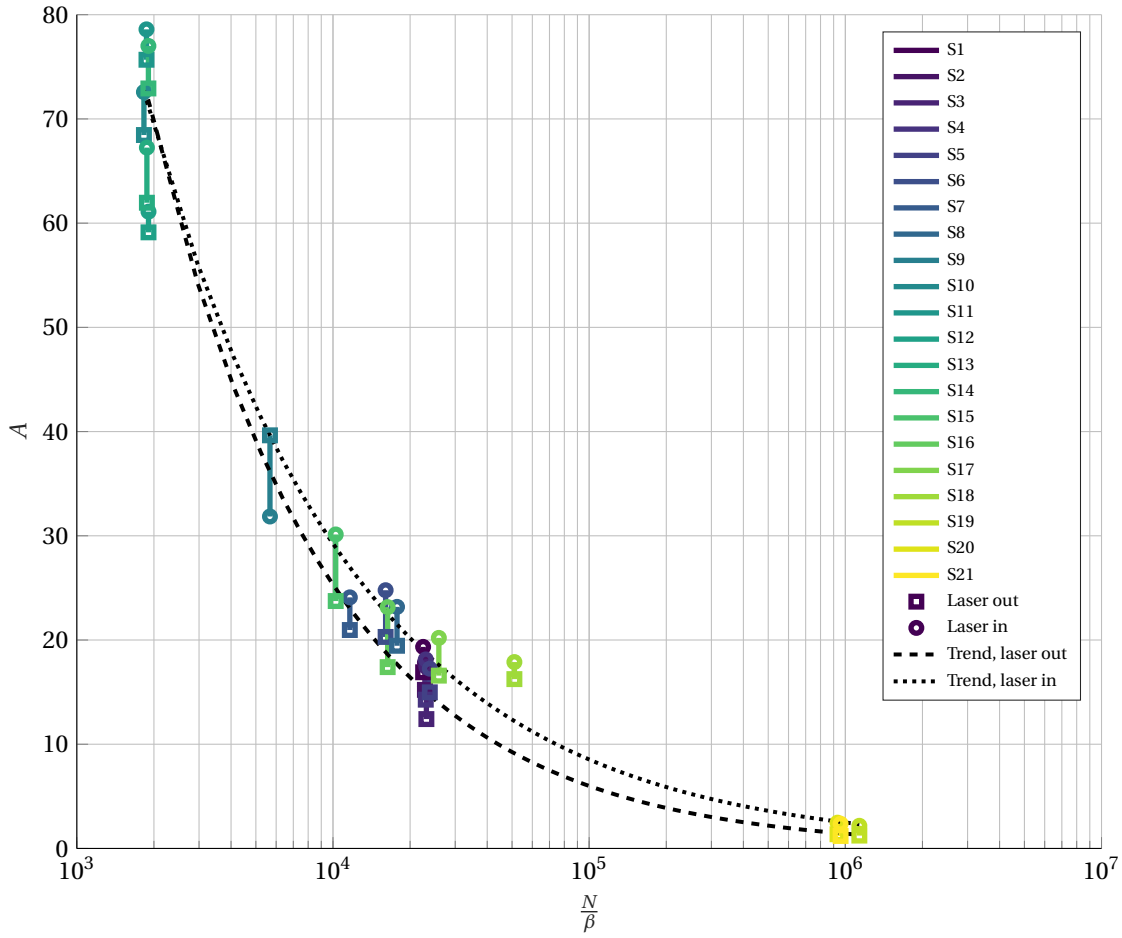

Figure 7.10: Scalability of A, representing frictional losses, expressed as a function of $\frac{N}{\beta}$ including power law trend lines on laser entry and exit sides. Legend corresponds to Tab. 6.2

was obtained from [5], from which B was estimated between 0.25 and 0.4 for $\frac{t}{d}$ around 2. The caveat here is that a square duct was used, as opposed to a circular pipe, which could have affected the pressure drop. Finally, Maynes et al. report B between 0.25 and 0.5 for $\frac{t}{d} > 3$ in turbulent conditions [40]. Given that the present research found values for B of around 0.5 to 0.6, the results seem trustworthy.

7.8. Uncertainty Quantification

Uncertainty in the experimental results originates from measurement uncertainty, instrument accuracy, and uncertainty due to the experimental setup. Three parameters were measured, namely the pressure drop, the mass flow rate, and the flow temperature. The pressure drop was measured using two different sensors, each with their own accuracy. The mass flow controller recorded both the flow rate and temperature.

Measurement uncertainty was restrained by performing a large number of measurements. For each data point, 100 samples were taken at an acquisition frequency of 5 Hz, and then averaged. Besides the standard deviation in the measurements, the instruments used for measuring have their own accuracy. The primary pressure sensor (Sec. 6.1) has an accuracy of ±0.25% of the full scale of ±60 kPa, as reported by the manufacturer. The secondary pressure sensor is more accurate, with an accuracy of ±0.03% of the full scale of -1 to 6 kPa, as reported by the manufacturer. The mass flow controller has a reported accuracy of ±0.5% of the reading and ±0.1% of the full scale. The full scale is 260 standardized liters per minute, which could be converted into 0.0056 kg/s.

Further uncertainty is introduced from the geometric properties of the perforated articles. The uncertainty in the hole diameter and open area ratio is indicated in Fig. 6.11, but is defined differently for the

acrylic and titanium articles due to the way in which the geometric properties were measured. For the acrylic articles, all holes were measured using the optical setup. Each hole size was individually calibrated using the process described in Sec. 6.4, which accounts for errors in the optical setup. This error also propagates into the estimated open area ratio. However, since all holes were measured, the open area ratio could be determined exactly, barring the calibration uncertainty. The spread in diameter among holes is therefore not relevant for the open area ratio. For the titanium articles, a subset of holes was measured with a microscope, from which the mean hole diameter was obtained. The open area ratio was inferred from the mean hole diameter and the number of holes. However, the size of each hole was unknown, so the spread in diameter propagates into the estimated open area ratio as an uncertainty. On the other hand, no calibration was required, eliminating calibration uncertainty.

The uncertainties from all measured parameters were propagated into the final results for $C_{\Delta p}$ and $Re_d \cdot \frac{d}{t}$, as described in App. C. The confidence bounds on the experimental results for the acrylic articles are shown in Fig. 7.11. For clarity, only the laser exit side is shown, but the laser entry side had comparable results. For most articles, the uncertainty ranges between 5% and 12% at high flow rates, when $C_{\Delta p}$ approaches a constant value. The uncertainty increases at low flow rates because the accuracy of the pressure sensor and the mass flow controller become large compared to the measured pressure drop and flow rate, respectively.

The largest source of uncertainty is the uncertainty in the open area ratio. In fact, it originates from the calibration procedure. This uncertainty could most readily be reduced by performing microscope measurements of additional holes. In doing so, the spread in the fit on the calibration data (see Fig. 6.9) could be reduced. While the spread would be reduced, the calibration itself, and therefore the results presented in this chapter, would likely not be significantly affected, because the obtained results fall within the expected behavior, indicating that the present calibration is accurate. Therefore, the uncertainty is deemed acceptable.

The uncertainty in the results of the titanium articles is large, which is almost entirely due to the uncertainty in the open area ratio. This can be attributed to material properties and laser settings which were still being fine-tuned at the time of manufacture. It was found that the hole diameter was in the order of the grain size of the material. Both factors contributed to a significant share of blind holes and a large general variation in the hole diameter. Therefore, it would be desirable to perform measurements with additional perforated articles with industry-scale dimensions, like the titanium articles tested here.

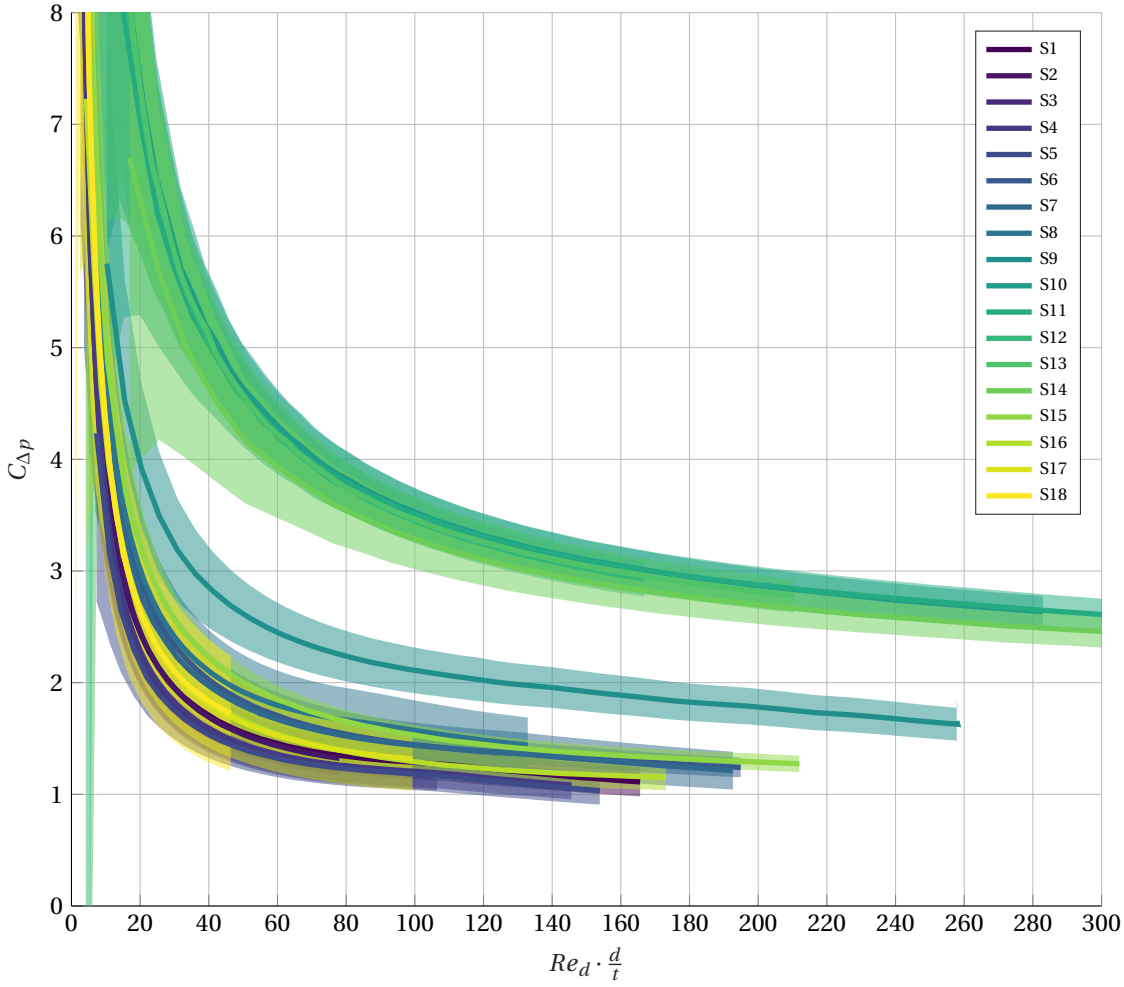

Figure 7.11: Uncertainty bounds (1σ) on experimental results for acrylic perforated articles, showing laser exit side only. Legend corresponds to Tab. 6.2

8

Conclusion and Recommendations

The research objective was to expand the capability to perform the aerodynamic design of a suction-type HLFC component with two key developments: incorporating boundary layer transpiration in an existing transition prediction tool and investigating the scalability of pressure losses across perforated sheets. Section 8.1 summarizes the findings from this report, and reflects on the degree with which the objective was reached. Additionally, Sec. 8.2 provides recommendations to extend this research.

8.1. Conclusion

Hybrid laminar flow control was identified as a means to prolong the extent of laminar flow. It combines an active solution and passive airfoil shaping to yield a system less complex than a full active system. Meanwhile, HLFC enables most of the benefits of a full active system, at a fraction of the required power. HLFC using boundary layer suction was found to be the most technologically mature solution for a transonic transport aircraft. In fact, suction is required on a swept wing to control the two prime instabilities of a laminar boundary layer: Tollmien-Schlichting waves and the cross flow instability. While the streamwise TS instability exists on any wing, the CF instability only occurs on swept wings.

The practical concerns of HLFC technology were addressed next. HLFC is most suited for the wing, the tail surfaces, and the nacelles. Important for suction-type HLFC is the critical suction limit, which is the suction rate at which the streamwise vortices behind a suction hole become unstable. Preventing this requires tiny suction holes. Furthermore, insect contamination should be prevented, for example using a Krueger flap or by continuously injecting a fluid around the leading edge. The latter solution can simultaneously serve as an anti-icing system. Thermal anti-icing is another option. Practical examples have demonstrated the feasibility of HLFC in flight tests, for example on the wing of the Boeing 757 and the fin of the Airbus A320. However, these systems were too complex and heavy for a net benefit. More recently, Boeing has found a way to commercially implement a passive HLFC solution on the tail surfaces of their 787-9 model.

The aforementioned challenges of HLFC have been investigated by researchers at TU Delft. First of all, researchers have focused on reducing suction pump requirements by optimizing the location where suction is applied. A second research area was the design of creative HLFC solutions in order to reduce its complexity. Finally, investigations into the critical suction limit have been performed.

The following part of the report documented the incorporation of boundary layer transpiration into a transition prediction tool. First, transition prediction methods were reviewed. Linear stability theory combined with the e^N-method was found most suitable, as it strikes a balance between computational time and accuracy. Subsequently, the governing equations for the base flow and the stability analysis were presented. The existing transition prediction tool comprises a boundary layer solver and a stability solver that follow these governing equations. However, modifications were required for use with transpiration.

Within the boundary layer solver, the no-penetration boundary condition was adapted to allow transpiration. Additional inputs to the solver were required, namely a suction distribution. This input was given its

own discretization, thereby allowing suction distributions to be defined independent of the discretization of the outer flow variables, which generally uses comparatively few points. The subsequent internal interpolation of the suction distribution was created such that it accounts for the location of the stagnation point.

Modifications to the stability solver itself were not required, as its boundary conditions remain valid with transpiration. However, suction was found to be incompatible with the preprocessing algorithm of the stability solver. For the TS instability, the solution grid in the disturbance parameter space was negatively affected by suction. This grid is determined using an estimation of the neutral curves of the boundary layer solution. Suction was found to have too much a stabilizing effect on these curves, which prevented the complete enclosure of all unstable frequencies. Furthermore, the propagation of N-curves through stable regions was hindered. This was remedied by treating the boundary layer properties as if the influence of suction was not there, thereby causing the solution to appear less stable. In turn, the resulting grid was suitable to capture the necessary stability behavior.

The modifications to the boundary layer solver were verified and validated, using cases ranging from flat plates to a swept wing. All relevant characteristics for HLFC on a transonic aircraft were covered, namely pressure gradient, sweep angle, and suction. Overall, excellent agreement was found between the present results and references. Hence, the boundary layer solver is fully suited for analysis with transpiration.

The stability solver was validated using two cases, one for which N-curves obtained with linear stability theory were available, and another which featured a sweep angle so the CF component could be tested. For the first case, the N-curves obtained presently showed good agreement with the reference. The observed differences could be attributed mainly to the selection of instability modes. For the second case involving CF, the observed behavior was in agreement with expectation, given the pressure distribution. The influence of suction was clearly visible. This case also showed that no modification were required for the preprocessor for the CF instability. For both cases, the modified preprocessor produced suitable grids for the TS instability. Analysis with more cases may be required to ensure general applicability, but the present results are satisfactory and should extrapolate to most general cases. Given the solid results obtained for both solvers, the modified transition prediction tool can be used to study stability on HLFC components.

However, there are some limitations of the present implementation of the transition prediction tool. For instance, compressible flow was not yet implemented, which is a relevant element of transonic flow. In addition, no investigation into establishing the critical N-factor with suction has been performed in this research. This is required before the tool can be used to predict transition for HLFC components, but it remains a tricky question, as was highlighted in the literature summarized in this report. For example, it is unclear whether the critical N-factor remains the same with suction. Moreover, it could be dangerous to trust the stability analysis if N is not monotonic.

The remaining part of the report presented the experimental investigation into the scalability of the pressure drop across perforated sheets. A perforated sheet is the core element of a suction-type HLFC component, which is why a good estimate of the pressure drop is essential and has the broadest applicability. The present research neglected tangential flow and focused on the primary pressure loss originating from the perpendicular flow through a perforated sheet. This simplifies the problem by reducing the number of governing parameters. Generally, the pressure drop, represented by the pressure drop coefficient ($C_{\Delta p}$), is a function of the following nondimensional parameters: the open area ratio (β), the ratio of sheet thickness to hole diameter ($\frac{t}{d}$), and the hole Reynolds number (Re_d). Typical values of these similarity parameters for HLFC applications were collected from literature. This information was used to design the experimental matrix.

The experimental setup consisted of a pipe, within which a perforated sheet was placed in a perpendicular orientation. A matrix of perforated articles was manufactured out of laser-drilled acrylic sheets. These articles mimicked the typical nondimensional similarity properties of HLFC surfaces, but featured a broad range of dimensional properties, to enable an assessment of the influence of scale. The geometric properties of these articles were measured using an optical setup, which consisted of a camera and a light table. Individual hole properties were found using a boundary recognition algorithm. The benefit of this setup was that all holes were captured in a single image. In order to account for errors, the optical setup was calibrated with separate measurements of individual holes taken with a microscope. Besides the 18 acrylic articles which

were all scaled up with respect to typical HLFC components, three perforated titanium articles were produced at the characteristic scale of HLFC.

The experimental results were collected and presented in terms of the similarity parameters. The influence of β was fully absorbed in the definition of $C_{\Delta p}$. Furthermore, the effect of $\frac{t}{d}$ was accounted for by plotting the results as a function of $Re_d \cdot \frac{d}{t}$, as was suggested in literature. An additional observation was that a converging hole consistently created a higher pressure drop than a diverging hole.

While the influence of the similarity parameters followed expectation, the experimental results suggested a definite effect of the scale of perforated sheets: curves of $C_{\Delta p}$ were generally grouped, but the articles with the smallest and largest hole diameter were furthest apart. The scalability was assessed with a model for the pressure drop, which uses term linear and quadratic in the hole velocity. When converted to nondimensional form, only the coefficients A and B remain, which respectively describe the frictional losses inside holes and the entry and exit losses. It was found that the influence of scale was related to the number of holes in a perforated article. In particular, the number of holes per unit of open area ($\frac{N}{\beta}$) indicated the effect of scale. Both A and B fit a decaying power law trend with $\frac{N}{\beta}$. With increasing $\frac{N}{\beta}$, B decreased until reaching a steady value of around 0.5–0.6. This value was reached when $\frac{N}{\beta}$ exceeded a certain limit, which implies that a sufficient number of holes is required to represent an infinite perforated sheet. The limit is expected to vary depending on the experimental setup. On the other hand, A was found to continually decrease with $\frac{N}{\beta}$. So, the frictional losses inside holes seem strongly dependent on scale, while the entry and exit losses are independent of it, provided that the number of holes is sufficient.

For the design of HLFC surfaces, this implies that a perforated sheet can be scaled up for high flow rates, because B is dominant then, but the scalability at low flow rates is limited, when A is dominant. Typically, HLFC operates at low flow rates, which gives a low Re_d when combined with the typically small hole diameter. This puts HLFC in the domain where A is relevant, and so the perforated sheets should not be scaled up significantly to accurately capture the frictional losses. For now, the pressure drop characteristics of HLFC components will likely still need to be determined experimentally. However, further experimental research with industry-scale perforated sheets could provide a better estimate of A.

8.2. Recommendations

Estimating the critical suction limit was outside the scope of the present research, but remains a goal for the practical design of HLFC components. The critical suction limit has not been quantified for multiple rows of holes. Yet, MacManus and Eaton demonstrated that their parameter is applicable for the critical suction limit for multiple rows of holes. However, further experimental research will be required to estimate it. A potential next step could be to evaluate the streamtube parameter from MacManus and Eaton with the data presented in [67]. Another step could be to incorporate the streamtube parameter into the boundary layer solver.

Further developments to the transition prediction tool can be made, for example the extension to compressible flow. Compressibility is an important aspect of transonic flow and therefore should be included in a design tool for HLFC. Another option would be to test other stability solvers with the application of suction, for example PSE theory.

The literature study demonstrated that two options for specifying the suction distribution were desired. The option of the direct input of the suction distribution was implemented in the present work, but the indirect input can be implemented at a later stage. For this option, the suction distribution would be determined according to the layout of the internal suction system and the pressure difference across the surface. However, this would require a good model linking the suction rate to the pressure drop, for which a start was made with the present experimental research. Further experiments would be required to achieve a more conclusive assessment of the scalability of pressure losses. In addition, tangential flow would have to be considered for the design of an HLFC component, which introduces additional similarity parameters and an additional pressure loss. This was not studied in the present work.

The modified boundary layer solver and stability solver were verified, such that they can be used to study stability on HLFC components. The next step would be to collect or perform experimental research with

which the critical N-factors with suction can be evaluated. This input is required before predictions of the transition location on HLFC components can be made.

Further validation of the modified solvers would be beneficial, especially for the preprocessing in the stability solver, because it includes solution-dependent modifications. Additional cases can help fine-tune the procedure. Furthermore, the current modifications to the preprocessing of the stability solver were not based on the suction rate. Since the effect on boundary layer stability increases with the suction rate, it could be worth investigating whether a relation can be found between the suction rate and the required modification of the instability grid. As found in the literature study, a new test case for transition prediction tools was proposed in [55]. Further developments have not been found, but it would be worth following its progress.

Regarding the experimental study performed in this report, obtaining more data of small-scale articles would be helpful to study the behavior of especially the frictional losses for sheets containing many small holes. This data would help to substantiate the findings of the present work and the prediction of the pressure losses across an actual HLFC component.

For the experimental results obtained here, the largest source of uncertainty was the calibration of the optical method. This uncertainty could potentially be reduced by taking measurements of additional holes with the microscope.

The present experimental matrix contained few articles to study only the effect of $\frac{t}{d}$. This was due to the difficulty of manufacturing perforated articles with high $\frac{t}{d}$, in the typical range of HLFC components. This was also why the test matrix focused on the lower practical limit of HLFC, namely 10. However, given that the inertial pressure losses across perforated sheets do not vary much from $\frac{t}{d} > 2$, it would have been possible to obtain equally representative results with articles with a reduced hole aspect ratio compared to typical HLFC components. Moreover, even when accounting for some safety margin, manufacturing articles with $\frac{t}{d}$ around 4 would be much easier to manufacture than at $\frac{t}{d} = 10$. The downside would be that having a lower $\frac{t}{d}$ would imply higher $Re_d \cdot \frac{d}{t}$, which would therefore more quickly go outside of the domain of typical HLFC components (From Tab. 5.1: $Re_d < 300$, $\frac{t}{d} > 10 \Rightarrow Re_d \cdot \frac{d}{t} < 30$).

Bibliography

[1] C. Abegg, H. Bippes, and F. P. Bertolotti. On the application of suction for the stabilization of crossflow instability over perforated walls. In W. Nitsche, H. J. Heinemann, and R. Hilbig, editors, *New Results in Numerical and Experimental Fluid Mechanics II*, volume 72 of *Notes on Numerical Fluid Mechanics*. Vieweg, Braunschweig/Wiesbaden, 1999.

[2] D. Arnal. Description and Prediction of Transition in Two-Dimensional, Incompressible Flow. In *Special Course on Stability and Transition of Laminar Flow*. Advisory Group for Aerospace Research & Development, 1984. AGARD Report 709.

[3] D. Arnal. Boundary Layer Transition: Prediction, Application to Drag Reduction. In *Special Course on Skin Friction Drag Reduction*. Advisory Group for Aerospace Research & Development, 1992. AGARD Report 786.

[4] C. Atkin. New Aerodynamic Approach to Suction System Design. In P. Thiede, editor, *Aerodynamic Drag Reduction Technologies: Proceedings of the CEAS/DragNet European Drag Reduction Conference*. Springer, 2000.

[5] J. A. Barros Filho, M. A. Navarro, F. A. P. Magalhaes, and A. A. Campagnole dos Santos. Pressure drop of flow through perforated plates. In *International Nuclear Atlantic Conference*, Santos, SP, Brazil, 2007.

[6] Boeing Commercial Airplane Group. High Reynolds Number Hybrid Laminar Flow Control (HLFC) Flight Experiment IV. Suction System Design and Manufacture. Technical report, National Aeronautics and Space Administration, 1999.

[7] Boeing Commercial Airplane Group. High Reynolds Number Hybrid Laminar Flow Control (HLFC) Flight Experiment III. Leading Edge Design, Fabrication, and Installation. Technical report, National Aeronautics and Space Administration, 1999.

[8] L. M. M. Boermans. Research on sailplane aerodynamics at Delft University of Technology. Recent and present developments. In *Presented to the Netherlands Association of Aeronautical Engineers (NVvL)*, 2006.

[9] J. Y. Boersma. Business Jet Design Using Laminar Flow. Master's thesis, Delft University of Technology, 2016.

[10] J. P. Boyd. *Chebyshev and Fourier Spectral Methods*. Dover, Mineola, NY, 2nd edition, 2000.

[11] A. L. Braslow. A History of Suction-Type Laminar-Flow Control with Emphasis on Flight Research. *Monographs in Aerospace History*, 13, 1999.

[12] A. L. Braslow, D. L. Burrows, N. Tetervin, and F. Visconti. Experimental and Theoretical Studies of Area Suction for the Control of the Laminar Boundary Layer of an NACA 64A010 Airfoil. Technical report, National Advisory Committee for Aeronautics, 1951.

[13] D. M. Bushnell. Aircraft drag reduction – a review. In *Proceedings of the Institution of Mechanical Engineers*, volume 217, 2003.

[14] D. M. Bushnell and M. H. Tuttle. *Survey and Bibliography on Attainment of Laminar Flow Control in Air Using Pressure Gradient and Suction*, volume 1. National Aeronautics and Space Administration, Hampton, VA, 1979.

[15] S. L. Chernyshev, A. Ph. Kiselev, and A. P. Kuryachii. Laminar flow control research at TsAGI: Past and present. *Progress in Aerospace Sciences*, 47:169–185, 2011.

[16] T. C. Corke and M. L. Post. Single dielectric barrier discharge plasma enhanced aerodynamics: physics, modeling and applications. *Experiments in Fluids*, 46:1–26, 2009.

[17] J. Cousteix. Basic Concepts on Boundary Layers. In *Special Course on Skin Friction Drag Reduction*. Advisory Group for Aerospace Research & Development, 1992. AGARD Report 786.

[18] Crane Co. Flow of Fluids through Valves, Fittings and Pipe. Technical report, 1982.

[19] R. E. Dannenberg, B. J. Gambucci, and J. A. Weiberg. Perforated Sheets as a Porous Material for Distributed Suction and Injection. Technical report, National Advisory Committee for Aeronautics, 1956.

[20] P. P. Doerffer and R. Bohning. Modelling of perforated plate aerodynamics performance. *Aerospace Science and Technology*, 4:525–534, 2000.

[21] J. E. Ellis, S. A. Walsh, and D. I. A. Poll. Assessment of the e^N Method as a Transition Prediction Tool for Zero Pressure Gradient Flows with and without Boundary Layer Suction. In P. Thiede, editor, *Aerodynamic Drag Reduction Technologies: Proceedings of the CEAS/DragNet European Drag Reduction Conference*. Springer, 2000.

[22] M. Gad-el-Hak. *Flow control: passive, active, and reactive flow management*. Cambridge University Press, 2000.

[23] G. Gan and S. B. Riffat. Pressure Loss Characteristics of Orifice and Perforated Plates. *Experimental Thermal and Fluid Science*, 14:160–165, 1997.

[24] D. E. Gault. An Experimental Investigation of Boundary-Layer Control for Drag Reduction of a Swept-Wing Section at Low Speed and High Reynolds Numbers. Technical report, National Aeronautics and Space Administration, 1960.

[25] M. Gerber. Device for Boundary Layer Suction and Composite Component therefor, 2014. US Patent US8800915 B2.

[26] N. Gregory. Research on Suction Surfaces for Laminar Flow. In G. V. Lachmann, editor, *Boundary Layer and Flow Control*, volume 2. Pergamon Press, 1961.

[27] B. Y. Guo, Q. F. Hou, A. B. Yu, L. F. Li, and J. Guo. Numerical modelling of the gas flow through perforated plates. *Chemical Engineering Research and Design*, 91:403–408, 2013.

[28] R. Henke. A320 HLF Fin Flight Tests Completed. *Air & Space Europe*, 1(2):76–79, 1999.

[29] E. L. Houghton, P. W. Carpenter, S. H. Collicott, and D. T. Valentine. *Aerodynamics for Engineering Students*. Elsevier, 6th edition, 2013.

[30] I. E. Idelchik. *Handbook of Hydraulic Resistance*. Israel Program for Scientific Translations, 1966.

[31] R. D. Joslin. Aircraft Laminar Flow Control. *Annual Review of Fluid Mechanics*, 30(1):1–29, 1998.

[32] U. Krause, P. Kreuzer, and H. Stuke. Air Outlet Design for a Passively Driven Hybrid Laminar Flow Control System. In *European Congress on Computational Methods in Applied Sciences and Engineering*, 2016.

[33] K. S. G. Krishnan, O. Bertram, and O. Seibel. Review of hybrid laminar flow control systems. *Progress in Aerospace Sciences*, 2017.

[34] S. G. Lekoudis. Stability of Boundary Layers over Permeable Surfaces. In *AIAA 16th Aerospace Sciences Meeting*, Huntsville, AL, 1978.

[35] L. M. Mack. Boundary-Layer Linear Stability Theory. In *Special Course on Stability and Transition of Laminar Flow*. Advisory Group for Aerospace Research & Development, 1984. AGARD Report 709.

[36] D. G. MacManus and J. A. Eaton. Measurement and Analysis of the Flowfields Induced by Suction Perforations. *AIAA Journal*, 36(9):1553–1561, 1998.

[37] D. G. MacManus and J. A. Eaton. Flow physics of discrete boundary layer suction measurements and predictions. *Journal of Fluid Mechanics*, 417:47–75, 2000.

[38] D. G. MacManus, J. A. Eaton, R. V. Barrett, J. Rickards, and C. Swales. Mapping the flow field induced by a HLFC perforation using a high resolution LDV. In *AIAA 34th Aerospace Sciences Meeting and Exhibit*, Reno, NV, 1996. American Institute of Aeronautics and Astronautics.

[39] S. Malavasi, G. Messa, U. Fratino, and A. Pagano. On the pressure losses through perforated plates. *Flow Measurement and Instrumentation*, 28:57–66, 2012.

[40] D. Maynes, G. J. Holt, and J. Blotter. Cavitation Inception and Head Loss Due to Liquid Flow Through Perforated Plates of Varying Thickness. *Journal of Fluids Engineering*, 135(3):1–11, 2013.

[41] J. Meister and J. Pfennig. Boundary Layer Suction Arrangement, 2007. US Patent US20070266707 A1.

[42] R. Michel. Boundary Layer Development and Transition. In *Boundary Layer Simulations and Control in Wind Tunnels*. Advisory Group for Aerospace Research & Development, 1988. AGARD Report 224.

[43] E. Obert. *Aerodynamic Design of Transport Aircraft*. IOS Press, 2009.

[44] N. Otsu. A Threshold Selection Method from Gray-Level Histograms. *IEEE Transactions on Systems, Man, and Cybernetics*, 9(1):62–66, 1979.

[45] W. Pfenninger. Laminar Flow Control, Laminarization. In *Special Course on Concepts for Drag Reduction*. Advisory Group for Aerospace Research & Development, 1977. AGARD Report 654.

[46] W. Pfenninger and J. W. Bacon. About the Development of Swept Laminar Suction Wings with Full Chord Laminar Flow. In G. V. Lachmann, editor, *Boundary Layer and Flow Control*, volume 2. Pergamon Press, 1961.

[47] W. Pfenninger and E. Groth. Low Drag Boundary Layer Suction Experiments in Flight on a Wing Glove of an F-94A Airplane with Suction through a Large Number of Fine Slots. In G. V. Lachmann, editor, *Boundary Layer and Flow Control*, volume 2. Pergamon Press, 1961.

[48] J. P. Robert. Drag Reduction: An Industrial Challenge. In *Special Course on Skin Friction Drag Reduction*. Advisory Group for Aerospace Research & Development, 1992. AGARD Report 786.

[49] W. S. Saric. Laminar-Turbulent Transition: Fundamentals. In *Special Course on Skin Friction Drag Reduction*. Advisory Group for Aerospace Research & Development, 1992. AGARD Report 786.

[50] H. Schlichting and K. Gersten. *Boundary-Layer Theory*. Springer-Verlag, 9th edition, 2017.

[51] V. Schmitt, J. P. Archambaud, K. H. Horstmann, and A. Quast. Hybrid Laminar Fin Investigations. In *Active Control Technology for Enhanced Performance Operational Capabilities of Military Aircraft, Land Vehicles and Sea Vehicles*, Braunschweig, 2000.

[52] G. Schrauf. Evaluation of the A320 hybrid laminar fin experiment. In *European Congress on Computational Methods in Applied Sciences and Engineering*, Barcelona, 2000.

[53] G. Schrauf. Status and Perspectives of Laminar Flow. *The Aeronautical Journal*, 109(1102):639–644, 2005.

[54] G. Schrauf. The Need of Large-Scale HLFC Testing in Europe. Technical report, Airbus Operations GmbH, Bremen, 2013.

[55] G. Schrauf. Hybrid Laminar Flow Control Test Cases for Transition and Drag Prediction. In *European Congress on Computational Methods in Applied Sciences and Engineering*, 2016.

[56] G. Schrauf and K. H. Horstmann. Linear Stability Theory Applied to Natural and Hybrid Laminar Flow Experiments. In P. Thiede, editor, *Aerodynamic Drag Reduction Technologies: Proceedings of the CEAS/DragNet European Drag Reduction Conference*. Springer, 2000.

[57] G. Schrauf and H. von Geyr. Simplified Hybrid Laminar Flow Control for Transport Aircraft. In *European Congress on Computational Methods in Applied Sciences and Engineering*, Vienna, Austria, 2012.

[58] A. Sciacchitano and B. Wieneke. PIV uncertainty propagation. *Measurement Science and Technology*, 27, 2016.

[59] A. Seitz and K. H. Horstmann. Design studies on NLF and HLFC applications at DLR. In *27th Congress of the International Council of the Aeronautical Sciences*, 2010.

[60] F. Shan, Z. Liu, W. Liu, and Y. Tsuji. Effects of the orifice to pipe diameter ratio on orifice flows. *Chemical Engineering Science*, 152:497–506, 2016.

[61] V. K. Singh and T. John Tharakan. Numerical simulations for multi-hole orifice flow meter. *Flow Measurement and Instrumentation*, 45:375–383, 2015.

[62] A. Smith and D. I. A. Poll. Instability and Transition of Flow at, and Near, an Attachment-Line – Including Control by Surface Suction. Technical report, National Aeronautics and Space Administration, 1998.

[63] A. M. O. Smith and N. Gamberoni. Transition, Pressure Gradient, and Stability Theory. Technical report, Douglas Aircraft Company, Inc., 1956. ES 26388.

[64] J. Sodja, M. J. Martinez, J. C. Simpson, and R. De Breuker. Experimental Evaluation of the Morphing Leading Edge Concept. In *23rd AIAA/AHS Adaptive Structures Conference*, Kissimmee, FL, 2015.

[65] P. R. Spalart and J. D. McLean. Drag reduction: enticing turbulence, and then an industry. *Philosophical Transactions of the Royal Society A*, 369:1556–1569, 2011.

[66] H. B. Squire. On the Stability for Three-Dimensional Disturbances of Viscous Fluid Flow between Parallel Walls. *Proceedings of the Royal Society of London. Series A, Containing Papers of a Mathematical and Physical Character*, 142(847):621–628, 1933.

[67] K. Steffens. Investigation on the pressure loss over the suction skin and the maximum suction threshold for use in Laminar Flow Control systems. Master's thesis, Delft University of Technology, 2005.

[68] W. Sui and D. Zhang. Four Methods for Roundness Evaluation. *Physics Procedia*, 24:2159–2164, 2012.

[69] E. Torenbeek. *Synthesis of Subsonic Airplane Design*. Springer-Science+Business Media, 1982.

[70] C. C. Tseng and C. J. Li. Numerical investigation of the inertial loss coefficient and the porous media model for the flow through the perforated sieve tray. *Chemical Engineering Research and Design*, 106: 126–140, 2016.

[71] J. Van Craenenbroeck. Boundary layer suction configurations with minimal pump requirements for multi-element airfoils. Master's thesis, Delft University of Technology, 2016.

[72] N. C. A. van den Berg. Studying the effect of boundary layer suction using design tools based on finite difference and integral methods. Master's thesis, Delft University of Technology, 2012.

[73] T. van der Hoeven. Slot Suction of the Turbulent Boundary Layer. Master's thesis, Delft University of Technology, 2013.

[74] J. L. van Ingen. A suggested semi-empirical method for the calculation of the boundary layer transition region. Technical report, Technische Hogeschool Delft, Vliegtuigbouwkunde, 1956. VTH-74.

[75] J. L. van Ingen. *Theoretical and Experimental Investigations of Incompressible Laminar Boundary Layers with and without Suction*. PhD thesis, Delft University of Technology, 1965.

[76] J. L. van Ingen. The e^N method for transition prediction. Historical review of work at TU Delft. In *38th Fluid Dynamics Conference and Exhibit*, 2008.

[77] L. J. Weber, M. P. Cherian, M. E. Allen, and M. Muste. Headloss Characteristics for Perforated Plates and Flat Bar Screens. Technical report, Iowa Institute of Hydraulic Engineering, Iowa City, IA, 2000.

[78] F. M. White. *Viscous Fluid Flow*. McGraw-Hill, 2nd edition, 1991.

[79] F. M. White. *Fluid Mechanics*. McGraw-Hill, New York, NY, 7th edition, 2011.

[80] T. Young, B. Mahony, B. Humphreys, E. Totland, A. McClafferty, and J. Corish. Durability of hybrid laminar flow control (HLFC) surfaces. *Aerospace Science and Technology*, 7:181–190, 2003.

A

Derivation of Boundary Layer Equations

Section 3.3.1 stated that the boundary layer equations for high-Reynolds number flow can be derived from the complete set of equations of motion by taking the limit for the Reynolds number tending to infinity. Thus, the equations of motion are first presented. The mass continuity equation is given by Eq. (A.1). The Navier-Stokes or momentum equations are given by Eq. (A.2).

$$\frac{D\rho}{Dt} + \rho \nabla \cdot \mathbf{u} = 0 \tag{A.1}$$

$$\rho \frac{D\mathbf{u}}{Dt} = \mathbf{f} - \nabla p + \nabla \cdot \boldsymbol{\tau} \tag{A.2}$$

Here, $\mathbf{u}$ is the velocity vector containing the Cartesian velocity components u, v, and w. Therefore, Eq. (A.2) comprises three equations, each describing the balance of momentum in a basic direction (x, y, or z). Furthermore, $\mathbf{f}$ contains the body forces, while $\boldsymbol{\tau}$ is the viscous stress tensor. Finally, $\frac{D}{Dt}$ is the convective derivative, which is given by Eq. (A.3).

$$\frac{D}{Dt} = \frac{\partial}{\partial t} + \mathbf{u} \cdot \nabla \tag{A.3}$$

A.1. Assumptions

Assuming an infinite swept wing introduces a simplification in the governing equations. The geometry of the wing is invariant in the spanwise direction. Therefore, any physical quantity is also invariant in the spanwise direction. In other words, following the reference frame from Fig. 3.2, all terms including $\frac{\partial}{\partial z}$ can be neglected.

Furthermore, it is assumed the flow is steady. This has as an effect that all terms including $\frac{\partial}{\partial t}$ can be neglected. Finally, body forces are not included in this analysis. Therefore, also the term containing the body forces, $\mathbf{f}$, can be neglected.

For the analysis of the boundary layer equations, a difference can be made between incompressible and compressible flow. Compressible flow is present in the typical transonic flight regime of a transport aircraft. Considering incompressible flow gives further simplifications over compressible flow.

A.2. Incompressible Boundary Layer Equations for Infinite Swept Wing

In incompressible flow, the density is constant. Thus, any variations of density can be excluded from the governing equations. The continuity equation (Eq. (A.1)) simplifies considerably, resulting in Eq. (A.4). The Navier-Stokes equations are also simplified because of this assumption, yielding Eq. (A.5). Furthermore, the assumptions of steady flow and zero body force have been applied.

$$\nabla \cdot \mathbf{u} = 0 \tag{A.4}$$

$$\rho \frac{D\mathbf{u}}{Dt} = -\nabla p + \mu \nabla^2 \mathbf{u} \tag{A.5}$$

The Cartesian equivalent of the continuity equation is given by Eq. (A.6). The Navier-Stokes equations split up into three momentum equations, in the x-, y-, and z-direction, respectively given by Eqs. (A.7a), (A.7b), and (A.7c). These equations have been divided by the density.

$$\frac{\partial u}{\partial x} + \frac{\partial v}{\partial y} + \frac{\partial w}{\partial z} = 0 \tag{A.6}$$

$$u\frac{\partial u}{\partial x} + v\frac{\partial u}{\partial y} + w\frac{\partial u}{\partial z} = -\frac{1}{\rho}\frac{\partial p}{\partial x} + \nu\left(\frac{\partial^2 u}{\partial x^2} + \frac{\partial^2 u}{\partial y^2} + \frac{\partial^2 u}{\partial z^2}\right) \tag{A.7a}$$

$$u\frac{\partial v}{\partial x} + v\frac{\partial v}{\partial y} + w\frac{\partial v}{\partial z} = -\frac{1}{\rho}\frac{\partial p}{\partial y} + \nu\left(\frac{\partial^2 v}{\partial x^2} + \frac{\partial^2 v}{\partial y^2} + \frac{\partial^2 v}{\partial z^2}\right) \tag{A.7b}$$

$$u\frac{\partial w}{\partial x} + v\frac{\partial w}{\partial y} + w\frac{\partial w}{\partial z} = -\frac{1}{\rho}\frac{\partial p}{\partial z} + \nu\left(\frac{\partial^2 w}{\partial x^2} + \frac{\partial^2 w}{\partial y^2} + \frac{\partial^2 w}{\partial z^2}\right) \tag{A.7c}$$

Now the effect of the assumption of an infinite swept wing can be illustrated. As mentioned in Sec. A.1, any variation in the z-direction is neglected. As a result, Eq. (A.6) simplifies to Eq. (A.8), and Eqs. (A.7) simplify to Eqs. (A.9).

$$\frac{\partial u}{\partial x} + \frac{\partial v}{\partial y} = 0 \tag{A.8}$$

$$u\frac{\partial u}{\partial x} + v\frac{\partial u}{\partial y} = -\frac{1}{\rho}\frac{\partial p}{\partial x} + \nu\left(\frac{\partial^2 u}{\partial x^2} + \frac{\partial^2 u}{\partial y^2}\right) \tag{A.9a}$$

$$u\frac{\partial v}{\partial x} + v\frac{\partial v}{\partial y} = -\frac{1}{\rho}\frac{\partial p}{\partial y} + \nu\left(\frac{\partial^2 v}{\partial x^2} + \frac{\partial^2 v}{\partial y^2}\right) \tag{A.9b}$$

$$u\frac{\partial w}{\partial x} + v\frac{\partial w}{\partial y} = \nu\left(\frac{\partial^2 w}{\partial x^2} + \frac{\partial^2 w}{\partial y^2}\right) \tag{A.9c}$$

These equations are in a dimensional form. In order to make a more direct application to any problem, the equations can be nondimensionalized. The approach to nondimensionalizing the governing equations and consequently deriving the boundary layer equations largely follows Schlichting and Gersten [50], but has been adapted to the present application (Sec. 3.3.1). For this, all Cartesian coordinates are divided by a characteristic length scale, L. The planar velocity components, u and v, are divided by the local edge velocity of the boundary layer, U_e. The cross flow velocity, w, is divided by the spanwise edge velocity of the boundary layer, W_e. Note that this is possible because Eq. (A.9c) is the only equation that depends on w, and is linear in u and v. The pressure is nondimensionalized by dividing it by ρU_e^2. The Reynolds number in this case is defined by Eq. (A.10).

$$Re = \frac{\rho U_e L}{\mu} = \frac{U_e L}{\nu} \tag{A.10}$$

The nondimensional parameters are indicated by the superscript *. The nondimensional spatial coordinates are given as in Eq. (A.11). The nondimensional velocity components are given by Eq. (A.12). The nondimensional pressure is given by Eq. (A.13).

$$x^* = \frac{x}{L}; \quad y^* = \frac{y}{L}; \quad z^* = \frac{z}{L} \tag{A.11}$$

$$u^* = \frac{u}{U_e}; \quad v^* = \frac{v}{U_e}; \quad w^* = \frac{w}{W_e} \tag{A.12}$$

$$p^* = \frac{p}{\rho U_e^2} \tag{A.13}$$

The nondimensional continuity equation is found by multiplying Eq. (A.8) by $\frac{L}{U_e}$, resulting in Eq. (A.14). The nondimensional x-momentum equation is found by multiplying Eq. (A.9a) by $\frac{L}{U_e^2}$, resulting in Eq. (A.15a). Note that the viscous term needs to be divided again by L to get nondimensional length scales. Furthermore, only one division by the velocity U_e was required for this term, leaving a remaining $\frac{1}{U_e L}$. Combining this with the viscosity ν yields the Reynolds number. Similarly, the nondimensional y-momentum equations is also found by multiplying Eq. (A.9b) by $\frac{L}{U_e^2}$, resulting in Eq. (A.15b). The nondimensional z-momentum equation is found through similar reasoning, but instead multiplying Eq. (A.9c) by $\frac{L}{U_e W_e}$, resulting in Eq. (A.15c).

$$\underbrace{\frac{\partial u^*}{\partial x^*}}_{O(1)} + \underbrace{\frac{\partial v^*}{\partial y^*}}_{O(1)} = 0 \tag{A.14}$$

$$\underbrace{u^* \frac{\partial u^*}{\partial x^*}}_{O(1)} + \underbrace{v^* \frac{\partial u^*}{\partial y^*}}_{O(1)} = -\frac{\partial p^*}{\partial x^*} + \underbrace{\frac{1}{Re}}_{O(\delta^{*2})} \left(\underbrace{\frac{\partial^2 u^*}{\partial x^{*2}}}_{O(1)} + \underbrace{\frac{\partial^2 u^*}{\partial y^{*2}}}_{O(1/\delta^{*2})} \right) \tag{A.15a}$$

$$\underbrace{u^* \frac{\partial v^*}{\partial x^*}}_{O(\delta^*)} + \underbrace{v^* \frac{\partial v^*}{\partial y^*}}_{O(\delta^*)} = -\frac{\partial p^*}{\partial y^*} + \underbrace{\frac{1}{Re}}_{O(\delta^{*2})} \left(\underbrace{\frac{\partial^2 v^*}{\partial x^{*2}}}_{O(\delta^*)} + \underbrace{\frac{\partial^2 v^*}{\partial y^{*2}}}_{O(1/\delta^*)} \right) \tag{A.15b}$$

$$\underbrace{u^* \frac{\partial w^*}{\partial x^*}}_{O(1)} + \underbrace{v^* \frac{\partial w^*}{\partial y^*}}_{O(1)} = \underbrace{\frac{1}{Re}}_{O(\delta^{*2})} \left(\underbrace{\frac{\partial^2 w^*}{\partial x^{*2}}}_{O(1)} + \underbrace{\frac{\partial^2 w^*}{\partial y^{*2}}}_{O(1/\delta^{*2})} \right) \tag{A.15c}$$

If now the limit for $Re \to \infty$ is taken for Eqs. (A.15), as was indicated in Sec. 3.3.1, all viscous components would drop out, and the inviscid solution would be obtained. However, the inviscid solution generally does not satisfy the no-slip condition at the wall. Thus, it becomes clear that not all viscous terms can be neglected to study the boundary layer flow.

In order to determine which terms are important for the boundary layer flow, a study of the order of magnitude of all terms is performed. The nondimensional streamwise and spanwise lengths and velocity components (x^*, z^*, u^*, and w^*) can be said to be of order of magnitude $O(1)$. However, the boundary layer is very thin, so the wall-normal length scale in the boundary layer will not be $O(1)$. In fact, this length is of the order of the boundary layer thickness, $y = O(\delta)$. The nondimensional wall-normal coordinate will thus be of the order of magnitude of the nondimensional boundary layer thickness, δ^*, implying $y^* = O(\delta^*)$. For a laminar boundary layer, the relative boundary layer thickness is inversely proportional to the square root of the Reynolds number, indicated in Eq. (A.16) [50].

$$\delta^* = \frac{\delta}{L} \sim \frac{1}{\sqrt{Re}} \tag{A.16}$$

From this relation, it can be determined that the term $1/Re$ will have order of magnitude $O(\delta^{*2})$. The order of magnitude of the pressure gradient can vary. The relative importance of the pressure gradient will become clear after the analysis of the other terms. The order of magnitude of the relevant terms in Eqs. (A.14) and (A.15) is indicated underneath each equation.

So far, all terms have been assigned an order of magnitude, except for the normal velocity, v^*. Its order of magnitude follows from the continuity equation (Eq. (A.14)). The length scale y^* is of order $O(\delta^*)$ which will tend to zero as $Re \to \infty$. Thus, in order to avoid that $\frac{\partial v^*}{\partial y^*}$ become degenerate, the normal velocity must be of the same order as the length scale: $v^* = O(\delta^*)$.

Since the length scale and velocity component normal to the wall are very small, $O(\delta^*)$, they are not suitable to study the boundary layer. It is desired to have wall-normal variables that describe the boundary layer on an $O(1)$ scale. To do this, the boundary layer transformation is introduced, which yields the new definitions of the wall-normal variables given by Eq. (A.17) [50].

$$\bar{y} = y^* \sqrt{Re} = O(1); \quad \bar{v} = v^* \sqrt{Re} = O(1) \tag{A.17}$$

Substituting the boundary layer variables into Eqs. (A.14) and (A.15) gives the transformed equations, Eqs. (A.18) and (A.19). Note that terms involving wall-normal variables are now of order $O(1)$.

$$\underbrace{\frac{\partial u^*}{\partial x^*}}_{O(1)} + \underbrace{\frac{\partial \bar{v}}{\partial \bar{y}}}_{O(1)} = 0 \tag{A.18}$$

$$\underbrace{u^* \frac{\partial u^*}{\partial x^*}}_{O(1)} + \underbrace{\bar{v} \frac{\partial u^*}{\partial \bar{y}}}_{O(1)} = -\frac{\partial p^*}{\partial x^*} + \underbrace{\frac{1}{Re}}_{O(\delta^{*2})} \underbrace{\frac{\partial^2 u^*}{\partial x^{*2}}}_{O(1)} + \underbrace{\frac{\partial^2 u^*}{\partial \bar{y}^2}}_{O(1)} \tag{A.19a}$$

$$\underbrace{\frac{1}{Re}}_{O(\delta^{*2})} \underbrace{u^* \frac{\partial \bar{v}}{\partial x^*}}_{O(1)} + \underbrace{\frac{1}{Re}}_{O(\delta^{*2})} \underbrace{\bar{v} \frac{\partial \bar{v}}{\partial \bar{y}}}_{O(1)} = -\frac{\partial p^*}{\partial \bar{y}} + \underbrace{\frac{1}{Re^2}}_{O(\delta^{*4})} \underbrace{\frac{\partial^2 \bar{v}}{\partial x^{*2}}}_{O(1)} + \underbrace{\frac{1}{Re}}_{O(\delta^{*2})} \underbrace{\frac{\partial^2 \bar{v}}{\partial \bar{y}^2}}_{O(1)} \tag{A.19b}$$

$$\underbrace{u^* \frac{\partial w^*}{\partial x^*}}_{O(1)} + \underbrace{\bar{v} \frac{\partial w^*}{\partial \bar{y}}}_{O(1)} = \underbrace{\frac{1}{Re}}_{O(\delta^{*2})} \underbrace{\frac{\partial^2 w^*}{\partial x^{*2}}}_{O(1)} + \underbrace{\frac{\partial^2 w^*}{\partial \bar{y}^2}}_{O(1)} \tag{A.19c}$$

Now the boundary layer simplification for large Reynolds numbers can be found. As mentioned in the beginning of Sec. 3.3.1, the limit for $Re \to \infty$ is taken, leading to Eqs. (A.20) and (A.21).

$$\frac{\partial u^*}{\partial x^*} + \frac{\partial \bar{v}}{\partial \bar{y}} = 0 \tag{A.20}$$

$$u^* \frac{\partial u^*}{\partial x^*} + \bar{v} \frac{\partial u^*}{\partial \bar{y}} = -\frac{\partial p^*}{\partial x^*} + \frac{\partial^2 u^*}{\partial \bar{y}^2} \tag{A.21a}$$

$$-\frac{\partial p^*}{\partial \bar{y}} = 0 \tag{A.21b}$$

$$u^* \frac{\partial w^*}{\partial x^*} + \bar{v} \frac{\partial w^*}{\partial \bar{y}} = \frac{\partial^2 w^*}{\partial \bar{y}^2} \tag{A.21c}$$

The important result of the boundary layer approximation is that the pressure normal to the wall does not vary inside the boundary layer. Thus, the pressure inside the boundary layer is determined by the pressure outside the boundary layer. Consequently, the outer pressure distribution may be obtained separately and imposed onto the boundary layer as a boundary condition.

Furthermore, the pressure gradient in the streamwise direction may be eliminated. The boundary layer changes smoothly into the outer flow (Sec. 2.2), which means that the velocity gradients in the y-direction are zero at the boundary layer edge. By using this information in Eq. (A.21a), the pressure gradient at the boundary layer edge is given by Eq. (A.22). Because the pressure does not vary in the y-direction, this streamwise pressure gradient applies everywhere in the boundary layer thickness.

$$\frac{\partial p^*}{\partial x^*} = -U_e^* \frac{dU_e^*}{dx^*} \tag{A.22}$$

Thus, for an incompressible, steady flow over an infinite swept wing, the boundary layer equations are given by Eqs. (A.23) and (A.24). The corresponding boundary conditions are given in (A.25). Note that the streamwise and spanwise velocity components must be zero at the wall, due to the no-slip condition. Furthermore, they have to be equal to the outer velocity components at the edge of the boundary layer. A no-penetration condition on the wall-normal velocity would make $\bar{v}$ zero at the wall. Allowing for transpiration, however, $\bar{v}$ can be any function of x^*. Note that it is important that $\bar{v}$ remain $O(1)$, which is to say that v should remain small ($O(\delta)$), because this condition was used in the derivation of the boundary layer equations.

$$\frac{\partial u^*}{\partial x^*} + \frac{\partial \bar{v}}{\partial \bar{y}} = 0 \tag{A.23}$$

$$u^* \frac{\partial u^*}{\partial x^*} + \bar{v} \frac{\partial u^*}{\partial \bar{y}} = U_e^* \frac{dU_e^*}{dx^*} + \frac{\partial^2 u^*}{\partial \bar{y}^2} \tag{A.24a}$$

$$u^* \frac{\partial w^*}{\partial x^*} + \bar{v} \frac{\partial w^*}{\partial \bar{y}} = \frac{\partial^2 w^*}{\partial \bar{y}^2} \tag{A.24b}$$

$$\begin{array}{rlll} \bar{y} = 0: & u^* = 0; & \bar{v} = f(x^*); & w^* = 0 \\ \bar{y} \to \infty: & u^* = 1; & & w^* = 1 \end{array} \tag{A.25}$$

B

Orr-Sommerfeld Equation

The Orr-Sommerfeld equation, as a basis of linear stability theory, is based on the assumption that the base boundary layer flow is incompressible, has no curvature, and is parallel [17, 49]. A parallel flow has the property that it is independent of the streamwise and spanwise directions and that the normal velocity is zero [49]. That is to say, $u = u(y)$, $w = w(y)$, and $v = 0$. This seems like a strong simplification, but, as Saric notes, non-parallel effects are not the most important to capture the necessary physics for the stability of the flow [49]. This parallel flow may be interpreted as a simplified boundary layer. For a general boundary layer, u and w are much larger than v. Even with suction, the normal velocity was still assumed to be small (Sec. A.2). Thus, since $u,\ w \gg v$, it is reasonable to let $v = 0$. Furthermore, velocity changes in a boundary layer happen much more quickly in the wall-normal direction than the tangential direction. Therefore, it can also be imagined that $\frac{\partial \mathbf{u}}{\partial y} \gg \frac{\partial \mathbf{u}}{\partial x}, \frac{\partial \mathbf{u}}{\partial z}$, which in the simplest form implies that u and w are only functions of y.

Adding disturbances waves to the simplified flow, as shown in Eq. (B.1), is the starting point of the Orr-Sommerfeld equation. The base flow is steady and is indicated with an overbar. The unsteady fluctuations are indicated with a prime, and are waves with a frequency ω that propagate in the direction of the wave number vector (k), which has a streamwise component (α) and a spanwise component (β) [35]. In addition, the notation of App. A is followed, where symbols with a superscript * are nondimensional quantities.

$$u = \bar{u} + u'; \quad v = v'; \quad w = \bar{w} + w'; \quad p = \bar{p} + p' \tag{B.1}$$

With respect to scaling, all velocity components are scaled with either U_∞ [49] or U_e [35]. Lengths are scaled with the boundary layer reference length: the Blasius length scale (l), given by Eq. (B.2). Here, the reference velocity U may again be chosen to be U_∞ or U_e. The pressure is scaled with ρU^2, again evaluated in the freestream or at the boundary layer edge. Time is scaled with l/U and frequency with the inverse.

$$l = \sqrt{\frac{\nu x}{U}} = \frac{x}{\sqrt{Re_x}} \tag{B.2}$$

The next step is to specify that the perturbed quantities of Eq. (B.1) still satisfy the continuity and Navier-Stokes equations (Eqs. (A.1) and (A.2)). After substitution, nondimensionalizing, subtracting the mean flow, and neglecting the terms which include products of disturbance quantities (for example, $u' \frac{\partial u'}{\partial x} \ll u'$), a system of equations results that is linear in the disturbance quantities [35].

The linear disturbance equations contain mean flow coefficients that only depend on y because of the parallel-flow assumption. This implies the solutions are separable and a possible solution is Eq. (B.3) [35, 49]. The terms $\hat{u}^*$, $\hat{v}^*$, $\hat{w}^*$, and $\hat{p}^*$ describe the shape and amplitude of the modes in the boundary layer, while the exponential term describes that the disturbances are traveling waves in the xz-plane.

$$\begin{bmatrix} u'^* \\ v'^* \\ w'^* \\ p'^* \end{bmatrix} = \begin{bmatrix} \hat{u}^*\left(y^*\right) \\ \hat{v}^*\left(y^*\right) \\ \hat{w}^*\left(y^*\right) \\ \hat{p}^*\left(y^*\right) \end{bmatrix} e^{i(\alpha^* x^* + \beta^* z^* - \omega^* t^*)} \tag{B.3}$$

The solutions from Eq. (B.3) are only valid for a parallel boundary layer. However, the mean flow quantities and boundary layer thickness vary with chordwise position in a real boundary layer. This means the problem changes with every step. If the boundary layer growth is sufficiently small, in practice in can be assumed that the flow is locally parallel. This is the quasi-parallel theory [35]. By doing this, the solutions from Eq. (B.3) can be maintained, but they must be slightly adapted, as shown in Eq. (B.4) [49].

$$\begin{bmatrix} u'^* \\ v'^* \\ w'^* \\ p'^* \end{bmatrix} = \begin{bmatrix} \hat{u}^*\left(y^*\right) \\ \hat{v}^*\left(y^*\right) \\ \hat{w}^*\left(y^*\right) \\ \hat{p}^*\left(y^*\right) \end{bmatrix} e^{i\Theta} \tag{B.4}$$

In Eq. (B.4), the phase function Θ has the properties that $\frac{\partial\Theta}{\partial x^*} = \alpha^*$, $\frac{\partial\Theta}{\partial z^*} = \beta^*$, and $\frac{\partial\Theta}{\partial t^*} = -\omega^*$. This is an additional simplification over linearization. Non-parallel effects are ignored with this simplification. As mentioned in the beginning of this section, these do not have a great effect on the stability results.

When the solutions of Eq. (B.3) or (B.4) are substituted into the linearized disturbance equations, a system of four equations results. These equations may be combined to form a single, fourth order equation for $\hat{v}^*$, given in Eq. (B.5) [35, 49]. Here ϕ is used to indicate $\hat{v}^*$.

$$\begin{aligned} &\frac{d^4\phi}{dy^{*4}} - 2\left(\alpha^{*2}+\beta^{*2}\right)\frac{d^2\phi}{dy^{*2}} + \left(\alpha^{*2}+\beta^{*2}\right)^2\phi = \\ &\qquad iRe_l\left(\left(\alpha^*\bar{u}^* + \beta^*\bar{w}^* - \omega^*\right)\left(\frac{d^2}{dy^{*2}} - \left(\alpha^{*2}+\beta^{*2}\right)\right) - \left(\alpha^*\frac{d^2\bar{u}^*}{dy^{*2}} + \beta^*\frac{d^2\bar{w}^*}{dy^{*2}}\right)\right)\phi \end{aligned} \tag{B.5}$$

For a two-dimensional boundary layer, $\bar{w} = \beta = 0$, and Eq. (B.5) simplifies to Eq. (B.6). This is the Orr-Sommerfeld equation. The three-dimensional version of the Orr-Sommerfeld equation, Eq. (B.5), should be used for three-dimensional boundary layers.

$$\frac{d^4\phi}{dy^{*4}} - 2\alpha^{*2}\frac{d^2\phi}{dy^{*2}} + \alpha^{*4}\phi = iRe_l\left(\left(\alpha^*\bar{u}^* - \omega^*\right)\left(\frac{d^2}{dy^{*2}} - \alpha^{*2}\right) - \alpha^*\frac{d^2\bar{u}^*}{dy^{*2}}\right)\phi \tag{B.6}$$

For the boundary conditions, the no-slip condition at the wall implies that the disturbances in the tangential velocities, u' and w', must be zero there. The no-penetration condition implies that v' cannot vary at the wall. Without any variation in velocity, the pressure also does not fluctuate. Therefore, $\hat{u} = \hat{v} = \hat{w} = \hat{p} = 0$ for $y = 0$. The effect of boundary layer transpiration will be addressed later. Far away from the wall, the disturbances should go to zero, implying $\hat{u} = \hat{v} = \hat{w} = \hat{p} = 0$ as $y \to \infty$.

Equation (B.5) is a fourth order equation for $\hat{v}^*$, or ϕ, so four boundary conditions on ϕ are needed. So far, two boundary conditions have been specified, namely that $\phi = 0$ for $y = 0$ and $y \to \infty$. The other two boundary conditions follow from the continuity equation. The continuity equation for the disturbances says that the divergence of the disturbance velocity components is zero. Since u' and w' are zero at the boundaries of the domain, they are also invariant in the x- and z-directions, respectively. Therefore, the continuity equation implies that the variation of v' in the y-direction is also zero. So, the two additional boundary conditions on ϕ are that $\frac{d\phi}{dy^*} = 0$ for $y^* = 0$ and $y^* \to \infty$.

C

Uncertainty Propagation

All uncertainties of the measured variables, namely the hole diameter, open area ratio, mass flow rate, pressure drop, and flow temperature, were propagated into the uncertainty of the results presented in Chap. 7. The propagation of uncertainty was assessed by means of Eq. (C.1), which states that the standard deviation of variable y is related through partial derivatives to the standard deviation of each variable x_j with $j = 1, 2, \ldots, n$, on which y is dependent [58].

$$\sigma_y^2 = \sum_{j=1}^{n} \left(\frac{\partial y(x_1, x_2, \ldots, x_n)}{\partial x_j} \right)^2 \sigma_{x_j}^2 \tag{C.1}$$

The origins of the uncertainties in the measured variables were discussed in Sec. 7.8, except for the uncertainty in the open area ratio, since it is not measured directly. Instead, it is based on the hole diameter, which is measured directly. So, the uncertainty on β was derived from Eq. (C.1), by assuming that Eq. (6.2) holds, which is true for the titanium articles and approximately true for the acrylic articles, because β_{acrylic} was determined slightly differently. Thus, σ_β was found as in Eq. (C.2).

$$\sigma_\beta = 2N \frac{d}{D^2} \sigma_d \tag{C.2}$$

The experimental results in Chap. 7 were presented in terms of $C_{\Delta p}$ and $Re_d \cdot \frac{d}{t}$. In order to evaluate the uncertainty of these variables using Eq. (C.1), the variables need to be expressed as a function of the measured quantities. Following the procedure from Sec. 7.1, this yields Eq. (C.3) for the pressure drop coefficient, and Eq. (C.4) for $Re_d \cdot \frac{d}{t}$.

$$C_{\Delta p} = \frac{\pi^2}{8} D^4 \Delta p \frac{p_{\text{atmosphere}} + \Delta p}{RT} \frac{\beta^2}{\dot{m}^2} \tag{C.3}$$

$$Re_d \cdot \frac{d}{t} = \frac{\dot{m} d^2}{\mu \beta t \frac{\pi}{4} D^2} \tag{C.4}$$

Subsequently, the partial derivatives can be evaluated, from which the uncertainty follows. The results were presented in Fig. 7.11.